Università degli Studi di Padova
Dipartimento di Fisica ed Astronomia "G. Galilei"

Tesi di Laurea in Fisica

Integrated Opto-Microfluidic Lab-on-a-Chip in Lithium Niobate for Sensing Applications

Laureando:

Carlo Montevecchi

Relatore:
Prof.ssa Cinzia Sada

Anno Accademico 2015/2016

Abstract

In recent years a renewed interest in microfluidics by the scientific community has lead to an increasing amount of reaserches in this field, thanks to the possibility of manipulating and analysing fluids on the microscale, a feature with wide applications in physics and chemistry but also in the fields of biology, medicine and enviromental sciences.

The combination of microfluidics and integrated fast analysis tools allows for the realizaion of miniaturized and portable Lab-On-a-Chip (LOC) devices able to perform analyses typically restricted to traditional laboratory facilities, requiring very small amounts of reagents and analytes with much faster reaction times.

Nevertheless, sensing in LOCs is usually not integrated in the device itself, so that there is still a need for external optical stages added to the microfluidic chip, nullifying the efforts spent to decrease the size of LOCs and their related advantages. Integration of these optical stages inside a microfluidic LOC is one of the biggest challenges researchers are facing in the realization of completely stand-alone LOCs.

In this work the first opto-microfluidic Lab-On-a-Chip for both the generation and detection of droplets, entirely integrated in lithium niobate, is presented. The device is composed of a microfluidic stage consisting in a passive droplet generator, where water in oil droplets are produced by the cross-flow of the two immiscible phases, and an optical stage consisting in two optical waveguides coupled with a microfluidic channel in which the produced droplets flow.

We report the realization of single mode channel waveguides at a wavelenth of 632.8nm in lithium niobate and their characterization by Rutherford Backscattering Spectrometry (RBS), Secondary Ion Mass Spectrometry (SIMS) and Near Field (NF) measurements.

The applicability of lithium niobate in the field of microfluidics is investigated, showing the micromachining process used to obtain microfluidic channels in this material and studying its wettability properties. A functionalization procedure is defined to improve its hydrophobicity allowing for the production of water droplets in oil. Different sealing techniques are also tested for the realization of microfluidic chips in lithium niobate.

These studies allow for the realization of a microfluidic chip in lithium niobate with a cross-junction droplet generator, which is characterized in a T-junction configuration to asses its performances in comparison to similar devices.

Finally the coupling of the optical waveguides to the microfluidic stage is achieved, and two possible applications for our opto-microfluidic prototype are discussed. The first one

is the use of the optical stage as a droplet counter, able to detect the time of passage of the droplets in front of the waveguides. The second one consists in the sensing of the refractive index of couples of droplets produced in a cross junction used in an alternating droplet configuration. The couples of droplets contain a saline solution and pure water respectively, and the sensor works by collecting and comparing the trasmitted signal from the solution and from the reference water. the transmitted intensity from the waveguide is shown to be sensitive to the refractive index of the solution with a sensitivity of $\Delta n = 2 \cdot 10^{-3}$ in the range $n = [1.339, 1.377]$.

This is the first example of a Lab-On-a-Chip for real time droplet counting and refractive index sensing, completely integrated in lithium niobate.

Estratto

Negli ultimi anni un nuovo interesse per la microfluidica si è diffuso nella comunità scientifica, con un numero sempre crescente di ricerche in materia, grazie alla possibilità di manipolare e analizzare fluidi all microscala, una caratteristica che permette un largo numero di applicazioni in fisica e chimica, ma anche nel campo della biologia, della medicina e delle scienze ambientali.

La combinazione della microfluidica e di strumenti di analisi integrati ad alta velocità permette la realizzazione dei cosiddetti Lab-On-a-Chip (LOC), ovvero laboratori su chip, capaci di eseguire analisi tipicamente possibili solo all'interno di laboratori tradizionali, utilizzando minime quantità di reagenti e analiti e con alte velocità di reazione.

Tuttavia, la parte sensoristica nei LOC spesso non è integrata nel chip stesso, richiedendo comunque la presenza di apparati ottici esterni al chip microfluidico, di fatto azzerando l'impegno nel ridurre le dimensioni degli LOC eliminando la loro portabilità. L'integrazione di questi apparati ottici all'interno dei chip microfluidici è una delle più grandi sfide affrontate dai ricercatori per la creazione di un LOC completamente autonomo.

In questo lavoro viene presentato il primo Lab-On-a-Chip opto-microfluidico in niobato di litio, dotato sia di un generatore che di un sensore di gocce. Lo strumento è composto da due stadi: uno stadio microfluidico in cui un generatore passivo produce gocce di acqua in olio grazie al flusso incrociato delle due fasi immiscibili; e uno stadio ottico che consiste in due guide d'onda ottiche accoppiate a un canale microfluidico in cui scorrono le gocce.

Riportiamo la realizzazione di guide ottiche a canale a una lunghezza d'onda di 632.8nm in niobato di litio e la loro caratterizzazione tramite le tecniche di Rutherford Back Scattering (RBS), Secondary Ion Mass Spectrometry (SIMS) e misure in campo vicino (Near Field, NF).

Si è investigata la possibilità di utilizzare il niobato di litio nel campo della microfluidica, mostrando che è possibile ottenere canali microfluidici grazie a un processo di microlavorazione per mezzo di una sega da taglio, e facendo uno studio sulla sua bagnabilità. Si è definito un processo di funzionalizzazione per migliorare l'idrofobicità del niobato di litio per poter produrre gocce di acqua in olio. Sono stati studiati diversi tipi di chiusura per la realizzazione di un chip microfluidico.

Con questi studi è stato possibile realizzare un chip microfluidico in niobato di litio con un generatore di gocce con giunzione a croce, il quale è stato caratterizzato in una configurazione con giunzione a T per verificarne le prestazioni, confrontandole con quelle

di strumenti simili.

Per concludere si è riusciti ad accoppiare le guide d'onda ottiche allo stadio microfluidico, e si sono testate due applicazioni per prototipo di chip opto-microfluidico. La prima è l'uso dello stadio ottico come contagocce, con la capacità di rilevare il tempo di passaggio delle gocce di fronte alle guide d'onda. La seconda applicazione è consistita nel rilevare l'indice di rifrazione di coppie di gocce prodotte nella giunzione a croce in una configurazione a gocce alternate. Le coppie di gocce contengono rispettivamente una soluzione salina e acqua pura, e il sensore rileva e confronta il segnale trasmesso dalla soluzione con il segnale ottenuto dall'acqua pura di riferimento. L'intensità trasmessa dalle guide d'onda è risultata sensibile all'indice di rifrazione della soluzione con una sensibilità $\Delta n = 2 \cdot 10^{-3}$ in un intervallo $n = [1.339, 1.377]$.

Questo è il primo esempio di Lab-On-a-Chip completamente integrato in niobato di litio per il conteggio di gocce in tempo reale a per la rilevazione dell'indice di rifrazione.

Contents

Introduction

Microfluidic technology holds great promise as ti can perform typical laboratory applications using a fraction of the volume of reagents in significantly less time. For these reasons, applications for microfluidics have clearly advanced from their root in micro-analytical chemistry. Unlike continuous flow systems, droplet-based systems focus on creating descrete volumes with the use of immiscible phases. Thanks to its scalability and parallel processing, droplet microfluidics has been used in a wide range of applications including the synthesis of biomolecules, drug delivery, diagnostic testing and biosensing. In addition droplet-based devices can easily increase in complexity without an increase in overall size, as opposed to flow based system that scale almost linearly with complexity, and they also offer great versatility connected to the creation and manipulation of descrete droplets inside microdevices. Different methods have been devised able to produce highly monodisperse droplets in the nanometer to micrometer range, at rates of up to twenty thousand per second. Due to high surface to area ratios at the microscale, heat and mass transfer times and diffusion distances are shorter, facilitating faster reaction times, aided also by convective motions inside the droplets which also help maintain uniformity. unlike continuous-flow microfluidics, droplet-based microfluidics allows also for independent control of each droplet, thus generating micro-reactor that can be individually transported, mixed and analysed, allowing for parallel processing and for large sets of data to be acquired in a short time.

There are three main droplet generation techniques: co-flowing systems, T-junction and flow-focusing devices. In all cases the dispersed phase is injected in the device where it comes in contact with the carrier phase, which is independently driven. This results in an instability in the flow that leads to the formation of droplets. A number of material have been exploted for the creation of microfluidic circuits, including polymers and glass. Further stages such as those required for fluid pumping and sorting and for the optical analysis are realized by using external equipments or different materials, lithium niobate being one of these. In particular, chemical and physical sensors perfectly integrated with the microfluidic circuit is still under debate, although optical methods are the most used. One of the min reasons for the lack of integration is the fact that the most commonly used materials, like PDMS and glass, complicate the full integration of the fluidic and optical functionalities in the same substrate. In this scenario, the integration of a large number of different stages on a single substrate chip is a key point for promoting new insights in

many applications where portability and speed of analysis are needed, as well as allowing the investigation of new phenomena.

This work of thesis is part of the reaserch conducted by the $LiNbO_3$ group of the Department of Physics of Padova, aiming to realize a miniaturized portable device able to perform chemical, biological, enviromental or medical analysis, all in a single multipurpose platform.

To reach such an ambitious goal, a series of miniaturized stages developed in the fields of optics and microfluidics have to be integrated inside a single chip of a few square centimeters and must be coupled with each other for the manipulation and analysis of fluid volumes of the order of the nanoliter. Miniaturization and integration in these so called Lab-On-a-Chip (LOCs) devices present different advantages:

- **portability**: a fully integrated LOC offers the possibility of performing on-field measurements without the need of lab facilities;
- **affordability**: an LOC would have a production and operating cost several times lower than a standard laboratory facility, with the prospect of mass production and a very low reagent consumption, since a very small amount is sufficient for its operations;
- **throughput**: due to the high degree of control in the manipulation of small amounts of fluid, fast multiplexed simultaneous analyses can be performed easily.

Sensing inside LOCs is usually performed by macro-optical stages externally added to a microfluidic chip. The integration of a microfluidic and an optical stage represents a serious challenge and is currently the focus of a series of reaserches involved in LOCs development. Often extended systems such as microscopes and fast cameras have been used to detect droplets inside microfluidic channels. Recently, methods to embed optical fibres in the same polymeric matrix employed to to realize the microfluidic stage have been proposed, representing the first examples of opto-microfluidic integration [1, 2]. However, while polymeric materials allow for the realization of inexpensive and easy to produce devices, they suffer from degradation and poor stiffness, as well as not being suitable for certain biological or chemical applications due to possible interactions between the cells or reagents and the channel walls. In addition, optical fibers, while easy to integrate, pose some limitations when trying to integrate other types of optical stages on the same device. A different approach was the employment of optical waveguides coupled to microfluidic channels both fabricated by femtosecond laser irradiation on fused silica. However, no attempt to use this system both to inject the laser beam as well as collecting the optical signal have been reported [3, 4, 5], meaning only partial integration of the optical stage has been achieved.

Lithium niobate is a material with exceptional optical properties which have been largely exploited in the photonics and integrated optics industry, and could therefore be a good candidate for the realization of an integrated opto-fluidic device. As a matter of

fact lithium niobate can host high quality optical waveguides and complex devices such as multiplexers, switches and optical modulators which are commercially available, as well as Bragg gratings and Mach-Zehnder interferometers can be realized on a single lithium niobate crystal. In addition, lithium niobate has been effectively used for the manipulation of nano-droplets, exploiting surface acoustic waves (SAW) thanks to its piezoelectricity[6, 7], and very recently it has also been employed to trap particles dispersed in oil, exploiting its photovoltaic properties [8, 9, 10, 11]

Our group was the first to realize microfluidic channels in lithium niobate [12] with very good results, with the next step being the integration of an optical stage on such a device.

In this thesis the first Lab-on-a-Chip prototype for both generation and detection of droplets, completely integrated in lithium niobate is presented, along with an application for a droplet based refractive index sensor.

The idea is to couple two optical waveguides perpendicularly to a microfluidic channel in order to perform an optical analysis of the droplets flowing inside the channel. The elements of the prototype are:

- a droplet generator characterized by a cross-junction between two perpendicular microfluidic channels inside which water droplets in oil are produced passively thanks to the geometry of the junction and the interaction between the two fluids;
- two aligned waveguides crossing the microfluidic channel at a right angle; the first one is coupled with a laser and is used to illuminate the droplets flowing inside the channel, the second one at the other side of the channel collects the transmitted intensity.

The performances of this system to count and trigger water droplets, as well as a measure of their refractive index will be treated in this work.

The thesis will be organized as follows:

Chapter 1 will present lithium niobate, covering its compositional, piezoelectric, pyroelectric and optical properties. Special attention will be dedicated to those properties which could be exploited for opto-fluidics applications.

Chapter 2 will briefly discuss the theory of guided light, followed by a brief section on the state of the art of optical waveguides in lithium niobate. The realization of single mode titanium in-diffused waveguides at 632.8nm will then be discussed as well as their characterization by means of Rutherford Backscattering Spectroscopy (RBS), Secondary Ion Mass Spectroscopy (SIMS) and Near Field (NS) measurements, together with the discussion of the results from a FEM based simulation.

Chapter 3 will be dedicated to droplets microfluidic theory and droplet generation, as well as prsenting the techniques emplyed for the production, sealing and functionalization of our microfluidic device.

Chapter 4 will deal with the microfluidic characterization of the realized droplet generator, comparing the results with the theoretical models proposed in literature.

Chapter 6 will deal with the coupling of the waveguides to the microfluidic channels and the employment of the opto-fluidic prototype as a droplet counter and as a refractive index sensor.

Chapter 1

Lithium Niobate

1.1 Compositional and Crystallographic Properties

Lithium niobate is a synthetic man-made material which cannot be found in nature. It was described for the first time by Zachariasen in 1928 and first discovered to be ferroelectric in 1949. In the sixties lithium niobate was widely investigated by Nassau and Abrahams at Bell Laboratories who published a series of papers about the structures and properties of the material. It is one of the four compounds of the pseudo-binary system Li_2O-Nb_2O_5, besides $Li_2Nb_28O_71$, Li_3NbO_4 and lithium triniobate $LiNb_3O_8$. The crystal is usually grown by Czochralski technique in its *congruent* composition which is characterized by a lithium deficiency (48.45% of Li_2O). This composition corresponds to a maximum in the liquid-solid curve as depicted the phase diagram (Fig. 1.1). For the congruent composition, the melt and the growing crystal are identical with respect to composition, so these crystals show the highest uniformity in chemical and physical properties. On the contrary for other growing techniques, such as stoichiometric crystals, the composition of the melt and the crystal differ slightly during growth, so that the crystal becomes non-uniform, particularly along the growth axis.

Several physical and optical properties, like the phase transition temperature, the birefringence, the photovoltaic effect and UV band absorption edge, strongly depend on the ratio between the concentration of lithium and that of niobium [13]. This is why the congruent composition is preferred and stoichiometric wafer are not available in commerce.

At room temperature a $LiNbO_3$ crystal exhibits a mirror symmetry about three-fold rotational symmetry of the crystal. These symmetry operations classify lithium niobate as a member of the space group $R3c$, with point group $3m$. Above the transition temperature it belongs to the centrosymmetric space group $R3m$.

In the trigonal system the definition of the crystallographic axes is not unique and three different cells can be chosen: hexagonal, rhombohedral or orthohexagonal. The orthohexagonal is usually preferred and the tensor components describing lithium niobate physical properties are expressed with respect to the axes of this cell.

The three mutually orthogonal reference axes in the orthohexagonal convention are:

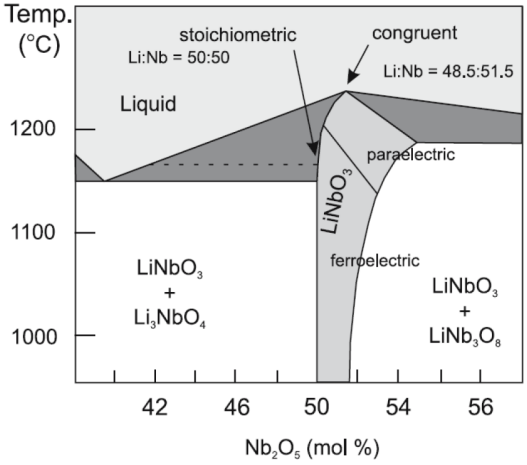

Figure 1.1: Phase diagram of the Li_2-Nb_2O_5 system [14].

- the z-axis (also indicated as c-axis or optical axis) which is the axis around which the crystal exhibits its three-fold rotation symmetry;

- the y-axis, which lays on the mirror plane;

- the x-axis, perpendicular to the previous ones.

Piezoelectricity is proper of z-axis and y-axis and by convention their positive direction is chosen to be pointing on the negatively charged plane under uniaxial compression. Due to the crystal pyroelectricity along the optical axis, z-axis direction is also indicated as that pointing to the positively charged plane while the crystal is cooling.

Commercial wafers from Crystal Technology employed during this work have facets along the circular border perpendicular to the main crystallographic directions in order to be easily oriented.

Lithium niobate structure at temperatures below the ferroelectric Curie temperature ($T_C = (1142.3 \pm 0.7)$°C for congruent composition) consists of planar sheets of oxygen atoms in a slightly distorted hexagonal close-packed configuration (Fig. 1.2). The octahedral interstices formed by this oxygen structure are one-third filled by lithium atoms, one third-third by niobium atoms and one third vacant, following the order Li-Nb-vacancy along the c axis. In the paraelectric phase, above the Curie temperature, the lithium atoms lie in the oxygen planes, while niobium ions are located at the center of oxygen octahedra: this phase therefore presents no dipolar moment.

On the contrary, for temperatures below T_C, lithium and niobium atoms are forced into new positions: Li ions are shifted with respect to the O planes by about 44pm, and the Nb ions by 27pm from the center of the octahedra. These shifts cause the arising of spontaneous polarization.

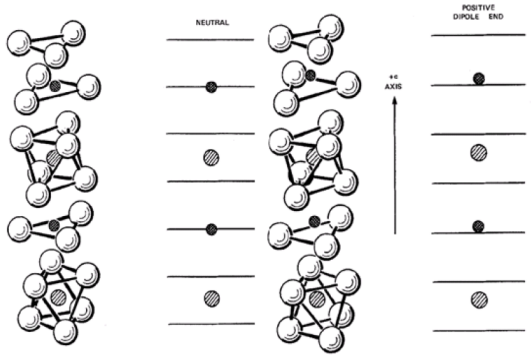

Figure 1.2: Compositional structure of lithium niobate together with the sketched positions of lithium (double cross-hatched circles) and niobium (single cross-hatched circles) atoms with respect to the oxygen planes for the paraelectric (left) and ferroelectric phase (right) [15].

1.2 Defects and Doping

Impurities and structural modifications can considerably modify the physical properties of lithium niobate and are therefore extremely important in the study of this material.

As stated before, congruent lithium niobate has a sub-stoichiometric fraction of lithium which corresponds to the lack of about of the 6% of lithium atomds respect to the stoichiometric composition. Structure modifications are thus needed to ensure charge compensation after Li_2O out-diffusion.

Three different models have been proposed:

- *oxygen vacancy model*: when lithium oxide out-diffusion is compensated by oxygen vacancies as it usually occurs in the oxydes perovskites

$$\langle LiNbO_3 \rangle \rightarrow 2V_{Li}^{+} + V_O^{2-} + Li_2O$$

- *lithium vacancy model*: when some of the lithium vacancies are compensated by niobium atoms (*niobium antisites*)

$$\langle LiNbO_3 \rangle \rightarrow 4V_{Li}^{-} + Nb_{Li}^{4+} + 3Li_2O$$

- *niobium vacancy model*: when both niobium vacancies and niobium antisites concur to reach compensation

$$\langle LiNbO_3 \rangle \rightarrow 4V_{Nb}^{5+} + 5Nb_{Li}^{4+} + 3Li_2O$$

While which of these mechanism prevails is still a question of debate, the oxygen vacancy model seems to be disproved by density measurements [16] which instead confirm the hypothesis of niobium antisites. These substitutional niobium atoms are important since they introduce donor and acceptor levels in the bandgap of the soichiometric crystal giving rise to the photovoltaic and photorefractive effect even in the abscence of extrinsic

impurities. Extrinsic defects were employed since the sixties to tailor lithium niobate physical properties.

Lithium niobate doping is a straight-forward process thanks to its high concentration of vacancies. Dopants can be added both during crystal growth or after the solidification by thermal diffusion or ion implantation.

A few examples of extrinsic defects used to modify the material properties are Fe which enhances the photorefractive effect and Mg, Zr, Zn and Hf that instead reduce the photorefractive effect.

Titanium thermal in-diffusion and hydrogen proton exchange processes are used instead to produce optical waveguides on the surface of the crystal.

Erbium doping can also be exploited to realize integrated laser sources [17].

Parameter	Ordinary	Extraordinary
A_0	$4.5312 \cdot 10^5$	$3.9466 \cdot 10^5$
A_1	$-4.8213 \cdot 10^8$	$79.090 \cdot 10^8$
A_{IR}	$3.6340 \cdot 10^8$	$3.0998 \cdot 10^8$
A_{UV}	2.6613	2.6613
λ_0	223.219	218.203
n	2.2866	2.2028

Table 1.1: Parameters for the generalized Sellmeier equations at room temperature and refractive indices for $\lambda = 632.8$nm

1.3 Physical Properties

1.3.1 Optical Properties

Pure lithium niobate is a transparent crystal presenting a very low absorption coefficient from 035μm to about 5μm. The light absorption coefficient is very sensitive to defects and impurities, while light propagation is weakly affected by scattering with an extinction coefficient of 0.16dB/cm.

Due to the crystallographic structure and the symmetry properties of lithium niobate, its permittivity tensor, in the orthohexanogal cell reference framework, can be represented by a 3×3 matrix:

$$\bar{\epsilon} = \begin{pmatrix} \epsilon_{11} & 0 & 0 \\ 0 & \epsilon_{11} & 0 \\ 0 & 0 & \epsilon_{33} \end{pmatrix} \tag{1.1}$$

The anisotropy of the permittivity tensor leads to the characteristic birefringence of lithium niobate. In fact two different refractive indices can be found in lithium niobate depending on the orientation of the electric field: the ordinary refractive index $n_o = \sqrt{\epsilon_{11}/\epsilon_0}$ for electromagnetic waves polarized perpendicularly to the z-axis of the crystal

and extraordinary refractive index $n_e = \sqrt{\epsilon_{33}/\epsilon_0}$ in the case of a wave with a polarization parallel to the optical axis.

Refractive indices dependence on light wavelenght and crystal composition can be interpolated by the generalized Sellmeier equation [18], which is valid in the wavelenght range $\lambda = 400 \div 3000$nm and for compositions of $C_{Li} = 47 \div 50$mol% to an accuracy of 0.002 in n_i:

$$n_i^2 = \frac{A_{0,i} + A_{1,i}(50 - C_{Li})}{\lambda_{0,i}^{-2} - \lambda^{-2}} + A_{UV} - A_{IR,i}\lambda^2 \tag{1.2}$$

where $i = \{o, e\}$ for ordinary or extraordinary polarization respectively respectively and λ is expressed in nanometers. The intensity factors A desctibe te influence of various oscillators responsible for the refractive indicesin the visible and the near visible and the near infrared region: A_0 for Nb on Nb site, A_1 for Nb on Li site, A_{UV} for high energy oscillators (states in the conduction band, plasmons), A_{IR} for phonons. The parameters at room temperature are listed in table 1.1 together with the typical refractive indices for a congruent composition at a wavelenght of 632.8nm, corresponding to a He-Ne laser. Apart from the Li/Nb ratio, lithium niobate refractive indices depend strongly on extrinsic impurities and this feature can be exploited to tailor n_o and n_e by doping. An example is the titanium in-diffusion for the realization of optical waveguides as it will be explained in chapter 2.

1.3.2 Electro-Optic Effect

The linear electro-optic effect is one of the most important properties of lithium niobate. It consists in the variation of the refractive index due to the application of an electric field according to the relation:

$$\Delta\left(\frac{1}{n^2}\right)_{i,j} = \sum_k r_{ijk}E_k + \sum_{k,l} s_{ijkl}E_kE_l + ... \tag{1.3}$$

where $\Delta(1/n^2)_{i,j}$ is a second rank tensor describing the change in the relative permittivity. The third-rank tensor r_{ijk} and the fourth-rank tensor s_{ijkl} describe the linear and the quadratic electro-optic effect, usually named *Pockel effect* and *Kerr effect* respectively. In lithium niobate the Kerr effect can be neglected since the quadratic electro-optic effect has been observed to be significant only over an applied electric field above 65kV/mm [19].

Due to its symmetry the electro-optic linear coefficients of lithium niobate can be expressed as a reduced tensor[1]

[1]We have adopted the convention {jk} = {11} → 1, {jk} = {22} → 2, {jk} = {33} → 3, {jk} = {23}, {32} → 4, {jk} = {31}, {13} → 5, {jk} = {12}, {21} → 6.

$$r = \begin{pmatrix} 0 & -r_{22} & r_{13} \\ 0 & r_{22} & r_{13} \\ 0 & 0 & r_{33} \\ 0 & r_{42} & 0 \\ r_{42} & 0 & 0 \\ -r_{22} & 0 & 0 \end{pmatrix} \tag{1.4}$$

According to the measurements reported by Bernal *et al.* [20] the values for these coefficients are $r_{13} = 8.6 \cdot 10^{-12}$m/V, $r_{22} = 3.4 \cdot 10^{-12}$m/V, $r_{33} = 30.8 \cdot 10^{-12}$m/V, $r_{51} = r42 = 28.0 \cdot 10^{-12}$m/V. Electro-optic effect is a key-point for integrated optics applications since together with titanium in-diffused waveguides it can be used to realize optical modulators and switches. This characteristic is rather appealing for opto-fluidic applications as well and makes lithium niobate a prime candidate in these studies since it allows for the integration of devices based on this effect with optical waveguides and channels engraved on the material.

The electro-optic effect, together with the photovoltaic effect, is also responsible for the lithium niobate photorefractivity which allows for the local modification of lithium niobate refractive indices by means of a non-uniform pattern of light intensity.

1.3.3 Piezoelectricity

Lithium niobate exhibits also piezoelectricity since it is possible to induce polarization with applied mechanical stress. In particular the induced polarization is:

$$P_i = \sum_{j,k} d_{ijk}\sigma_{jk} \tag{1.5}$$

where σ_{jk} is the second-rank symmetric tensor and d_{ijk} is the third-rank piezoelectric tensor. The stress tensor has 6 independent components since $\sigma_{ij} = \sigma_{ji}$. Moreover the crystal symmetry further reduces the independent components down to 4, which can be expressed in the reduce notation as:

$$d_{ijk} = \begin{pmatrix} 0 & 0 & 0 & 0 & d_{15} & -2d_{22} \\ -d_{22} & d_{22} & 0 & d_{15} & 0 & 0 \\ d_{31} & d_{31} & d_{33} & 0 & 0 & 0 \end{pmatrix} \tag{1.6}$$

Piezoelectric crystals exhibit also the converse piezoelectric effect meaning strain in the crystal appears under the application of an external electric field. The relation between the external field components and the second-rank stress tensor is:

$$S_{ik} = \sum_{i} d_{ijk}E_i, \tag{1.7}$$

where d_{ijk} are again the components of the piezoelectric tensor. The piezoelectric effect of lithium niobate has been effectively exploited to induce acoustic surface waves (SAW)

in the material, which have been used to move droplets on the surface of the crystal [21] or to sort particles in a flowing liquid [22].

1.3.4 Pyroelectric effect

Lithium niobate is a pyroelectric material which exhibits a change in the spontaneous polarization as a function of temperature. The relation between the change in temperature (ΔT) and the change in the spontaneous polarization (ΔP) is linear and can be written as $\Delta P = \bar{p}\Delta T$ where $\bar{p}$ is the pyroelectric tensor. In lithium niobate this effect is due to the movements of Li and Nb ions relative to the oxygen planes and, since their position shifts only along the z-axis, the pyroelectric tensor has the form:

$$\bar{p} = \begin{pmatrix} 0 \\ 0 \\ p_3 \end{pmatrix} \tag{1.8}$$

1.3.5 Photovoltaic Effect

The bulk photovoltaic effect of lithium niobate was discovered in 1974 by Glass *et al.* [23], who observed that a stationary current rises after the crystal was exposed to light. This is an effect typical of non-centrosymmetric crystal by which the momentum of photo-exited electrons has a preferential direction. The result is that a current density j_{phv} is generated by illuminating the crystal:

$$j_{\text{phv},i} = \beta_{ijk} e_j e_k^* I = \alpha k_{G,ijk} e_j e_k^* I \tag{1.9}$$

where β_{ijk} are the components of a third-rank tensor called *photovoltaic tensor*, which can be expressed as the product between the absorption coefficient α and the Glass coefficient k_G; e_j and e_k are the polarization vectors of the incident light wave and I its intensity.

In lithium niobate only four components of the photovoltaic tensor are independent: β_{333}, $\beta_{311} = \beta_{322}$, $\beta_{222} = -\beta_{112} = -\beta_{121}$ and $\beta_{113} = \beta_{131}^* = \beta_{232} = \beta_{223}^*$. The generated current density is mainly directed along the optical axis of the crystal since $k_{G,333} = 2.7 \cdot 10^{-9}\text{cm/V}$ and $k_{G,322} = 3,3 \cdot 10^{-9}\text{cm/V}$, while the generated current along the y-axis is one order of magnitude lower.

1.3.6 Photorefractive Effect

The photovoltaic effect and the electro-optic effect both contribute to an interesting phenomenon in lithium niobate called *photorefractive effect*.

The effect was first observed by Ashkin *et al.* [24] when they noticed the fanning of a laser beam passing through a lithium niobate crystal and they realized that light itself was inducing a change in the refractive index of the material. Since this phenomenon was detrimental for their purposes they called it *optical damage*.

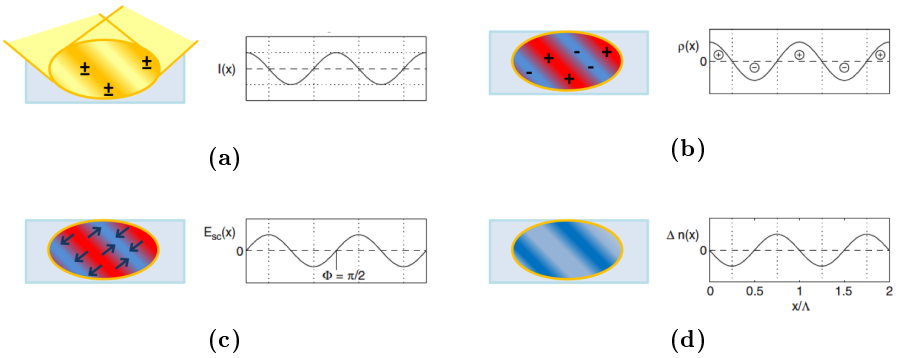

Figure 1.3: Scheme showing the refractive index change mechanism induce by the photorefractive effect after illumination by two interfering beams: (a) electrons in the illuminated areas are exited from the donor level to the conduction band; (b) the electrons are transferred by photogalvanic, diffusion or drift currents in the dark regions where they are trapped by acceptors; (c) an internal electric field arises due to the non-uniform charge distribution; (d) the refractive index changes by electro-optic effect due to the internal electric field.

The photorefractive effect relies on the presence of intrinsic or extrinsic impurities with two valence states. They in fact add intermidiate levels in-between the valence and conduction bands of the pure lithium niobate acting both as donors or acceptors depending on their valence state.

Niobium antisite Nb_{Li} fulfills this role since it can be found both in the Nb^{4+} donor state or in the Nb^{5+} acceptor state. The effect is highly enhanced if the crystal is conveniently doped, for example with iron, which presents the Fe^{2+} and Fe^{3+} states.

When a non-uniform light pattern irradiates the crystal, electrons in the highly illuminated areas are exited from the donor level to the conduction band (Fig. 1.3a). Thanks to diffusion, photogalvanic effect or drift they are transferred in the dark regions where they are trapped by acceptors (Fig. 1.3b). This leads to a non-uniform charge distribution and to the rise in the internal space-charge electric field (Fig. 1.3c). The presence of the space-charge electric field changes the refractive index of the material by the above mentioned electro-optic effect and a refractive index pattern is obtained (Fig. 1.3d).

In the case of Fe doped lithium niobate crystals (Fe:$LiNbO_3$) the phenomenon is described by the one-center charge transport model proposed for the first time in its complete formulation by Vinetskii and Kukhtarev [25]. The equations describing the charge transport are the following:

$$\begin{cases} \dfrac{\partial N_D^+}{\partial t} = (\beta + sI)(N_D - N_D^+) - \gamma n_e N_D^+ & \text{excitation-recombination rate equation;} \\ \nabla \cdot (\epsilon_0 \epsilon \vec{E}) = \rho & \text{Poisson equation;} \\ \dfrac{\partial \rho}{\partial t} + \nabla \cdot \vec{j} = 0 & \text{continuity equation;} \\ \rho = e(N_D^+ - N_A - n_e) & \text{charge density;} \\ \vec{j} = -e\mu_e n_e \vec{E} - \mu_e k_B T \nabla n_e + s k_G (N_D - N_D^+) I \hat{c} & \text{current density;} \end{cases} \tag{1.10}$$

where q and n_e are the charge and the density of the carriers respectively, s the photoionization cross section, γ the recombination constant, μ_e the electron mobility, k_B the Boltzmann constant, T the absolute temperature, k_G the Glass constant, N_D and N_D^+ the densities of filled and empty traps.

The current density is expressed as the sum of three terms due to drift, diffusion and photovoltaic effect respectively.

Photorefractive effect is extremely important in integrated optics applications since it can be exploited to realize holographic Bragg gratings or filters and couple them with waveguides to allow for an integrated mainpulation of light signals.

Chapter 2

Realization and Characterization of Planar Waveguides in Lithium Niobate

Optical waveguides rapresent the basic element in integrated optics devices and optical communication systems. Optical waveguides are defined regions where an electromagnetic wave can propagate and be confined by way of total internal reflection at the waveguide buondaries with minimal energy loss. They can come in a wide variety of shapes and sizes, and the miniaturization of such systems, in the form of thin film waveguides, has been proven to minimize the effects of ambient conditions and the loss of imformation of optical signals while possessing high power densities.

In this chapter we will at first present a simple theory of guided light inside a thin film to illustrate the physical principles and their interesting features. Afterwords, we will describe the state of the art in waveguide fabrication on $LiNbO_3$ and the experimental procedures we used to realize our optical waveguides, with special attention to titanium in-diffusion as the method to produce them. The theory behind diffusion processes in lithium niobate and the techniques and analyses exploited to simulate and characterize our devices will be finally described.

2.1 Theory of Thin Film Waveguides

Wave light theory states that the electromagnetic field in a dielectric medium, with magnetic permeability equal to unity and real relative permittivity tensor $\overline{\overline{\epsilon_r}}$ (non-absorbing medium) is described by the Maxwell equations:

$$\begin{cases} \vec{\nabla} \cdot \left(\bar{\bar{\epsilon_r}} \vec{E} \right) = \rho_l \\ \vec{\nabla} \times \vec{E} = -\dfrac{\partial \vec{B}}{\partial t} \\ \vec{\nabla} \cdot \vec{B} = 0 \\ \vec{\nabla} \times \vec{B} = \mu_0 \vec{j_l} + \dfrac{1}{c^2} \bar{\bar{\epsilon_r}} \cdot \dfrac{\partial \vec{E}}{\partial t} \end{cases} \tag{2.1}$$

Where $\vec{E}$ is the electric field, $\vec{B}$ is the magnetic field density, ρ_l is the charge density, j_l is the current density. In an isotropic medium with scalar permittivity $\epsilon_r(\vec{r})$ function of position, if we assume all electric charges in the medium given by polarization of the dielectric (in the absence of free charges and currents):

$$\begin{cases} \rho_l = 0 \quad \Rightarrow \quad \vec{\nabla} \cdot \vec{E} = -\dfrac{1}{\epsilon_r} \vec{\nabla} \cdot \epsilon_r \vec{E} \\ \vec{j_l} = 0 \quad \Rightarrow \quad \vec{\nabla} \times \vec{B} = \dfrac{1}{c^2} \epsilon_r \cdot \dfrac{\partial \vec{E}}{\partial t} \end{cases} \tag{2.2}$$

one obtains the Helmholtz wave equations for the electric and magnetic field [1]:

$$\nabla^2 \vec{E}(\vec{r}) + \frac{\omega^2}{c^2} \epsilon_r(\vec{r}, \omega) \vec{E}(\vec{r}) + \vec{\nabla} \left(\frac{1}{\epsilon_r(\vec{r}, \omega)} \vec{E}(\vec{r}) \cdot \vec{\nabla} \epsilon_r(\vec{r}, \omega) \right) = \vec{0} \tag{2.3}$$

$$\nabla^2 \vec{B}(\vec{r}) + \frac{\omega^2}{c^2} \epsilon_r(\vec{r}, \omega) \vec{B}(\vec{r}) + \frac{1}{\epsilon_r(\vec{r}, \omega)} \vec{\nabla} \epsilon_r(\vec{r}) \times \left(\vec{\nabla} \times \vec{B}(\vec{r}) \right) = \vec{0} \tag{2.4}$$

Solving either equation 2.3 or 2.4 is sufficient to determine the form of the electromagnetic field in the medium.

In this section we will follow P. K. Tien and R. Ulrich approach to thin film waveguide theory [26]. The thin-film (or dielectric planar) waveguide is a dielectric film sandwiched between two media of refractive indices lower than that of the film: in this stratified medium we will assume that permittivity is constant along planes perpendicular to a fixed Cartesian direction (we will call this special direction z). We will call x the direction parallel to the direction of propagation and y the trasversal direction. Note that when a waveguide propagates inside the film, the dimension of the beam cross section along z is guided by the thickness of the film, but in its other dimension, y, the wave can propagate freely. For a simplified analysis we will assume an incident light beam with infinite extentension in the y direction.

Throughout the following equations we use the subscript 2, 1, 0 for quantities that belong to the sustrate over the film, the film itself, and the substrate below the film respectively, as shown in Fig. 2.1. Quantities at the interface are denoted by double

[1] Assuming a time dependence $\exp(-i\omega t)$ for the electric and magnetic fields and taking the curl of the second and forth Maxwell equation, using the vector identities $\vec{\nabla} \times (\vec{\nabla} \times \vec{A}) = \vec{\nabla}(\vec{\nabla} \cdot \vec{A}) - \nabla^2 \vec{A}$ and $\vec{\nabla} \times (\phi \vec{A}) = \phi(\vec{\nabla} \times \vec{A}) + \vec{\nabla}\phi \times \vec{A}$.

subscripts (12, 10). All interfaces are parallel to the $x-y$ plane. For the two-dimensional analysis used here, $\partial/\partial y = 0$, the equation for the electric field is

$$\frac{\partial^2 E}{\partial x^2} + \frac{\partial^2 E}{\partial z^2} = -(kn_j)^2 E, \qquad j = 0, 1, 2, \tag{2.5}$$

$$n^2 = \epsilon\mu, \qquad k = \frac{\omega}{c} = \frac{2\pi}{\lambda} \tag{2.6}$$

where n_j is the refractive index of medium j, ϵ is the dielectric constant (or permittivity) and μ is the magnetic permeability.

In the special case when the wave is linearly polarized with its electric vector perpendicular to the plane of incidence we shall speak of a transverse electric wave (denoted TE); when it is linearly polarized with its magnetic vector perpendicular to the plane of incidence we shall speak of a transverse magnetic wave (denoted TM). Any arbitrarily polarized wave may be resolved into two waves, one of which is a TE wave and the other a TM wave. Since boundary conditions at a discontinuity surface for the perpendicular and parallel component are indipendent to each other, these two waves will also be mutually indipendent. Moreover, Maxwell's equations remain unchanged when E and $H = \mu B$ and simultaneously ϵ and μ are swapped. Thus any theorem relating to TM waves may immediately be deduced from the corresponding result for TE waves by making this change.

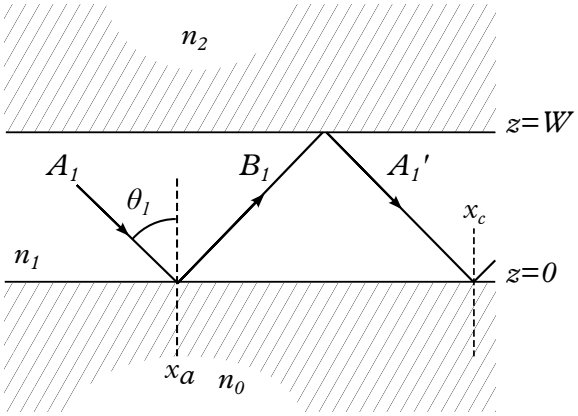

Figure 2.1: Total reflection of an electromagnetic wave inside a thin film waveguide.

For TE waves, we have field components E_y, H_x, and H_z only, and for TM waves, H_y, E_x, and E_z only. The two curl equations for the TE and TM waves are

$$\begin{aligned} H_x &= \frac{i}{k}\frac{\partial E_y}{\partial z}, & H_z &= -\frac{i}{k}\frac{\partial E_y}{\partial x}, \\ E_x &= -\frac{i}{kn_j^2}\frac{\partial H_y}{\partial z}, & E_z &= \frac{i}{kn_j^2}\frac{\partial H_x}{\partial x}. \end{aligned} \tag{2.7}$$

As a consequence of Eqs. 2.7 it is sufficient to consider only E_y for TE waves and H_y for TM waves. We will denote the complex amplitudes of the incident and reflected beams in the film by A_1 and B_1. We use the agreement that all A_j waves propagate toward

the lower right and the B_j waves propagate toward the upper right. When the waves are coupled they all have the same phase constant β along the x axis.

As stated above the thin film has a refractive index n_1 and a thickness W. It is sandwiched between two semi-infinite media of refractive indeces n_0 and n_2. We will assume $n_1 > n_0 > n_2$. We start by considering a wave, A_1 propagating toward its lower boundary $z = 0$ with an incident angle θ_1 on the interface (10) (Fig. 2.1). If θ_1 is larger than the critical angle between n_1 and n_0 ($\sin\theta_c = n_1/n_0$) the A_1 wave is totally reflected into the B_1 wave. Similarly the B_1 wave is totally reflected into the A_1' wave at the upper film boundary (Fig. 2.1). The A_1 and A_1' waves have the common propagation factor

$$\exp(-i\omega t - ib_1 z + i\beta x), \tag{2.8}$$

where

$$b_1 = kn_1\cos\theta_1 \quad \text{and} \quad \beta = kn_1\sin\theta_1. \tag{2.9}$$

Similarly, the B_1 wave has the propagation factor

$$\exp(-i\omega t + ib_1 z + i\beta x). \tag{2.10}$$

The common factor $\exp(-i\omega t + i\beta x)$ will be omitted in all expressions. All A_j waves therefore have the form $\exp(-ib_j z)$ and the B_j waves have the form $\exp(+ib_j z)$ where $j = 1$ denotes the film. The letters C_j and D_j denote the fields in the upper or lower substrate, where $j = 0$ or 2. All of the fields must satisfy the curl Eqs. 2.7. Taking TE waves, as an example, we have for the A_1 (or A_1') waves

$$E_y = A_1 e^{-ib_1 z}; \quad H_x = n_1\cos\theta_1 A_1 e^{-ib_1 z} \tag{2.11}$$

and for the B_1 waves

$$E_y = B_1 e^{ib_1 z}; \quad H_x = n_1\cos\theta_1 e^{ib_1 z} \tag{2.12}$$

where $0 < z < W$. Because of the total reflections the fields in media n_0 and n_2 are exponentially decreasing functions. In the lower substrate, n_0, we have

$$E_y = C_0 e^{p_0 z}; \quad H_x = \frac{ip_0}{k} C_0 e^{p_0 z}; \quad z < 0, \tag{2.13}$$

and in upper substrate, n_2,

$$E_y = D_2 e^{-p_2(z-W)}; \quad H_x = \frac{ip_2}{k} D_2 e^{-p_2(z-W)}; \quad z > W. \tag{2.14}$$

Substituting Eqs. (2.11)-(2.14) into wave equation (2.5), one at a time, we obtain

$$\begin{aligned} \beta = kn_1 \sin\theta_1; \quad b_1 = kn_1 \cos\theta_1, \\ b_1^2 = (kn_1)^2 - \beta^2, \\ p_0^2 = \beta^2 - (kn_0)^2, \\ p_2^2 = \beta^2 - (kn_2)^2. \end{aligned} \tag{2.15}$$

The quantities β, b_1, p_0, and p_2 are real and positive. Otherwise, the waves A_1 and B_1 are no longer totally reflected at the film boundaries and they form radiation modes that will not discussed yet. To match the boundary conditions at $z = 0$ by adding the E field (and also H field) of the A_1 wave in Eq. (2.11) to that of the B_1 waves in Eq. (2.12) and equating the sum to the E field (H field) of the evanescent wave in Eq. (2.13) we obtain

$$\frac{B_1}{A_1} = e^{-i2\Phi_{10}}. \tag{2.16}$$

Similarly by matching the boundary conditions at $z = W$, we have

$$\frac{A_1'}{B_1} = e^{-i2\Phi_{12}}, \tag{2.17}$$

where

$$\tan\Phi_{10} = \frac{p_0}{b_1}, \quad \tan\Phi_{12} = \frac{p_2}{b_1} \tag{2.18}$$

for the TE waves. Similarly, we can show, for the TM waves,

$$\tan\Phi_{10} = \left(\frac{n_1}{n_0}\right)^2 \frac{p_0}{b_1}, \quad \tan\Phi_{12} = \left(\frac{n_1}{n_2}\right)^2 \frac{p_2}{b_1}. \tag{2.19}$$

We choose those solutions Φ_{10} and Φ_{12} of Eqs. (2.18) and (2.19) for which $0 \leq \Phi \leq \pi/2$. The A_1 wave in Eq. (2.16) suffers a phase change of $-2\Phi_{10}$ during the total reflection (while the wave in Eq. (2.17) suffers a phase change of $-2\Phi_{12}$). This has an important effect upon the field distribution in the waveguide: if, for example, $\beta \to kn_1$, then $2\Phi_{12} \to \pi$ in Eq. (2.18). The incident and reflected waves differ by nearly a phase of π, and so they almost cancel at the boundary $z = W$. In accordance with this, p_2 is large and the fields penetrate only little into the medium n_2.

Now we can combine the waves A_1, B_1, A_1' ecc. forming a zigzag path (Fig. 2.1). Because the reflections at both film surfaces are total, the amplitudes A_1' and A_1 can differ only by a phase Δ. After subsequent reflections, the wave has phase differences 2Δ, 3Δ, 4Δ, ... relative to A_1. In general, the superposition of such a set of plane waves is zero, exept when $\Delta = 2m\pi$ with integer m. In that case the beams A_1, A_1' and all further reflections of this beam interfere constructively. We can find the phase difference Δ directly. The phase of the A_1 wave at $x = x_c$ and $z = 0$ is

$$-\omega t + \beta x_c. \tag{2.20}$$

The phase of the A_1' wave at the same point is the phase of the A_1 wave at $x = x_a$ and $z = 0$ plus that of a zigzag. It is

$$-\omega t + \beta x_a + \beta(x_c - x_a) + 2b_1 W - 2\Phi_{10} - 2\Phi_{12}. \tag{2.21}$$

The difference of expressions (2.20) and (2.21) is $\Delta = 2m\pi$. Therefore

$$2b_1 W - 2\Phi_{10} - 2\Phi_{12} = 2m\pi. \tag{2.22}$$

Equation 2.22 is the so called equation of the modes. Since $b_1 W$ is positive and both Φ_{10} and $\Phi_{12} \leq \pi/2$, m cannot be negative. The integer m may then be 0, 1, 2, 3, ... up to a certain finite value, depending on W. This m specifies the order of the mode. Equation (2.22) is the same for both the TE and the TM waves, but the Φ_{ij} differ.

2.1.1 Properties of thin film waveguides

Let $n_0 > n_2$ in the film waveguide in Fig. 2.1. Since β, b_1, p_0, and p_2 are all positive in Eqs. (2.15), possible values of β range from kn_0 to kn_1. In the upper limit ($\beta \to kn_1$), we have $b_1 \to 0$. Thus, from Eq. (2.22), $W \to \infty$. In this case the waves propagate as plane waves parallel to the x axis and for that, the boundaries of the film must be at $z = \pm\infty$. At the lower limit ($\beta \to kn_0$), we have

$$\begin{aligned} b_1 &\to k(n_1^2 - n_0^2)^{\frac{1}{2}}, \\ p_0 &\to 0, \\ \Phi_{10} &\to 0, \\ p_2 &\to k(n_0^2 - n_2^2)^{\frac{1}{2}}, \end{aligned}$$

Therefore the thickness of the film calculated from Eq. (2.22) is

$$W_{\min} = \frac{1}{k}\left[m\pi + \arctan\left(\frac{n_0^2 - n_2^2}{n_1^2 - n_0^2}\right)^{\frac{1}{2}}\right] \cdot \frac{1}{(n_1^2 - n_0^2)^{\frac{1}{2}}} \tag{2.23}$$

for the TE waves. This is the minimum thickness required for a waveguide to support a mode of the order m. For a symmetric waveguide ($n_0 = n_2$) and $m = 0$, $W_{\min} \to 0$, the film can be infinitesimally thin. Equation (2.22) cannot be solved explicitly in β beacause Φ_{10} and Φ_{12} involve trascendental functions. Conversely, however, if we assign a value to β then the quantities b_1, p_0, and p_2 can be calculated from Eqs. (2.15) and (2.18). In addition, if m is given, W can be calculated from Eq. (2.22). It is the thickness of the film required for a mode of order m to propagate with a given phase constant β.

Equation (2.22) can be rewritten as

$$W = W_{10} + W_{12} + mW_1, \tag{2.24}$$

where

$$W_{10} = \Phi_{10}/b_1; \quad W_{12} = \Phi_{12}/b_1; \quad W_1 = \pi/b_1.$$

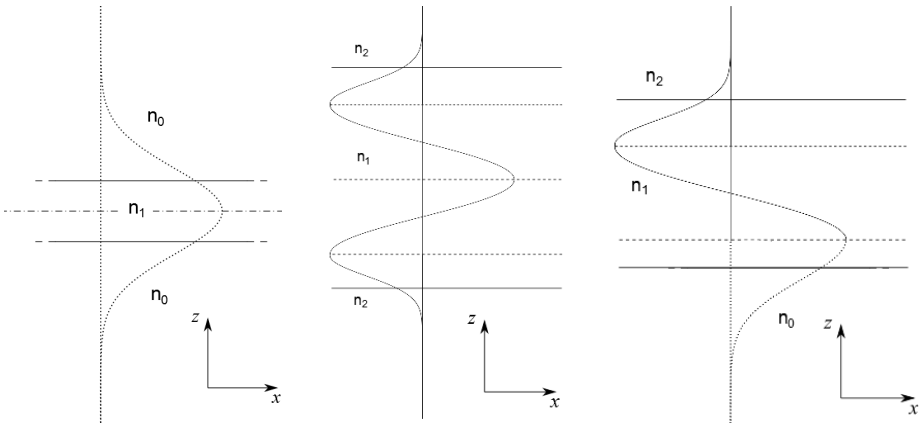

(a) $m = 0$ **(b)** $m' = 2$ **(c)** $m'' = 1$

Figure 2.2: (a) Symmetric waveguide having a phase constant β for a mode of order $m = 0$, (b)symmetric waveguide having phase constant β for a mode of order $m' = 2$, and (c) asymmetric waveguide constructed by combining the lower half of (a) with the upper half of (b).

Equation (2.24) indicates that we can construct an asymmetric waveguide ($n_0 \neq n_2$) of the desired propagation characteristics from two symmetric ($n_0 = n_2$) and ($n_0' = n_2'$) waveguides that have films of identical refractive indices $n_1 = n_1'$ (Fig. 2.2). By combining the lower half of one waveguide with the upper half of the other we obtain an asymmetric waveguide that has the same phase constant β for the mode of order, $m'' = (m + m')/2$. The process can be performed with any combination of m and m', both even. Also notice that, for a given β, the thickness of the film (for the mode order m) is simply that for $m = 0$ plus mW_1 (Fig. 2.3). At the film boundaries, the field amplitudes are $2A_1 \cos\Phi_{10}$ and $2A_1 \cos\Phi_{12}$ respectively.

Finally we can calculate the power carried in a waveguide (we will do so for TE waves only) by integrating the x component of the Poynting vector ($S = E \times H$)

$$(c/8\pi)Re(E_y H_z^*) \tag{2.25}$$

of the total field (A_j and B_j waves) from $z \to -\infty$ to $z \to +\infty$. For a waveguide of unit width in y, this power is

$$P = \frac{c}{4\pi} A_1 A_1^* n_1 \sin\theta_1 \left(W + \frac{1}{p_0} + \frac{1}{p_2} \right). \tag{2.26}$$

Equation (2.26) has a simple interpretation: the quantity $(c/4\pi)A_1 A_1^* n_1 \sin\theta_1$ is the Poynting vector along the x axis for the superposition of the A_1 and B_1 waves. The factor $(W + 1/p_0 + 1/p_2)$ is then an equivalent thickness of the waveguide, W_{eq}, within which the energy of the waves is confined. It is larger than the actual thickness W of the film because the fields extend beyond its boundaries according to $\exp(p_0 z)$ for $z < 0$ and $\exp[-p_2(z - W)]$ for $z > W$. The power density in a film waveguide is inversely proportional to W_{eq} (not W). Hence, even though in a symmetric waveguide the film can

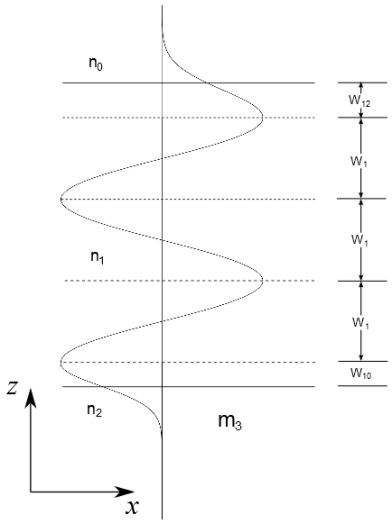

Figure 2.3: Field distribution for the mode $m = 3$ in an asymmetric thin-film waveguide. The thickness of the waveguide may be considered as the sum of W_{10}, W_{12}, and mW_1 which are the widths of its symmetric components

be infinitesimally thin, the power density cannot approach infinity. For $m = 0$, W_{eq} is approximately $\lambda/2n_1 \cos\theta_1$, where λ is the wavelength in a vacuum. The simple form of P in Eq. (2.26) does not apply to the TM waves.

2.2 State of the Art: Optical Waveguides in Lithium Niobate

Lithium niobate is one of the best materials for the realization of optical waveguides thakns to its very low optical absorption (∼0.1dB/cm) in the typical wavelengths employed in telecomunications (between 1260÷1675nm). It is widely used in photonics for the realizatin of waveguides, electro-optical and acousto-optical modulators and switches, non-linear optical frequency converters and diffraction gratings. This applications are possible thakns to the material piezoelectric, electro-optic and photorefractive properties (see chapter 1).

Thermal diffusion of titanium thin films into a substrate is a widely used method to produce waveguides in lithium niobate[27]. Titanium in-diffusion increases the refractive index of the substrate allowing for light to be guided. This technique and its diffusion profile depth can be controlled in such a way as to obtain a very thin waveguide able to support only the fundamental mode, one of the conditions for a high quality waveguide [28]. This ensures that the mode cross section will mantain the same profile at every point in the waveguide, no matter its length.

Several fabrication processes are available for the realization of waveguides in lithium niobate. The most widely spread are:

- **titanium in-diffusion**: it is the most widely used and studied technique in lithium niobate[27] since the mid seventies [29, 30] due to the simplicity and versatility of

the fabrication process, good light confinement along both the extraordinary and ordinary axes and to the fact that in-diffused waveguides preserve the electro-optical properties of lithium niobate [31] allowing for the realization of optical switches and modulators, switches, as well as Mach-Zehnder interferometers and couplers [32, 33].

- **proton exchange (PE)**: it consists in the immersion of lithium niobate in a liquid source of hydrogen ions (usually benzoic acid or toluic acid) at high temperature ($150 \div 400\,°C$) [34]. The refractive index change is due to the substitution of lithium ions Li^+ from the cristal matrix with hydrogen ions H^+ from the liquid phase. In non-linear optics this process is followed by an annealing treatment to achieve higher resistence to optical damage, and this technoque is called Annealed Proton Exchange (APE). Advantages of this technique are a high change in refractive index ($\Delta n_e \approx 0.1$), one order of magnitude higher than Ti in-diffused waveguides, and its simple execution. There are however some drawbacks with this process, namely that only extraordinary polarized modes are supported and that the electro-optical properties of lithium niobate are lost after the proton exchange. Other methods exist to avoid losing these electro-optical properties (Soft Proton Exchange [35] and Reverse Proton Exchange), but these come with a lower refractive index, in the range of $0.01 \div 0.03$.

- **ion implantation**: ion implantation produces a refractive index by way of crystal disruption, up to an order of 0.1. The technique consists in directing ions at fixed energy and incidence angle on the crystal surface. A variety of ions (H, B, C, F, Si, P, Ag) can be emplyed at different energies (Few MeV up to more than 20 MeV) and fluencies ($10^{12} \div 10^{17}$ions/cm^2) [36, 37, 38]. The impacts result in the production of both both point and extensive defects a few microns below the crystal surface. Depending on the ion energy and mass both electronic exitations and nuclear interactions can contribute to the refractive index change of the material [39]. Post-annealing is usually required to recover optical transparency and to eliminate absorption centres generated during the ion implantation. The advantages of this technique are the high refractive index change obtainable in both the ordinary and extraordinary directions and the possibility to obtain 2D patterns by joining beam rastering with photolitographic techniques. The cost of the process and need for huge facilities limited the use of this technique.

- **laser writing**: it is possible to write waveguides in lithium niobate with a laser beam by photorefractive effect or by structural modifications. In the first case *Itoh et al.* [40] demonstrated that the refractive index modifications induced by scanning the crystal with a focused laser beam at a wavelngth of 514nm and a pump of power 70mW were able to light propagating along the ordinary axis and polarized along the extraordinary axis. This technique leads to a considerable increase in n_e of the order of 10^{-3} but they suffer from erasure when exposed to a sufficiently intense laser beam, especially in the visible spectrum. A higher pump power can be employed to impose irreversible structural modification of the crystal structures and obtain a

refractive index change. Femtosecond laser pulses are focused in the region where the waveguide needs to be written and computer controlled step motors move the sample to scan the waveguide region [41]. Depending on the energy employed, the effect is a decrease of n_e only or both n_e and n_o at higher pulse energies. The guided modes are then localized in between the damaged regions. The advantage of this technique is the possibility to realize 3D waveguide patterns in the bulk material and to add couplers and diffracting gratings using the same technique [42]. The main disadvantage is the poor confinement due to the low refractive index change ($\sim 8 \cdot 10^{-4}$)

- **ridge waveguides**: ridge waveguides can be realized by mechanical micromachining [43] and chemical etching [44]. The first tecnique requires computer numerically controlled (CNC) machines operating micro-saws or micro-mills able to produce optical grade surfaces. The chemical approach requires the use of hydroflouric acid as an etchant. Etching speed can be controlled by localized proton exchange [45, 46] or ion implantation in the regions to be engraved. There are more complex techniques to produce ridge waveguides by means of thin film deposition and ion beam micro-milling as in the case of smart guides [47]. Ridge waveguides give the highest confinement due to the high refractive index difference between lithium niobate core and the surrounding material, but the presence of fabrication defects produces scattering that can result in lower efficiency compared to diffused waveguides.

In this work we employed titanium in-diffusion for the realization of our waveguides. The main reasons were as follows:

- the intention to produce waveguides able to support only the fundamental mode (this means waveguides less than 6μm wide for a wavelength of 632.8nm typical of He-Ne lasers used in this work), which ensures that a gaussian light beam propagating in the waveguide will maintain the same profile at every point in the waveguide, no matter its length. This is a fundamental feature for a high quality waveguide when transmitting signals, since it means no loss of information will occur[28].

- the need for a sufficiently high refractive index jump both for y- and z-propagating waveguides. This is required both for versatility and for the perspective to realize a photorefractive Bragg grating along the waveguide. The grating reflects the pump wavelength and could be used to select fluorescent light from molecules dispersed in the fluid flowing in the microfluidic channel perpendicular to the waveguide. Since the writing efficiency of the grating by photorefractive effect is orders of magnitude higher if the wavevector is along the extraordinary axis, z-propagating waveguides are preferred; this is also the reason why proton exchange was excluded [48];

- the availability of all the facilities and instruments needed for the fabrication process (clean room, collimated UV lamp, magnetron sputtering, oven) at the Physics and Astronomy Department of Padua;

- the intention of exploiting techniques both highly reproducible and easy to implement in order to facilitate the future technology trasfer.

2.3 Titanium In-Diffused Waveguides Fabrication

In this section we will give a brief step by step explanation of the experimental procedures used to realize channel waveguides on a lithium substrate. In our case we needed waveguides that support only the fundamental mode of propagation. This ensures that, if the beam coupled to the waveguide is gaussian, the fundamental mode will be gaussian at the exit of the waveguide with no loss of information. If the waveguide is multimodal there will be a superposition of modes at the exit and the information on the shape of the coupled beam will be lost.

The main steps of the process can be summarized as follows:

- a photoresist layer is deposited on the surface of the sample;
- a mask is placed in direct contact with the photoresist layer and exposed to UV light. The photoresist in the unmasked region is eliminated via chemical etching leaving only the masked pattern;
- a thin titanium film is deposited on the patterned surface by sputtering deposition;
- the photoresist layer is removed in a solvent bath leaving only the desired titanium stripes on the crystal surface;
- the titanium is diffused into the crystal by high temperature thermal annealing in an oxygen atmosphere.

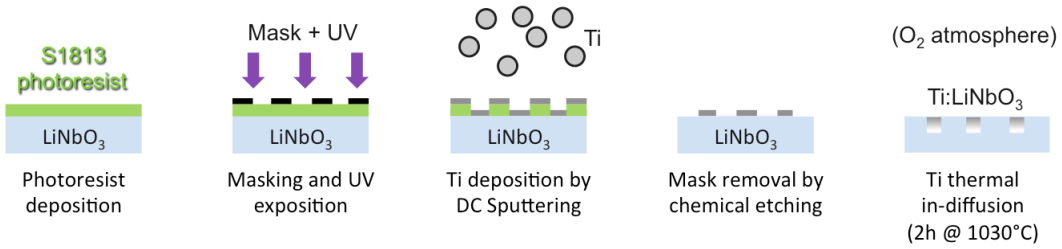

Figure 2.4: Sketch of the main steps for the fabrication of channel waveguides by titanium in diffusion.

Although this is a well-known standard procedure, it required several tests to be optimized.

Samples with planar waveguides were also realized for the characterization of the titanium in-diffusion process by Rutherford Back-Scattering (RBS) and Secondary Ion Mass Spectrometry (SIMS). The procedure was the same with the exeption that these samples did not require the photolitographic patterning.

In the following we present more detailed information for each step, focusing on the optimized conditions used to prepare the final prototype.

2.3.1 Sample Cutting

The first step involves cutting a commercial x-cut wafer of congruent lithium niobate (Crystal Technology, 1mm thickness, polished on both sides) into samples of the desired size. The custs were performed with a South Bay 540 cutting machine, equipped with a diamond-coated Cu-alloy blade. A graduated protractor is used to align the wafer along the crystallographic axes.

Each sample then underwent a sonicating bath in soap and distilled water, isopropanol and fynally acetone for 15 minutes respectively to ensure a clean surface, which is a key condition for photolitographic and sputtering processes.

2.3.2 Photolitography

All the photolitography steps were performed in a ISO 7 class clean-room financed by the MISCHA project (microfluidics laboratory for scientific and technological applications).

The photoresist employed was the S1813 from the Microposit S1800 G2 series. It is a positive photoresist, usually used in micro-litography on silicon, which showed to be be suitable also on lithium niobate. It was chosen for its compatibility with the emission spectrum of the available UV lamp and for its nominal resolution of 0.48μm, suitable for our purposes.

At first the samples were covered with a primer based on hexamethyldisilizane (HDMS) to favour the adhesion of the photoresist oxides. Both the primer and photoresist were deposited by spin coating at a spin rate of 2000rpm for 30s and 6000rpm for 30s respectively. A mask with patterns of stripes with widths (5, 6, 8, 10 μm) was realized by a specilized company (Delta Mask B.V.). It consists in a laser patterned chromium layer 980 on a plate of Soda Lime glass. After the photoresist deposition the samples were put under the mask, clamped in direct contact with it and exposed to UV radiation form a highly collimated UV lamp (300W mercury vapors lamp, $\lambda = 365.4$nm) with an intesity of 9mW/cm^2 for 18s. The photoresist was then developed by dipping in a stirred bath of Microposit Developer MF-300 for 60s and the rinsed in a distilled water bath. The quality and the width of the obtained channels were controlled by optical microscopy and profilometry respectively.

2.3.3 Titanium deposition

Sputtering deposition consists in the deposition on the sample surface of atoms which are removed from a metallic or insulating target after bombardment by the ions of a plasma. The process takes place in a vacuum chamber at a controlled pressure and the plasma is sustained by a potential difference between the target and the rest of the chamber. The potential difference can be supplied by a continous current source or an RF alternating

current source (mandatory for insulating materials). In the *magnetron* sputtering a magnetic field is also present in the proximity of the target due to permanent magnets. These magnets have the aim to confine secondary electrons coming from the collisions between the plasma ions and the target in order to increase the cationic density in the region of the target and allow for a higher sputtering rate. The deposition of titanium film was performed by a magnetron sputtering machine provided by Thin Film Technology. The samples were kept in a cylindrical vacuum chamber at a pressure below $3 \cdot 10^{-6}$mbar, achievable with two subsequent staging: a rotary vacuum pump able to reach the prevacuum pressure of about $8 \cdot 10^{-2}$mbar and a turbomolecular pump to reach the lowest pressure. Argon gas was injected in the chamber through a flow-meter mantaining a pressure if $5 \cdot 10^{-3}$mbar to feed the plasma. The titanium target was connected to a DC power source supplying a power of 40W during the deposition. The target was kept covered by a shield during a pre-sputtering time of 3 minutes in order to remove impurities and oxidized layers on its surface.

2.3.4 Lift-off

The photoresist and the titanium deposited on its surface were removed in a bath of SVC(TM)-14 photoresist stripper at 60°C for several minutes and then under sonication for a few seconds.

2.3.5 Thermal diffusion

The diffusion process was performed in a tubular furnace Hochtemperaturofen Gmbh (model F-VS 100-500/13) by Gero. The sample was positioned on a platinum foil laid in the boat at the end of a quartz rod used to put them at the center of the oven. The channel waveguides were diffused at a temeperature of 1030°C/h for 2h. The heating and cooling rate were kept at 300°C/h and 400°C/h respectively to avoid excessive thermal stresses of the crystals. Oxygen was fluxed inside the oven chamber at a flow rate of 50Nl/h to reduce surface damage after titanium in-diffusion [49]. Unfortunately wet conditions were not possible with the available set-up so that the optimal conditions reported in literature to avoid lithium out-diffusion were not reached.

2.3.6 Lapping and polishing

At the end of the process all samples lateral surfaces were lapped and polished to remove the damages and defects caused by the cutting from the original commercial wafer. The process was carried out with a polishing machine by Logitech. The polishing is performed by putting the samples surface in contact with a rotating disk. The procedure requires three subsequent steps employing an iron disk wet by an aqueous suspension of 3μm alumina particles and finally a polyurethane disk wet by an aqueous suspension of $> 1\mu m$ particles. At the end of the procedure a surface roughness of the order of 1nm is obtained as verified by AFM measurements.

2.4 Titanium In-Diffusion in Lithium Niobate

Titanium in-diffusion is one of the most widely used techniques for the realization of channel waveguides in lithium Niobate, in particular for the fabrication of integrated optical devices [50].

Titanium in-diffusion was studied in detail in the past and the process was found to behave, depending on the temperature, as follows:

- $T \sim 500°C$: titanium is oxidized to TiO_2;
- $T > 600°C$: $LiNb_3O_8$ epitaxial crystallites are formed at the surface together with the simultaneous loss of lithium;
- $T > 950°C$: a $(Ti_{0.65}Nb_{0.35})O_2$ mixed oxide source appears and it acts as the diffusion source for titanium in-diffusion inside the bulk crystal.

Titanium in-diffusion leads to dielectric waveguide layers with graded index profiles which are directly linked to the dopant concentration profile[51], where the refractive index $n(x)$ varies gradually over the cross-section of the guide. Dopant depth concentration profiles can be measured by Secondary Ion Mass spectrometry (SIMS) while for multi-modal waveguides the refractive index can be estimated by m-lines technique.

The measured profile demonstrates that the one dimensional (planar) diffusion process can be described by the standard Fick-type diffusion equation

$$\frac{\partial C(x,t)}{\partial t} = \frac{\partial}{\partial z}\left(D\frac{\partial C(x,t)}{\partial z}\right), \tag{2.27}$$

where C is the titanium concentration, z is the direction normal to the substrate surface, and D is the diffusion coefficient which is a function of C.

The main diffusion parameters, namely the initial thickness of the film and the diffusion temperature and time, have to be tuned in order to obtain a waveguide that supports only the fundamental mode [28]. These parameters were thoroughly investigated in $LiNbO_3$ since it is a widely used material in integrated optics and a variety of papers cover this subject [27, 52, 50]. However these parameters strongly depend on the atmosphere where the diffusion is carried on and on the crystal cut direction. Consequently a clear receipt for in-diffusion is still missing, and published data are almost not reproducible because all the diffusion process parameters are not adequately controlled or reported.

We will briefly describe a few possible reasons for the change in refractive index caused by Ti-diffusion in lithium niobate. We will then introduce a few simple methods of solution of the diffusion equation, useful to understand what kind of diffusion profiles we can expect and to create a model able to fit the experimental data. The diffusion parameters used in these work will be presented in the waveguide realization section.

2.4.1 Microscopic effects of Ti in-diffusion

The microscopic mechanism of the refractive index increase in Ti-diffused crystals were investigated in the past and it was found to be linked to a series of effects: the photoelastic effect, the increase of electronic polarizability and the effect of the change in the spontaneous polarization respectively.

Ti diffuses into $LiNbO_3$ as a result of cationic migration [53]. In the high temperature oxygen enviroment the Ti strip oxidizes forming TiO_2 [52] and consequetly Ti^{4+} ions diffuse into $LiNbO_3$ crystal by occupying vacant Li and Nb sites. A simultaneous inter-diffusion of Li^+ and Nb^{5+} ions into the TiO_2 strip takes place, where Li^+ ions are highly mobile (thus the practice to operate in a wet oxygen atmosphere to prevent the outdiffusion of LiO_2 by neutralizing Li^+ ions as a stable monolayer of LiOH at the surface).

The in-diffusion of Ti ions causes a strain in the crystal caused by the local rearrangement of the crystal structure, and the photoelastic effect consists in the variation of the refractive index due to this strain. It is sufficient to consider only primary strains S_1, S_2, and S_3 in the X-, Y-, and Z-axes respectively. By taking the relative lattice mismatch $|\epsilon_X| = |\epsilon_Y| = \Delta a/a >> |\epsilon_Z| = \Delta c/c$ into consideration (c being the optical axis of the ceystal), changes in the refractive indices at the surface are approximated by:

$$\Delta n_0 \approx -\frac{n_0^3}{2}(p_{11}+p_{12})\epsilon_y, \Delta n_e \quad \approx -n_0^3 p_{31}\epsilon_y, \tag{2.28}$$

where p_{ij} are the photo-elastic coefficients.It was calculated that the refractive index changes due to the photo-elastic effect contributed to about half of the observed index change (about 0.00046 and 0.0014 for the refractive index jump in the ordinary and extraordinary axes respectively at 1050°C of annealing) [29].

Another contribution to the change could come from the incorporation of an ion with an higher polarizability with respect to an element of the matrix. The relation between the refractive index n and electronic polarizability α is given as

$$\frac{n^2-1}{n^2+2} = \frac{4\pi}{3}\sum_i N_i\alpha_i \tag{2.29}$$

where N_i is the number of the ions of type i per unit volume and α_i is the electronic polarizability of the ion i. It was found [29] that Ti ions replaced Nb ions (the preferred replacement due to similar ion charge) of atomic fraction of about 10^{21}cm^{-3} in $LiNbO_3$ crystals. In order to produce a refractive index change $\Delta n = 10^{-3}$, the electronic polarizability of Ti ion, α(Ti), should be larger by $0.04\cdot 10^{-24}\text{cm}^3$ than that of the Nb ion, α(Nb). However, this is not possible since the electronic polarizability of ions has a tendency to decrease as ionic radius becomes small (the effective ionic radius of Ti^{4+} is 0.605Å versus 0.68Å of Li^+ and 0.64Å of Nb^{+5}).

Finally, Ti-diffusion into $LiNbO_3$ can produce a change in the spontaneous polarization ΔP_s tha would produce a refractive index change given by

$$\Delta n_0 = -n_0^3 g_{13} P_s \Delta P_s, \tag{2.30}$$

and

$$\Delta n_e = -n_e^3 g_{33} P_s \Delta P_s, \tag{2.31}$$

Where g is the quadratic electro-optic tensor. This effect could potentially account for changes of the refractive index of the order of 10^{-3}. On the other hand the change in spontaneous polarization will at the same time cause lattice strains through the electrostrictive effect. It was found that if $\Delta P_s < 0$, as required to increase the refractive index, the related strains would have opposite signs to the strains actually observed.

In conclusion, the photoelastic effect seems to be the most likely cause for the index change, but to the best of our knowledge a definitive theory has yet to be formulated.

2.4.2 Constant Diffusion Coeffient Case

General solutions of the diffusion equation usually come in two standard forms: the first is comprised of a series of error functions or related integrals, the second is in the form of a trigonometrical series which converges for large values of time. The two methods are presented here to illustrate the physics behind diffusion processes, and we assume a constant diffusion coefficient for a simpler treatment. In practice it is usually possible to define an effective diffusion coefficient D_{eff} when the diffusion coefficient is dependant on the dopant concentration, and numerical methods are used to simulate realistic concentration profiles.

Plane source

In the case of a plane source and for a constant diffusion coefficient we can rewrite Eq. (2.27) as

$$\frac{\partial C}{\partial t} = D\frac{\partial^2 C}{\partial z^2}, \tag{2.32}$$

which is the equation of diffusion in one dimension. By differentiation the solution is

$$C = \frac{A}{\sqrt{t}} \exp\left(\frac{-z^2}{4Dt}\right), \tag{2.33}$$

where A is an arbitrary constant. The dopant concentration in expression (2.33) assumes a gaussian distribution symmetrical with respect to $z = 0$, tends to zero as x approaches infinity for $t > 0$, and for $t = 0$ it vanishes everywhere exept at $x = 0$, where it becomes infinite. The total amount of substance M diffusing is given by

$$M = \int_{-\infty}^{\infty} C dx, \tag{2.34}$$

and we can write

$$x^2/4Dt = \xi, \qquad dx = 2(Dt)^{\frac{1}{2}} d\xi, \tag{2.35}$$

and substituting

$$M = 2AD^{\frac{1}{2}} \int_{-\infty}^{\infty} \exp(-\xi^2) d\xi = 2A(\pi D)^{\frac{1}{2}}. \tag{2.36}$$

Expression (2.36 indicates that the amount of dopant diffusing remains constant and equal to the amount originally deposited in the plane $x = 0$.
On substituting for A from (2.36) in Eq. (2.33) we obtain

$$C = \frac{M}{2(\pi D t)^{\frac{1}{2}}} \exp\left(\frac{-z^2}{4Dt}\right). \tag{2.37}$$

Expression (2.37) describes the diffusion of an amount of substance M deposited at time $t = 0$ in the plane $x = 0$.

Reflection at a boundary

In the problem just considered half the diffusing substance moves in the direction of positive z and the other half along negative z. However if we have a semi-infinite region in $z > 0$ with an impenetrable boundary at $z = 0$, all the diffusion occurs in the direction of positive z. A simple method to handle this problem is to consider the solution for negative z and reflect it along the $z = 0$ plane, superposing this solution to on the original distribution in the region $z > 0$. The distribution for a semi-infinite cylinder is given by

$$\begin{aligned} C &= \frac{M}{(\pi D t)^{\frac{1}{2}}} \exp\left(\frac{-z^2}{4Dt}\right), \qquad z > 0; \\ C &= 0, \qquad z > 0. \end{aligned} \tag{2.38}$$

Since Eq. (2.37) is linear, the sum of two such solutions is also a solution of the diffusion equation. This means that Eq. (2.38) satisfies the condition that the total amount of diffusing substance M remains constant. We must also consider the additional condition of zero flow across the boundary

$$\frac{\partial C}{\partial z} = 0, \qquad z = 0, \tag{2.39}$$

but since $\partial C/\partial z$ is zero at $z = 0$ in the original solution (2.37), it is still zero after reflection and superposition.

Extended initial distribution

We have considered cases in which the diffusing substance is concentrated initially in a plane. We want to describe what happens when the initial distribution occupies a finite region and we have an initial state defined by

$$\left.\begin{aligned} C &= C_0, \qquad x < 0 \\ C &= 0, \qquad x > 0 \end{aligned}\right\} \quad t = 0; \tag{2.40}$$

The solution can be found by modeling the extended distribution as an infinite number of line sources and superimposing the corresponding infinite number of elementary solutions.

If we consider the diffusing substance in an element of width $\delta\xi$ to be a line source of strength $C_0\delta\xi$, from Eq. (2.37) the concentration at point P, at a distance ξ from the element, at time t is

$$\frac{C_0\delta\xi}{2(\pi Dt)^{\frac{1}{2}}}\exp\left(\frac{-\xi^2}{4Dt}\right), \tag{2.41}$$

and the complete solution due to the initial distribution (2.41) is given integration over $\delta\xi$

$$C(x,t)=\frac{C_0}{2(\pi Dt)^{\frac{1}{2}}}\int_z^\infty \exp\left(\frac{-\xi^2}{4Dt}\right)d\xi=\frac{C_0}{\pi^{1/2}}\int_{z/2\sqrt{Dt}}^\infty \exp(-\eta^2)d\eta, \tag{2.42}$$

where $\eta=\xi/2\sqrt(Dt)$.

Expression (2.42) can be rewritten using a standard mathematical function, the error function, usually written as $\mathrm{erf}(z)$, where

$$\mathrm{erf}(z)=\frac{2}{\pi^{1/2}}\int_0^z \exp(-\eta^2)d\eta. \tag{2.43}$$

with the following properties

$$\mathrm{erf}(-z)=-\mathrm{erf}z, \qquad \mathrm{erf}(0)=0, \qquad \mathrm{erf}(\infty)=1. \tag{2.44}$$

Using this properties we can derive the expression for

$$\frac{2}{\pi^{1/2}}\int_z^\infty \exp(-\eta^2)d\eta=\frac{2}{\pi^{1/2}}\int_0^\infty \exp(-\eta^2)d\eta-\frac{2}{\pi^{1/2}}\int_0^z \exp(-\eta^2)d\eta=1-\mathrm{erf}z=\mathrm{erfc}z, \tag{2.45}$$

where erfc is the error function complement. The solution of the diffusion equation (2.42) is the written as

$$C(x,t)=\frac{1}{2}C_0\mathrm{erfc}\frac{x}{2\sqrt{Dt}}. \tag{2.46}$$

We se from this equation that $C=\frac{1}{2}C_0$ at $x=0$ for all $t>0$.

The error funtion appears in the solution of a diffusion problem as a consequence of summing the effect of a series of line sources, each yielding an exponential distribution.

We can also study the diffusion of a substance initially confined in the region $-h<x<+h$. Here the integration is from $x-h$ to $x+h$ leading to

$$C=\frac{1}{2}C_0\left\{\mathrm{erf}\frac{h-x}{2\sqrt{Dt}}+\mathrm{erf}\frac{h+x}{2\sqrt{Dt}}\right\} \tag{2.47}$$

which is symmetrical about $x=0$.

Finite systems

If the column of diffusing material is of finite length l, the condition that the concentration tends to zero as $x \to \infty$ is to be replaced by the condition that there is no flow of diffusing substance through the top surface

$$\frac{\partial C}{\partial x} = 0, \qquad x = l. \tag{2.48}$$

This condition is satisfied if the concentration curve is considered to be reflected at the boundary and the reflected curve superimposed on the original one. In the finite system the concentration curve reflected at $x = l$ is reflected again at $x = 0$, and then at $x = l$, and so on, with each successive reflection superimposed on the original curve shown in Eq.2.47. The complete expression will be an infinite series of error functions or error functions complements so that

$$C = \frac{1}{2} C_0 \sum_{n=-\infty}^{\infty} \left\{ \mathrm{erf} \frac{h + 2nl - x}{2\sqrt{Dt}} + \mathrm{erf} \frac{h - 2nl + x}{2\sqrt{Dt}} \right\} \tag{2.49}$$

Expression (2.49) is useful for calculating the concentration distribution in the early stages of diffusion. In this case, keeping the first few terms of the series gives sufficient accuracy for most practical purposes.

2.4.3 Experimental analysis

Our group fabricated functional channel waveguides both y- and z-propagating. After the initial tests we chose to focus on the realization of z-propagating waveguides to allow for the future integration of a Bragg grating on the waveguide exploiting the photorefractive effect (described in section 1.3.6), since this property is highly enhanced if the grating wavevector is directed along the optical axis of the crystal.

In order to find the best experimental parameters for the realization of z-propagating channel waveguides a calibration of the diffusion process was performed by measuring the deposited titanium dose with *Rutherford Backscattering Spectrometry* (RBS) and the diffused profile with *Secondary Ion Mass Spectrometry* (SIMS).

Finally a finite element method simulation was employed to calculate the guided modes.

2.4.4 RBS and SIMS Characterization

RBS was used to measure the titanium surface concentration of the thin film deposited by sputtering. Titanium films were deposited on silica substrates by sputtering technique and measured at the Legnaro National Laboratories (LNL-INFN). The incident beam was a 2MeV proton beam and the silicon solid state detector was placed at 170° with respect to the incident beam with a detection angle of 1.966mstrad.

In Fig. 2.5 we report the RBS spectra from a titanium film of (41 ± 5)nm deposited on a SiO_2 substrate at the same conditions used for the final realization of the waveguides. The Ti peak is sharp due to the very small thickness of the deposited film and it is clearly

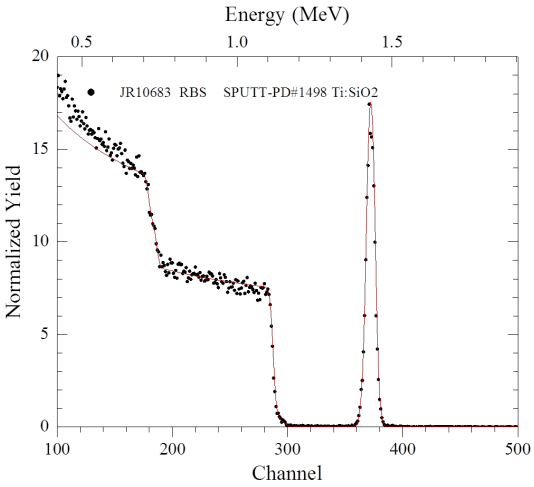

Figure 2.5: RBS spectrum of an as-deposited sample of Ti on a silica (SiO_2 substrate.

distinguishable from the background signal consisting in the backscattering spectra from Si and O atoms (the Si spectra being at higher energy than the O_2 one). The fit of the experimental data gave a titanium surface concentration of $150 \cdot 10^{15}$atoms/(cm^2·s) and a titanium concentration in the sputtered film of $(4.1 \pm 0.1) \cdot 10^{22}$atoms/cm^3. From the RBS spectrum it was also deduced that the sputtered layer was partially oxidized, with an approximate composition $TiO_{0.8}$. However this does not affect the diffusion process because, during the thermal treatment, the titanium film is completely oxidized at a temeperature of about 500°C before starting in-diffusion.

After the complete diffusion process carried out at 1030°C for 2h, the titanium concentration in the first microns below the surface was investigated by Secondary Ion Mass Spectrometry using a CAMECA ims4f.

A 10kV Cs^+ primary beam was used to sputter the surface of the sample kept at -4.5kV (so that the final 14.5keV impact energy was delivered). Negative secondary ions detection was exploited together with electron gun compensation of the charge build-up occurring in insulators.

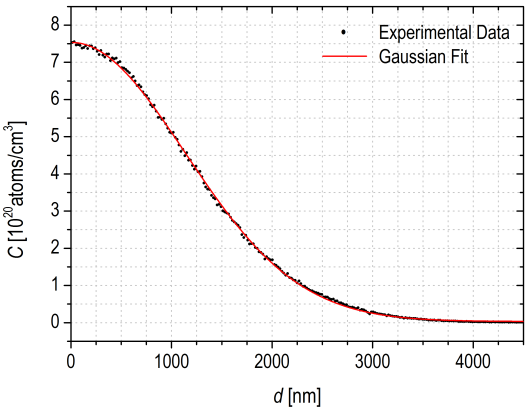

Figure 2.6: Concentration profile obtained from the SIMS measurement of a 37 ± 1nm titanium film on a x-cut $LiNbO_3$ substrate after diffusion in O_2 at 1030°C for 2h.

A typical concentration profile as a function of the sputtered depth is reported in Fig. 2.6 . The profile refers to the diffusion of the titanium film obtained with the same parameters in the numerical simulation described in the following section.

2.4.5 Numerical Simulation

A numerical simulation of the diffusion process was implemented to find the best parameters for the titanium in-diffusion starting from the surface concentration C_0 and the diffusion coefficient D obtained by the joint RBS and SIMS measurements.

The simulation was developed by dr. Nicola Argiolas and further refined by dr. Giacomo Bettella with COMSOL Multiphysics®. The main purposes of the simulation were to state the upper limit of the titanium stripes width to ensure single mode in-diffused waveguides and give the effective refractive index of such a mode.

The simulation software assumes a linear medium ($\vec{D} = \epsilon\vec{E}, \vec{B} = \mu\vec{H}$) and time-harmonic oscillation of the electric and magnetic fields ($\vec{E}, \vec{B}$) in order to simplify Maxwell's equations to the following equations:

$$\begin{aligned} \nabla \times \left(\frac{1}{\mu}\nabla \times \vec{E}\right) - \omega^2\epsilon_c\vec{E} = 0, \\ \nabla \times \left(\frac{1}{\epsilon_c}\nabla \times \vec{H}\right) - \omega^2\mu\vec{H} = 0, \end{aligned} \tag{2.50}$$

where $\epsilon_c = \epsilon_r + i\frac{\sigma}{\omega\epsilon_0}$, with ϵ_r the relative permittivity and σ the electrical conducibility. If $\nabla \cdot \vec{E} = 0$ there is no need to solve for the magnetic field $\vec{H} = \nabla \times \vec{E}/(i\omega\mu_0)$ and using the relation $\epsilon_r = n^2$ for non-conducting ($\sigma = 0$) and not ferromagnetic materials ($\mu_r = 1$) the equation to be solved is

$$\nabla \times (\nabla \times \vec{E}) = k_0^2 n^2 \vec{E} \tag{2.51}$$

that is the equivalent of equation (2.5) in vector form. Assuming a z-propagating waveguide, the z component of the electric field is assumed to be an harmonic function of z so that $\vec{E}(x, y, z) = \vec{E}(x, y)e^{-ik_z z}$.

The program solves equation(2.51)as an eigenvalue problem with the eigenvalues given by k_z from which the effective indices $n_eff = \omega/k_z$ of the confined modes of the waveguide are derived.

In this way it was possible to simulate the confined modes in a z-propagating waveguide diffused from a titanium stripe of width w on the surface of an x-cut crystal.

The refractive index variation $n(x, y)$ needed as imput for the simulation can be expressed as a function of the titanium concentration according to $n_0(x, y) = n_0 + K_{n_0}C(x, y)^{\gamma_0}$ or $n_e(x, y) = n_e + K_{n_e}C(x, y)$ [54, 55]. The concentration was modeled as the product between a Gaussian profile across the direction perpendicular to the crystal surface (x) and the sum of two error functions on the y direction, as in the case of a diffusion from a finite source of width w in one dimension:

$$\frac{C_0}{2}\exp\left(-\frac{x^2}{4Dt}\right)\left[\mathrm{erf}\left(\frac{1}{\sqrt{4Dt}}\left(\frac{w}{2}-y\right)\right)+\mathrm{erf}\left(\frac{1}{\sqrt{4Dt}}\left(\frac{w}{2}+y\right)\right)\right] \tag{2.52}$$

where $t = 2\mathrm{h}$ is the diffusion time, D is the diffusion coefficient calculated from the SIMS measured profile and C_0 is the titanium concentration at the surface obtained from the normalization of the SIMS profile area with the dose measured by RBS. The results from the simulation are discussed together with the near field images in the following section.

2.5 Near Field (NF) Setup and Measurements

A Near field experimental setup was built in order to couple the waveguides to a laser source and to measure the near field image of the mode sustained and its output intensity.

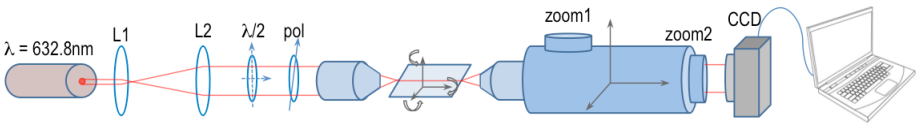

Figure 2.7: Scheme of the near field setup.

The setup is sketched in Fig. and includes:

- a laser source consisting of a He-Ne laser at a wavelength of 632.8nm with a nominal power of 4mW;
- a half-wave plate and a polarizer to turn and select the polarization of the source in order to exite both the TE or TM modes of the waveguide;
- two confocal lenses used to increase the laser beam width from 1mm up to 4mm, as wide as the entrance pupil diameter of the objective, to minimize the beam spot waist at the focus of the objective;
- a 20× objective to focus the laser beam before the coupling to the waveguide;
- a three-dimensional translation and rotation stage to move the sample, with a 1μm travel resolution and a 10' rotation resolution respectively;
- a microscope in horizontal position with a 20× objective with a long working distance (1.2cm) and two different zoom levels, moved by a three dimensional translational and rotational stage;
- a LaserCam-HR camera by Coherent Inc. to record the near field image.

To explain the setup we will refer to the crystallographic directions of the sample with the z direction parallel to the waveguides aligned along the focused beam, x will be the direction orthogonal to the sample surface and y the direction parallel to the saple surface and perpendicular to the light beam.

The beam in the proximity of the objective focus was characterized by sampling the beam cross section intesity profile at different distances with the camera. Both the projection on the x- and y-axis of the recorded two dimensional profiles where fitted by a Gaussian to calculate the beam width and verify the profile shape (Fig. 2.8). The beam width $W(z)$ as a function of the distance z from the focus (in the case of a focused Gaussian beam) can be fitted by the following function:

$$W(z) = W_0\sqrt{1+\left(\frac{z}{z_R}\right)} \tag{2.53}$$

where W_0 is the Gaussian beam waist (the minimum beam width at the focus), and z_R is the Rayleigh range at which $W = W_0\sqrt{2}$.

From the fit we obtained the waist W_0 and the Rayleigh range reported in Fig. 2.8. The values obtained from the two different orthogonal projection are compatible so that we can consider their average as the best estimation. From those parameters we can also estimate the numerical aperture of the beam:

$$\begin{aligned} W_0 &= (11.3 \pm 0.6)\mu\text{m} \\ z_R &= (65.5 \pm 4)\mu\text{m} \\ NA &= \frac{w_0}{2z_R} = 0.09 \pm 0.01 \end{aligned} \tag{2.54}$$

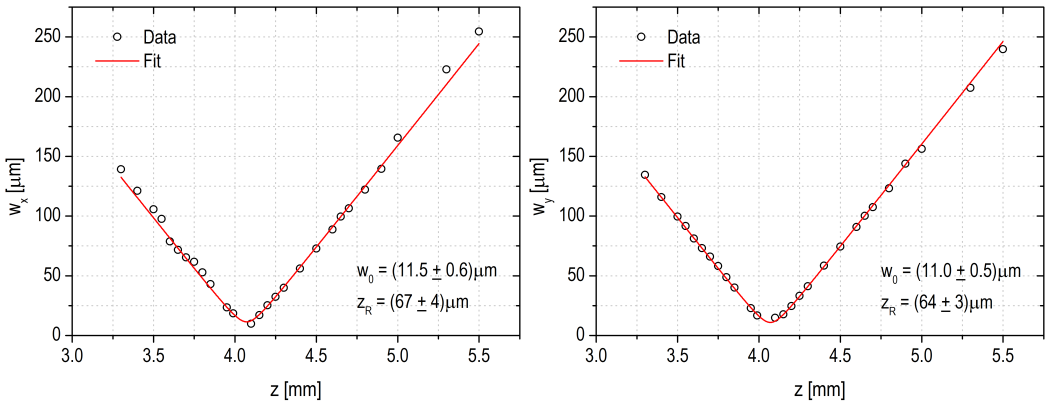

(a) a **(b)** b

Figure 2.8: Characterization of the Gaussian beam employed to exite the waveguides. Both the projections on the xz (a) and yz (b) planes as a function of z are fitted by the function of Eq. (2.53).

To achieve the maximum intensity transfer from the laser beam to the waveguide one would need to use an objective with a numerical aperture smaller than that of the waveguide and with a beam waist of the same dimensions of the waveguide field distribution.

A rough estimate of a graded index waveguide can be obtained by defining an effective numerical aperture NA_{eff} from the maximum refractive index value in the core n_{max} and

the refractive index of the cladding n_{clad}, as is usually made for graded index fibers. For a z-propagating waveguide we have:

$$NA_{eff} = \sqrt{\frac{n_{max}^2 - n_{clad}^2}{2}} = \sqrt{\frac{(n_0 + K_{n_0} C_0^{\gamma_0})^2 - n_0^2}{2}} = 0.13. \tag{2.55}$$

Although the beam waist is larger than the waveguide dimensions, the aperture of the objective is smaller than the effective aperture of the waveguide. An objective with a smaller beam waist would have a larger numerical aperture, so we preferred to match the numerical aperture rather than the beam waist to reduce intensity variations due to small translational mismatch.

We present a few near field images of various waveguides of different widths, direction of propagation and number of modes and the comparison with simulated data 2.9.

2.6 Waveguide Intensity Loss

A series of measurements have been carried out to obtain the intensity loss per unit length of our waveguides[2].

A set of 6 optical waveguides built on a single 23.00×18.00mm rectangular lithium niobate chip, with the waveguides parallel to the longest edge. The waveguide transmission was measured using the near field setup, with a beam splitter placed before the coupling optics to monitor the laser beam stability and a photo-diode in place of the CCD camera for an integrated measure of the intensity exiting the waveguide.

The experimental protocol was as follows:

1. the first waveguide was coupled with the laser pump ($\lambda = 632.8$nm, TE mode) and the total transmitted intensity was recorded by the photo-diode connected to a lock-in amplifier;

2. the transmitted intensity of the other five waveguides was recorded;

3. the chip was removed and then replaced on the holder and realigned as in point 1, recording only the signal from the first guide. This procedure was repeated 10 times to obtain an estimation of the error committed during alignment procedures;

4. the sample was lapped using the same procedure described in section 2.3.6 in order to reduce its length. Once the desired sample length had been reached and good optical surface quality of the polished lateral face had been achieved, the whole procedure was repeated starting from point 1.

The transmission of all six waveguides was measured for seven different length from 23.00 ± 0.01mm down to 7.266 ± 0.010mm. The intensity of the transmitted beam by

[2]The measurements were taken by Dr. Anna Zaltron and Rita Scolaro of the $LiNbO_3$ group of the Department of Physics at the University of Padova

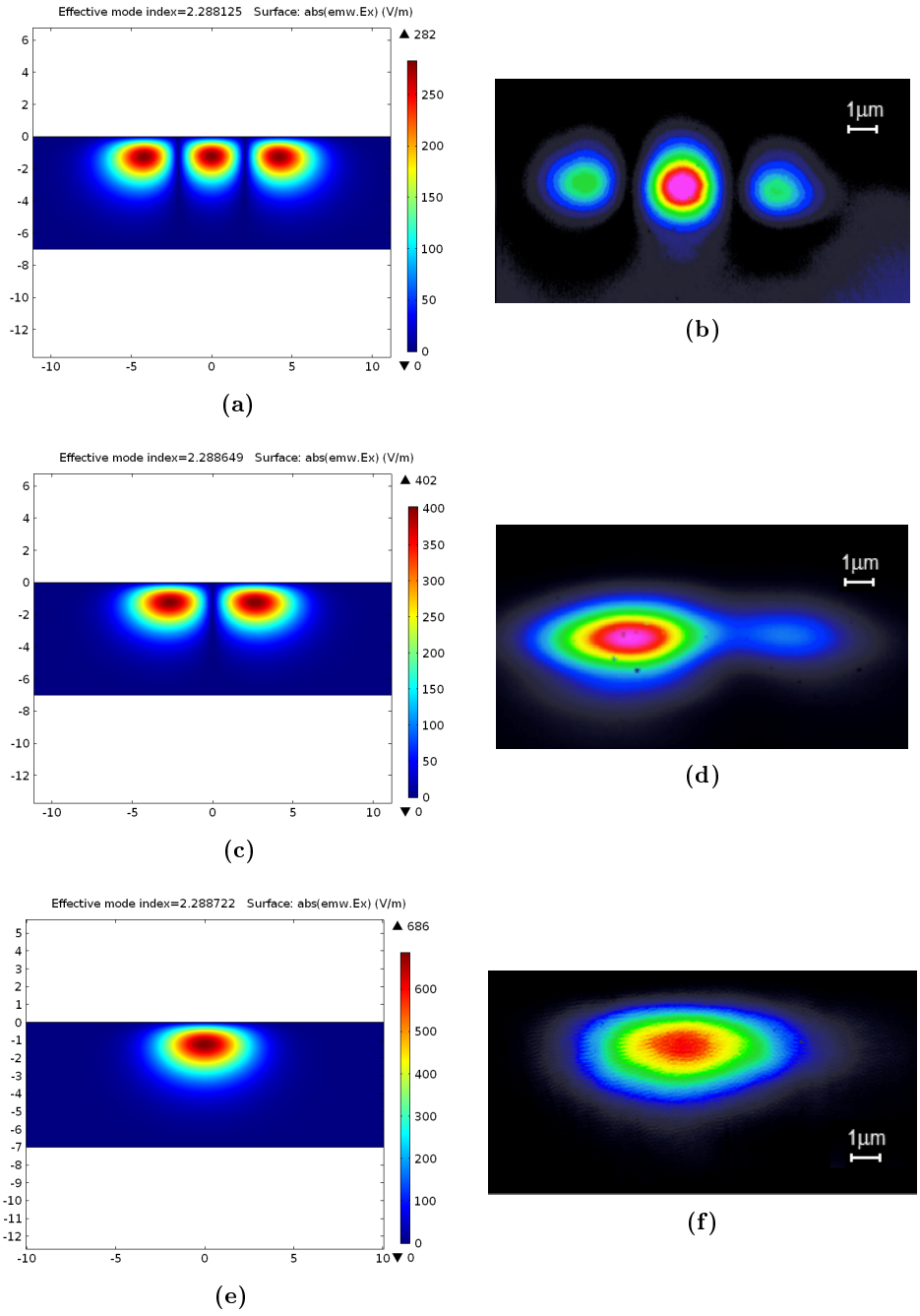

Figure 2.9: Examples of characteristic TE modes predicted by the simulation and measured with the near field setup, for waveguides of different nominal widths: (a), (b) 11.5mum, (c), (d) 10μm, (e), (f) 5μm. The images from the simulation show the electric field modulus of the highest order mode. Modes of order higher than the first do not perfectly match the simulated modes because the end-butt coupling makes the exitation of a single mode difficult, so that the near field images may rapresent a composition of different modes. The abscissa expresses the distance from the center of the waveguide in μm.

way of the optical waveguide recorded at its length, I, was measured depending on the waveguide length L. In particular, the results were fitted using the equation:

Waveguide	α[dB/cm]
1	11 ± 3
2	3 ± 2
3	8 ± 2
4	4 ± 3
5	4 ± 3
6	16 ± 1

Table 2.1: Attenuation coefficients α for the six tested waveguides.

$$I = y_0 + I_0 e^{-\alpha(L-L_0)}, \tag{2.56}$$

which is the standard formula for the transmitted intensity I, where I_0 is the laser beam intensity in front of the waveguide, α is the attenuation coefficient, L is the crystal length and y_0 is a fitting parameter which was found to be compatible with zero within one σ.

The attenuation coefficient α gives the attenuation per unit length of the waveguide and is usually reported in logarithmic scale as:

$$\alpha[\text{Db/cm}] = log_{10}\left(e^{-\alpha}\right) = 4.34 \cdot \alpha_{fit}. \tag{2.57}$$

The resulting values of α are reported in table 2.1 and take into account both scattering and absorption losses. The errors are those resulting from the fits multiplied by 4.34. The best waveguides have an attenuation coefficient of about $3 \div 4$Db/cm. The high values of α obtained for the first and sixth waveguides are probably due to imperfections in the titanium stripes introduced during the photolitographic process (likely due to border effects which reduced the quality of the photolitographic patterns along the borders) or during the lift-off process (small sections of the Ti stripes could have come off during this process leading to interruptions in the waveguide). As a matter of fact, the mentioned processes are more critical at the border of the samples, and the introduced imperfections could significantly increase surface and volume losses.

Only a few studies have been reported in literature concerning the losses of optical waveguides realized in lithium niobate by Ti-in-diffusion for wavelengths in the visible range. Ramabadran and Jackson[56] reported a series of measurements using Raman microprobe microscopy where the light intensity is detected at an angle of 90° from the optical propagation direction (i.e. in scattering mode) while scanning the entire optical waveguide length. In this configuration they measured an attenuation coefficient of $3.03 \div 1.75$dB/cm at λ =514.5nm (TE mode) for their y-propagating waveguides. Irrera and Valli[57] instead reported a series of measurements using a prism-coupling technique, where an incident laser beam is coupled to a prism so that the laser beam is totally reflected at the surface of the prism in direct contact with the waveguide. In this way, the vanishing electromagnetic field at the surface of the prism is coupled with the waveguide to exice

different modes. They reported an attenuation coefficient of 2dB/cm at λ =632.8nm (TE mode) for x-propagating waveguides. Therefore, our results are comparable with those found in literature, but there is still room for improvement. Adjustments in the diffusion process (in terms of diffusion time and temperature) and in the titanium dose could lead to improvements in the overall waveguides efficiency.

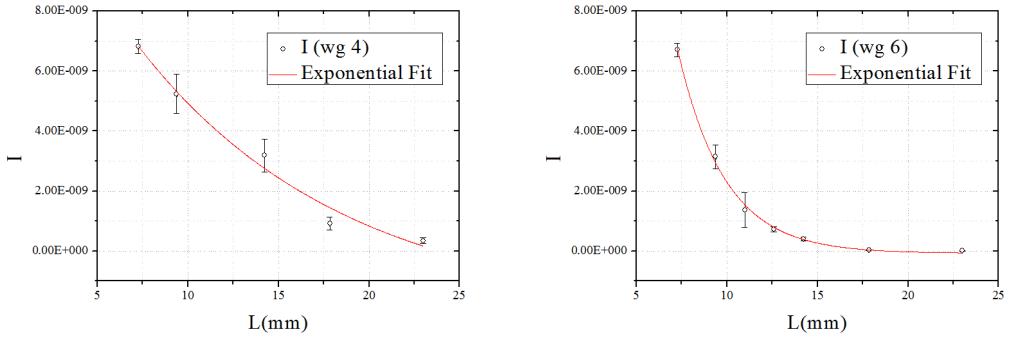

Figure 2.10: Plots of the intensity I as a function of the waveguide length L for (a) waveguide 4 and (b) waveguide 6

Chapter 3

Cross-Junction Droplet Generators in $LiNbO_3$ for Lab-on-a-Chip Devices

3.1 Microfluidics and Lab-on-a-Chip technology

Microfluidics studies the behaviour of extremely small amounts of fluids, with typical volumes ranging from microliters down to picoliters, usually flowing inside confined geometries with a length scale of tens of micrometers or less.

The first attempts to handle small amounts of liquids in the nanolitre and picolitre range date back to the 1950s [58] but it was the 1980s that saw the realization of the first microfluidic channels, thanks to micromachining techniques inherited from silicon microelectronics. Efforts were then made to create other miniaturized devices such as the first miniaturized gas chromatograph (GC) by Terry *et al.* on a silicon wafer [59] and other microfluidics structures such as microvalves and micropumps [60, 61].

The new millennium has brought forth a true boom in microfluidics technology thanks to polymeric materials, which allowed for the realization of cheap, flexible and easy to produce prototypes of microfluidic devices [62, 63].

In addition, with the broadening of possible fields of application came the need to support both microfluidic stages and optical or electronic ones. This also marks the birth of the Lab-on-a-chip concept.

Lab-on-a-Chip (LOC) technology has become in recent years one of the most promising concepts in applied physics which aims to transfer all laboratory operations into small, portable devices. The main reason for this success is that microfluidics provides extreme control of the manipulated samples and a very low reagents consumption, while allowing for high throughput and easily scalable complexity of the devices without a significant increase in the device overall size. This features, with the aforementioned possibility to integrate optical or electronical stages in the same device are the ingredients that make LOC technology possible.

The microfluidic channels of these devices are usually made from polymeric materials such as PDMS or PMMA and obtained by moulding on masters realized by photolito-

graphic techniques [62, 63]. The very small size of the channels and the typical flow rates employed lead to low Reynolds number [1] (Re$<$ 100), that is laminar flows, as well as large values of the Peclet number [2]: those are key to reach high control both in space and time over the transport of chemicals or biological species [64, 65, 66].

Even though polymers are preferred, since they are easier to shape and are almost inexpesive, they present a few drawbacks, such as swelling, nonspecific bioadhesion and degradation. This resulted in renewed interest in more expensive materials as an alternative to polymers, such as silicon or glass [67, 68], which are more stable at high pressure conditions and are vastly more durable since they do not suffer deterioration like polymerich materials. These materials rise to the challenge of making devices suitable for biological and medical application, as well as being prime substrates for the integration of multiple stages able to perform multiplexed analysis of liquid samples. Many micro-devices have already been realized but the challenge to integrate all of this devices into a single multi-purpose micro-device free of all external macro add-ons has yet to be won. In fact, when operating in microfluidics, one still needs macro syringe pumps or pressure controllers to operate, as well as microscopes for the analysis of the samples.

In this thesis we will describe our attempt at realizing an integrated opto-microfluidical platform on lithium niobate, which allows for the integration on the same material of a microfluidic stage consisting in a droplet generator for the handling of the samples, and an optical stage consisting in a thin film strip waveguide for their analysis.

Lithium niobate is also biocompatible [69] and was also proven to be a suitable material for the realization of pumping micro-systems [21, 7, 70], fluid manipulation devices [71, 72] and optical circuits [73], making it a prime candidate in the pursuit of a fully integrated Lab-on-a-Chip device. The first demonstration of its use in microfluidics to host microfluidic prototypes however is dated back in 2014 by the pioneeristic work of the $LiNbO_3$ group of Padova [12, 74].

3.2 Droplets Microfluidics

The world at low Reynolds numbers behaves very differently from our daily experience: the typical regime is laminar flow which has the peculiarity that no mixing happens between different fluids because there can be no turbolence or convection, and the only mixing mechanism is molecular diffusion. This is a very slow process across the typical distances insiade a microfluidic channel, and this means that performing fast reactions inside a microfluidic chip is not feasible under normal conditions.

In addition, the combined effects of laminar flow and the boundary conditions stating

[1] The Reynolds number measures the ratio of inertial forces to viscous forces with the expression $\mathrm{Re} = \frac{\rho u L}{\mu}$, where ρ is the density of the fluid, u is its mean velocity, L is the characteristic linear dimension of the flow and μ is the fluid dynamic viscosity.

[2] The Peclet number measures the ratio of advective transport rate to diffusive transport rate with the expression $\mathrm{Pe} = \frac{Lu}{D}$, where L is the characteristic linear dimension of the flow, u is the mean velocity and D the mass diffusion coefficient of involved species.

that the fluid velocity must be zero at the solid walls of the channel lead to parabolic velocity profiles. The velocity gradient along the direction perpendicular to the flow leads to inhomogenities of the injected liquid compounds distribution and consequently to poor control on the concentration of the flowing reagents.

Droplet microfluidics answers this problems: the idea is to confine the fluid of interest, called *dispersed phase* (which could contain chemical reagents, molecules or biological samples) inside droplets immersed in another immiscible fluid phase which carries the droplets along the microfluidic channel, called *continuous phase*.

The main advantages of this setup are:

- if the reactants inside the dispersed phase fluid are not soluble in the continuous phase fluid, they will not diffuse outside the droplet, eliminating reactant losses or dispersion along the channel. Droplets can therefore act as isolated chemical reactors allowing fine and safe control of chemical reactions or as sealed carriers for biological samples, even single cells [75], allowing for high throughput cell-based screening;
- droplets can be kept separated or merged, allowing maximum control on when and how reaction and mixing happens, if at all [76, 77, 78];
- two mixing mechanism take place inside the droplet, namely a fast unsteady convection in which the mass transfer is controlled by a recirculation motion, and the slow molecular diffusion. These mechanisms ensure the uniformity of reactants concentration inside the droplet and result in faster reaction times [79];
- the droplets can be driven, manipulated and sorted by employing particular channel geometries [80, 81], mechanical actuators [82], electric fields [83, 84, 85], acoustic waves [7], optical beams [72, 86, 87] so that parallel droplet processing or even droplet based logical operations can be made [77].

Droplet microfluidics thanks to these features widely broadened the range of possible applications of microfluidic technology and has already showed its potential in a variety of examples, of which we cite a few such as chemical synthesis [88], the manipulation of single cells or DNA strings [75, 89] and drug delivery and screening [90, 91].

3.3 Droplets generation

There are a variety of techniques to produce droplets inside microfluidic channels, taylored around different applications. The requirement for any of them is primarily a high reproducibility and very low dispersion of droplets volume distribution, . Other common requirements are high production frequency, the ability to mantain a steady droplet generation over a wide volume range and the possibility to use different fluids in the same device.

We can divide droplet generation methods into two broad categories: *passive* and *active* methods. Passive methods rely only on the interaction between two immiscible

fluid costrained in a confined geometry, and does not require any active contribution to the creation of droplets from the dispersed phase other than that needed to make the fluids flow inside the channels. The size and shape of the droplets are controlled just by tuning the inlet fluxes of the injected fluids. These methods exploit on particular geometrical designs of the microfluidic channels, on a suitable choice of fluids employed and on the wettability properties of the channel materials (which can be tailored with proper surface functionalization methods). The main advantages lie in the simpler device production method and in the highly monodispersed droplet generation, which can be controlled simply by changing the fluxes of both the dispersed and contnuous phases.

Active methods on the other hand rely on an external source of energy to form the droplets, essentially providing enough energy to the dispersed phase for a new interface surface to be formed. These methods include mechanical actuators such as valves [92], external electric fields [93, 94], focused laser beams [95], piezoelectric actuators [96] and pyroelectrodynamic shooting [97]. These techniques usually provide a faster response in tailoring the droplet size than passive methods and in certain cases can even generate droplets on demand [98, 99], but it is not always possible to integrate these systems on the same substrate on which the microfluidics channels are engraved, and they come with more sophisticated technologies and higher costs, so passive methods are generally preferred in the abscence of very specific needs.

In our work we chose a passive method of generation (namely a T-junction or cross-junction setup) since it was the cheapest and most straight-forward way to produce a working microfluidic droplet generator in lithium niobate without renouncing to droplet size control, throughput and monodispersion. It is however worth mentioning that lithium niobate has been selected as the material of choice for the integration of a number of active methods of droplet generation and manipulation. Lithium niobate is in fact a piezoelectric material and it has already been used as an external source of surface acoustic waves in polymeric base microfluidic chips [21, 70, 71]. In addition, as explained in the previus chapter, it is also one of the best materials for the realization of optical stages able to interact with droplets [95]. Electrodes can be easily realized on its surface by photolitography and metal evaporation techniques to exploit its electro-optic, piezoelectric and pyroelectric properties [73]. Finally, localized electric fields can also be produced thanks to the formation of a space charge distribution by laser beam irradiation due to the photorefractive effect and it has already been shown that these fields can be used to manipulate droplets [9, 72].

3.3.1 Passive droplet generators

All passive droplet generators are controlled by setting different fluxes for the continuous phase Q_c and the dispersed phase Q_d, usually controlled by employing a syringe pump for the fluid injection, or by setting the inlet pressures p_c and p_d, in which case one can use pumps with pressure regulators and flux meters for a more precise control of the injected flux rates.

As stated before the most important feature in passive droplet generators is the geometry of the channels in the region where the droplets are produced. On the basis of the flow near pinch-off we can classify the passive generators as follows:

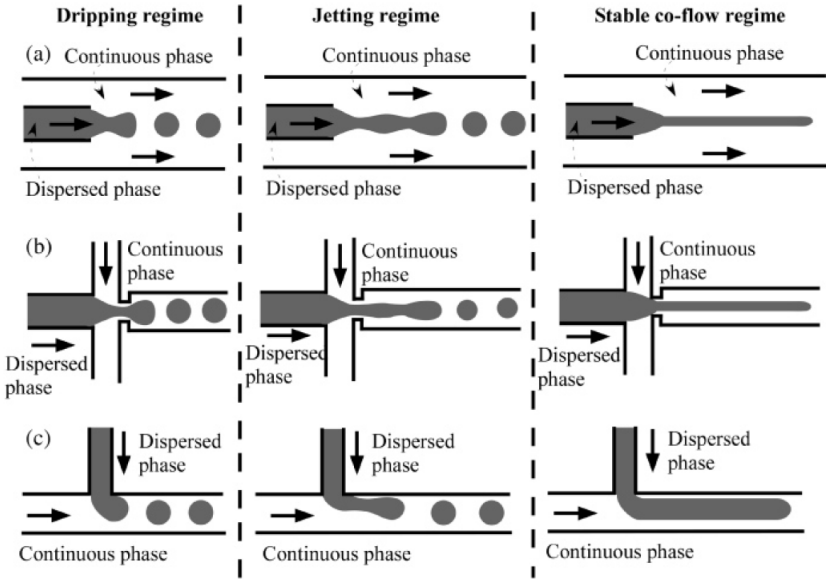

Figure 3.1: Sketch of three passive droplet generators geometries: (a) *co-flowing*; (b) *flow-focusing*, (c) *cross-flowing*. The three different operational regimes are shown from left to right: *dripping*, *jetting* and *coflow*.

- **co-flowing**: this geometry is characterized by two coaxial channel. The inner channel where the dispersed phase flows comes to an end, ejecting the dispersed phase inside the outer channel containing the countinuous phase. After an initial stage where the two phases flow together, droplets are generated by Rayleigh-Plateau instability. This is one of the first methods for droplet generation [100], now replaced by more stable configurations;

- **flow focusing**: dispersed and continuous phase are forced into a narrow region where the continous phase shrinks the dispersed phase until pinch-off is reached. This geometry is very stable over a wide range of droplet production frequencies (easily reaching frequencies of the order of 1kHz)) and it is one of the most used and studied techniques. However it has a few disadvantages, such as its higher fabrication complexity. In addition its operational principle relies mainly on shear stress, and the resulting volume and frequency of the droplets produced depend heavily on parameters and properties of the fluid of interest (such as its viscosity ratio $\lambda = \mu_d/\mu_c$), making it not suitable an approach when trying to design an all-purpose chip where different fluids are expected to be employed.

- **cross-flowing**: the inlet channel containing the dispersed phase crosses at a wide angle the main channel where the continuous phase is flowing. In this case the dispersed phase obstructs the main channel, shrinking the continuous phase stream

break-up takes place and the droplet is formed. Different geometries following this principle have been studied, such as T-junctions, Y-junctions or multiple junctions [101, 102, 103].

In general the important parameters for all of these systems are the densities of the injected fluids (ρ_c, ρ_d), their viscosities (μ_c, μ_d) their surface tension (σ) on the fluxes of the respective phases (Q_c, Q_d), on their wettability properties and consequently on their contact angle with the channel surfaces (θ_c, θ_d). As these parameters are varied one can distinguish three different regimes (Fig. 3.1):

- **co-flow**: in this regime no droplets are formed: the two phases flow parallel to each other undisturbed. This is typical when the fluid velocities are small, especially when the interfacial tension between the two fluids is high and they have similar viscosities. In particular, for the cross-flowing geometry, this regime can be favored by a high wettability of both continuous and dispersed phase on the channel walls. This is why a wetting continuous phase and a non-wetting dispersed phase are ideal for droplet production;
- **jetting**: this regime presents an initial unstable co-flowing thread, with the dispersed phase that breaks-up after the instability grows too large, forming the droplets. This regime allows for the fast production of small droplets but, due to its unstable nature, has a wider dispersion in droplets volumes;
- **dripping**: this regime produces highly monodispersed droplets at a high frequency and steady rate. It is therefore the most studied regime and the one most devices are designed on. The droplet break-up is dominated by the viscous force exerted by the continuous phase on the dispersed phase;

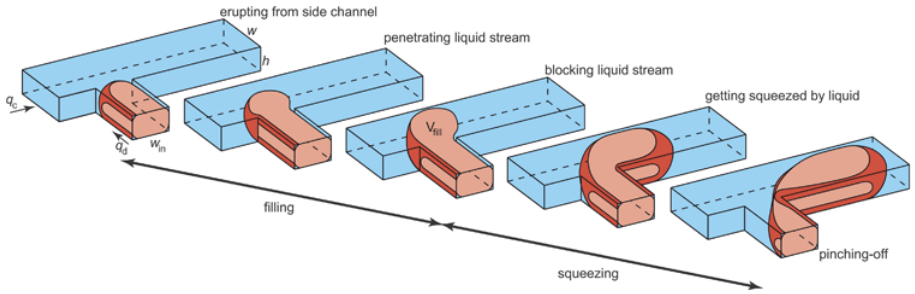

Figure 3.2: Sketch of the different stages of droplet generation in a T-junction operating in the *squeezing* regime. The dispersed phase emerges from the side channel, progressively filling the main channel until it is completely blocking the continuous phase flow; the pressure build-up squeezes the dispersed phase upstream, shrinking the neck until break-up takes place [104].

Although these are the main flowing regimes, in cross-flowing geometries (T-junctions in particular) another regime is possible, called *squeezing*, where the dispersed phase completely obstructs the main channel before break-up occurs (Fig. 3.2). In this regime larger

droplets, called *plugs*, are formed, which enterely fill the main channel. This is the regime of choice in our work: our aim is to illuminate the channel via a waveguide which lies within a micron of the substrate surface, crossing the upper region of the microfluidic channel, which is at least 100μm deep. When the plug completely fills the channel, the diffused phase can be more easily illuminated: smaller droplets would flow at the center of the channel below the waveguide level. Cross-flowing geometries (T-junction and cross-junction) will be the central topic of this reaserch concerning the microfluidic stage of our device.

3.4 T-junction

The characteristic geometry of a T-junction, as the name suggests, consists in a main microfluidic channel with a secondary channel that intersects the main channel at a right angle. In the standard setup the continuous phase flows in the main channel while the dispersed phase flows in the secondary channel. Usually both channels have the same height h but may have different widths w_c and w_d, depending on the desired droplet size. Syringe pumps are the most common instrument for fluid injection in the channels, since they provide fine control over the volume rates Q_c and Q_d of both phases and consequently over actual droplet size. Alternatively, pressure controllers can be employed, and in this case flowmeters are added downstream to have a feedback on the actual injected fluxes.

Droplets are produced thanks to the forces exerted by the continuous phase on the dispersed phase intering the main channel. The continuous phase at the junctions flows faster since the channel is partially obstructed by the dispersed phase and both are steady flows. With an increase in the continuous phase velocity at the junction comes a reduced pressure on the channel walls and on the dispersed phase itself, which starts to occupy a progressively wider portion of the main channel. The effect is an increase both in shear forces proportional to the continuous phase velocity, and the force driven by the pressure drop across the emerging droplet. The process concludes when these forces overcome the capillary force keeping the disperse phase attached to the dispersed phase thread, and the final result in the droplet break-up (Fig. 3.2).

The balance between the mentioned forces determines the regimes of *dripping* or *squeezing*. In the *dripping* regime the main contribution to droplet pinch-off is given by the shear viscous force while in the *squeezing* regime the droplet break-up is driven primarily by the pressure drop between the tip and the neck of the dispersed phase thread, since it obstructs the main channel increasing the reistence to the flow of the continuous phase.

An important parameter in microfluidics is the capillary number C_a, which rapresents the ratio between viscous shear stress and capillary pressure:

$$\mathrm{Ca} = \frac{\mu_c u_c}{\sigma} \tag{3.1}$$

where μ_c and u_c are the viscosity and the average velocity of the continuous phase and σ is the interfacial tension. C_a is useful to determine the regime in a microfluidic system.

The greater C_a is, the higher is the contribution of viscous shear forces on the break-up of the dispersed phase. If C_a is small the viscous shear force is not the main force opposing the capillary force and other mechanism arise. In the following we present a few models proposed in literature to describe the droplet generation process inside a T-junction.

3.4.1 Theoretical model for the T-junction

Liquids and fluid flow are generally treated as a continuum i.e. as a macroscopic physical object whose volume has a characteristic length much grater than the distance between its molecules. All domain boundaries are given as sharp boundaries, neglecting molecular diffusion of a phase into another one so that, in three dimensional problems, boundaries are two dimensional surfaces. All molecular interactions are therefore neglected and their effect is taken into account by capillarity, expressed as a surface tension force.

The equation of motion of a single newtonian[3] incompressible[4] fluid is described by the Navier-Stokes equation. Together with the continuity equation, they completely describe the flow of the fluid:

$$\frac{\partial \vec{u}}{\partial t} + (\vec{u} \cdot \nabla)\, \vec{u} + \frac{1}{\rho}\nabla\rho = \frac{\mu}{\rho}\nabla^2\vec{u} + \vec{F}, \tag{3.2}$$

$$\nabla \cdot \vec{u} = 0, \tag{3.3}$$

where $\vec{u}$ is the fluid velocity field, ρ is the density of the fluid, μ is the viscosity; p the pressure and $\vec{F}$ expresses the external forces acting on the fluid.

In the case of microfluidics the Reynolds number is very low (usually $\mathrm{Re} \lesssim 1$) so inertial forces can be neglected. Gravity can also be neglected since its contribution is usually much lower than that of viscous forces.

For a single fluid one usually sets no-slip conditions at the boundaries: this means that fluid velocity next to the walls is assumed to be zero, or more precisely $\vec{u} = \vec{u}_{wall}$ i.e. the fluid flows at the same velocity of the boundary walls in their immediate proximity.

In the case of two fluids one has to account for a series of additional effects and interactions: buoyancy ($\rho_1 \neq \rho_2$), different viscosities, and the interface between the fluids respectively.

The Navier-Stokes equations will be valid for both fluids separately but new buondary conditions have to be formulated to describe their interaction and the behaviour of their interface. A good approximation to describe such a system is to write the viscosity μ as a function with a discontinuity at the boundary Γ between the two phases (and similarly ρ if $\rho_1 \neq \rho_2$). The interfacial tension σ is included as a force term of the form $\vec{F}_\sigma = \sigma\kappa n\vec{\delta}_\Gamma$ which again presents a discontinuity (κ is the curvature of the interfacial surface). The Navier-Stokes then becomes:

[3]For Newtonian fluids the stress tensor τ is assumed to be a linear function of the rate of strain $\epsilon = 1/2\left(\nabla\vec{u} + (\nabla\vec{u})^T\right)$; in the case of an incompressible fluid $\tau = 2\mu\epsilon$, where μ is the fluid viscosity

[4]For an incompressible fluids we have $\rho(x,t) = \rho = constant$, where ρ is the fluid mass density; the continuity equation $\partial\rho/\partial t + \nabla\cdot(\rho\vec{u}) = 0$ reduces to $\nabla\cdot\vec{u}$

$$\frac{\partial \vec{u}}{\partial t} + (\vec{u} \cdot \nabla)\, \vec{u} + \frac{1}{\rho}\nabla\rho = \frac{1}{\rho}\nabla \cdot (2\mu\epsilon) + \sigma\kappa\vec{n}\delta_\Gamma, \qquad \nabla \cdot \vec{u} = 0. \tag{3.4}$$

These equations can be solved by numerical simulations such as lattice Boltzmann (LBE) [105, 106, 79], volume of fluid (VOF) [107], or by computational fluid dynamics methods (CFD) [108] but these techniques imply huge calculations to be solved for each set of geometrical and physical properties of the case under study.

We would therefore like to formulate simple scaling laws to roughly estimate the droplet volumes and production frequency of a droplet generator, making it easier and faster to plan for the realization of a microfluidic chip. These scaling laws are also very useful to understand the physical principles involved in two-phase cross-flow at the microscale. Since the beginning of the century both experimental measurements and numerical simulations have been explored to understand the behaviour of these systems but a unique simple formulation able to predict droplet size and frequency reliably still lacks. In the following we will present the main theoretical models proposed in the recent past and the scaling laws describing the production of droplets in the T-junction geometry. These will form the basis for the discussion of the experimental results obtained in our work.

The first attempt to give a physical explanation to the scaling behaviour of droplet volume was provided by Thorsen *et al.* [101] who suggested that droplets are sheared off from the stream of the dispersed phase with a size determined by the balance between pressure approximated as $p_L \approx 2\sigma/r$, r being the characteristic radius of curvature of the liquid-liquid interface, and the shear stress acting on said interface which can be expressed as $\tau \approx 2\mu_c u/\epsilon$, where ϵ is the characteristic radius of the gap between the dispersed phase enetering the channel and the channel wall. Equating this two terms, one can estimate the characteristic droplet size as $r \approx \sigma\epsilon/\mu_c u$.

A more detailed analysis of the problem was carried out by Garstecki *et al.* [102] who were the first to indicate the capillary number Ca as the parameter to distinguish between the squeezing and dripping regimes. In fact, they indentified three main forces acting on the tip of the discountinuous phase during break-up: the surface tension force and the shear stress force found by Thorsen, and a third force arising from the pressure drop associated with the resistance to the flow of the continuous fluid around the immiscible tip. They found that at low capillary numbers this third term is the dominating destabilizing force overcoming the interfacial forces at the break-up while the shear stress forces can be neglected. This was later confirmed by a simulation performed by De Menech *et al.* [109] who set the critical separation value at Ca = 0.015: at higher values of Ca the droplet break-up is dominated by the viscous shear stress and smaller droplets are produced, while at lower Ca the the squeezing pressure dominates and the generated droplets occupy the entire width of the channel.

Garstecki *et al.* also found that the size of the droplets is determined solely by the ratio of the volumetric rates of flow Q_d/Q_c of the two immiscible fluids and not on by the relation between the Lapalce pressure and the shear stress, as claimed by Thorsen. They

were also the first to indicate the capillary number C_a as the parameter to distinguish between the squeezing and dripping regimes.

Finally, they postulated a scaling relation for the droplet length L along the stream direction in the squeezing regime:

$$\frac{L}{w_c} = 1 + \alpha \frac{Q_d}{Q_c} \tag{3.5}$$

where w_c and w_d are the widths of the main channel and the inlet channel respectively and α is a constant of order one depending on the geometry of the T-junction ($\alpha \approx w_d/w_c$ and in their experiment the channels had equal widths). The reasoning behind this scaling law starts from the evidence that, in the squeezing regime, we can identify for steps for the droplet break-up:

1. the tip of the discontinuous phase enters the main channel;
2. the growing droplet spans the whole cross-section of the main channel ($\epsilon \ll w_c$);
3. the droplet elongates in the downstream direction and the neck connecting it to the inlet thins;
4. the neck breaks, the disconnected droplet flows downstream and the tip of the discontinuous phase recoils back towards the inlet.

After the droplet completely obstructs the main channel, it is pulled by the continuous phase for a time $t_{squeeze}$ needed to shrink the droplet neck until break-up. The velocity at which the neck shrinks is approximately equal to the average velocity of the continuous phase u_c so that $t_{squeeze} \simeq w_d/u_c = w_d w_c h/Q_c$ and the additional length gained by the droplet during this time is $L = w_d Q_d/Q_c$. Dividing this relation by w_c we obtain Garstecki's scaling law.

This postulated scaling law was justified on a theoretical basis and extended to an intermediate squeezing-to-dripping regime by Christopher *et al.* [110]. They modeled the tip of the dispersed phase thread depicted in Fig. 3.3 as a spherical shape with radius b connected to the disperse phase by a neck of width s, with $s = w_d$ at the beginning of the droplet generation process.

The perliminar analysis is similar to that of Garstecki regarding the forces involved in the break-up process. The result is a scaling law for the droplet length. The involved forces, while being the same as those listed by Garstecki, are given different expressions base on Christopher's analysis:

- the capillary force is given by the difference between the Laplace upstream and downstream of the emerging droplet, multiplied by the projected area of the emerging interface bh:

$$F_\sigma \simeq \left[-\sigma \left(\frac{2}{b} + \frac{2}{h} \right) + \sigma \left(\frac{1}{b} + \frac{2}{h} \right) \right] bh = -\sigma h \tag{3.6}$$

where the average curvature at the upstream end of the droplet is calculated as the sum of the curvature in the plane of the T-junction $2/b$ and the curvature in the outplane section $2/h$. Similarly the curvature at the downstream end of the dispersed phase tip is given by the sum of an approximated curvature $1/b$ somehow smaller than the curvature of the advancing tip and the same curvature on the out-plane section $2/h$;

- the drag force due to the viscous shear stress applied on the emerging interface:

$$F_\tau \simeq \mu_c \frac{\partial u}{\partial y} bh \simeq \mu_c \frac{u_{gap}}{w_c - b} bh \simeq \mu_c \frac{Q_c b}{(w_c - b)^2} \tag{3.7}$$

where the shear stress rate has been approximated by the average velocity of the continuous phase in the gap between the liquid-liquid interface and the wall of the channel divided by the gap $(w_c - b)$ between the wall and the tip;

- the squeezing pressure force obtained from a lubrication analysis [111] for the pressure-driven flow in a thin gap with aspect ratio $(w_c - b)/b$:

$$F_p \simeq \Delta p_c bh \simeq \frac{\mu_c u_{gap}}{w_c - b} \frac{b}{w_c - b} bh = \frac{\mu_c Q_c b^2}{(w_c - b)^3}. \tag{3.8}$$

During the droplet growth the viscous shear stress and the squeezing pressure increase until when they overcome the capillary force opposing droplet pinch-off. The hypothesis of Christopher *et al.* is that the break-up starts when these forces balance:

$$F_\sigma + F_\tau + F_p = 0 \qquad \Rightarrow \qquad ((1 - \bar{b})^3 = \bar{b} \cdot \mathrm{Ca}, \tag{3.9}$$

where $\bar{b} = b/w_c$; b is then the droplet length reached before the neck starts to shrink under the push of the continuous phase. The additional length gained by the droplet during the shrinking process can be obtained by multiplying the droplet speed during growth $u_{growth} \approx Q_d/(bh)$ by the time needed to shrink the neck $t_{squeeze} \approx w_d/u_c \approx w_d w_c h/Q_c$ so that the final length of the fully formed droplet, rescaled by w_c, results:

$$\bar{L} = \bar{b} + \frac{\Lambda}{b}\phi, \tag{3.10}$$

where $\Lambda = w_d/w_c$ and $\phi = Q_d/Q_c$. The approximated rescaled volume of the droplet is then

$$\bar{V} = \frac{V}{w_c^2 h} = \bar{L}\bar{b} = \bar{b}^2 + \Lambda\phi. \tag{3.11}$$

Although this model successfully predicted the observed dependence of the volume of the Droplets on Ca, the theoretical trend did not trace the experimental behaviour as observed by the authors. In fact they defined a rescaled droplet production frequency (derived from experimental observations) as:

$$\bar{f} = \frac{\mu_c w_c}{\sigma} f \tag{3.12}$$

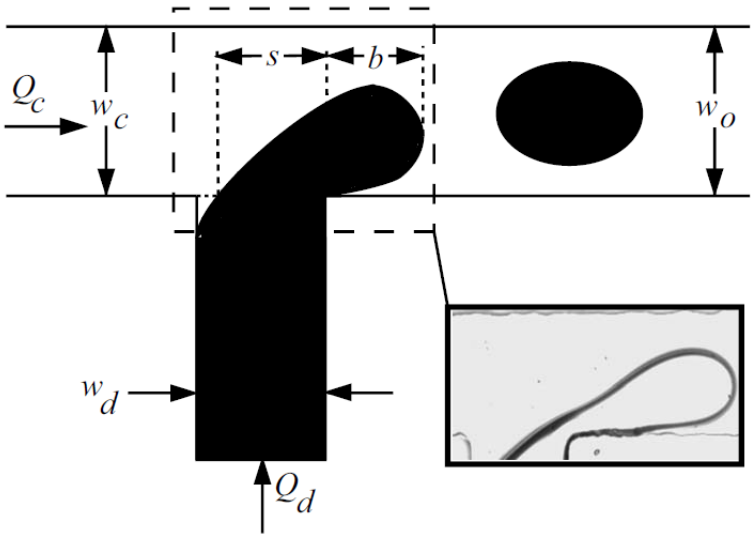

Figure 3.3: Diagram of the emerging droplet taken from the paper by Chritopher *et al.* [110]. The droplet emerges until it reaches a length b and a neck thickness s, as measured from the downstream corner of the T-junction. Cross-flow of the continuous phase liquid then streches the neck of the droplet; during this time the droplet continues to grow due to the injection of the dispersed phase liquid

suggesting a power law dependence of $\bar{f}$ on the capillary number at a fixed ratio ϕ in the range $10^{-3} < \mathrm{Ca} < 5 \cdot 10^{-1}$:

$$\bar{f} \propto \mathrm{Ca}^{1-\delta} \qquad \text{for } \phi = \text{ constant} \tag{3.13}$$

with $(1-\delta)$ experimentally determined to be 1.31 ± 0.03 indipendent of the viscosity of the fluids and on the channel width ratio $\Lambda = w_d/w_c$. Since $\phi = Q_d/Q_c$ was fixed and $Q_d = fV$, where V is the volume of the single droplet, the rescaled droplet volume $\bar{V} = V/(hw_c^2)$ is:

$$\bar{V} = \frac{\phi \mathrm{Ca}}{\bar{f}} \propto \mathrm{Ca}^{\delta}, \qquad \text{for } \phi = \text{ constant} \tag{3.14}$$

with $\delta = -0.31 \pm 0.03$. This power law dependance disagrees both with the theoretical model presented by the authors themselves and with the theory of Garstecki *et al.*.

A significantly different approach based on geometrical considerations was proposed by Van Steijn *et al.* [104] to describe the generation of droplets in the squeezing regime at low capillary numbers ($\mathrm{Ca} < 0.01$) when the width ratio between the amin an the inlet channel is not too small ($w_d/w_c \geq 0.33$).

The volume of the droplet was reconstructed by extrusion from its 2-D projection on the T-junction middle plane. They approximated the upstream border of the neck as a quarter of a circle with radius R and the advancing tip as half a circle with radius $w/2$ while the curvature of the lateral surface of the dispersed phase thread is taken again as a half circle but now with radius $h/2$ (Fig. 3.4)

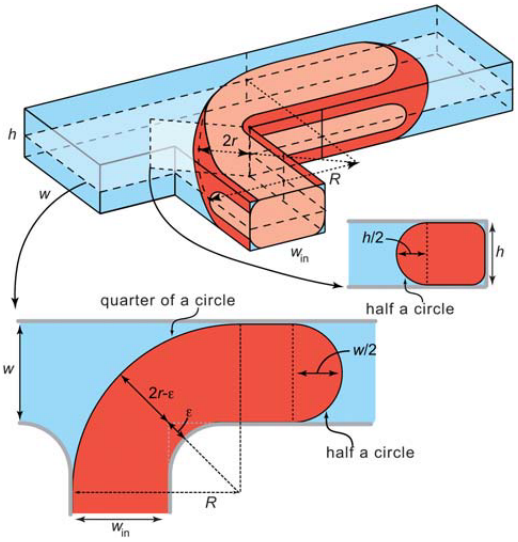

Figure 3.4: Geometrical reconstruction used to calculate the size of a bubble or droplet using two-dimensional views. The top-view image shown othe bottom left shows that the receding interface takes the shape of a quarter of a circle with radiu R, while the front of the droplet is described with half a circle with radius $w/2$. The roundend corners of the T-junction are characterized by the distance ϵ. Van Steijn *et al.* extended this "-D picture into the third dimension extrusion, taking into account the curvature of the interface shown on the bottom right. This curvature is again described as a half circle now with radius $h/2$ [104]. Note that in the T-junction used in our work ϵ can be neglected our corners were sharp and therefor the width of the neck is simply equal to $2r$.

The extrusion volume obtained is described as a funtion of the surface A and the perimeter l of the 2-D projection on the T-junction plane:

$$V = hA - 2\left(\frac{h}{2}\right)^2\left(1 - \frac{\pi}{4}\right)l. \tag{3.15}$$

As with the treatments of Garstecki and Christopher, Van Steijn divided the growth process of the droplet break-up in two stages: a *filling* stage where the emerging droplet increases in size until complete channel obstructions, followed by a *squeezing* stage consisting in the shrinking of the neck until pich-off (Fig. 3.2).

In the first stage the initial droplet volume V_{fill} is calculated simply by assuming that the droplet horizontal section can be rapresented by combining a quarter of a circle of radius R in the neck region and half of a circle of radius $w_c/2$ at the tip. In Fig. 3.5 two possible droplet sections are sketched depending on the geometrical ratio w_d/w_c. By geometrical considerations R_{fill} and V_{fill} are derived as follows:

$$R_{fill} = \max(w_d, w_c)$$

$$V_{fill} = \begin{cases} \dfrac{3\pi}{8} - \dfrac{\pi}{2}\left(1 - \dfrac{\pi}{4}\right)\dfrac{h}{w_c} & \text{for } w_d \leq w_c \\ \left[\dfrac{\pi}{4} - \dfrac{1}{2}\arcsin\left(1 - \dfrac{w_c}{w_d}\right)\right]\dfrac{w_d^2}{w_c^2} - \dfrac{1}{2}\left(\dfrac{w_d}{w_c} - 1\right)\sqrt{2\dfrac{w_d}{w_c} - 1} + \dfrac{\pi}{8} - \\ -\dfrac{1}{2}\left(1 - \dfrac{\pi}{4}\right)\left\{\left[\dfrac{\pi}{2} - \arcsin\left(1 - \dfrac{w_c}{w_d}\right)\right]\dfrac{w_d}{w_c} + \dfrac{\pi}{2}\right\}\dfrac{h}{w_c} & \text{for } w_d > w_c \end{cases} \tag{3.16}$$

After the filling stage the droplet grows at a rate determined by the inlet flow Q_d. This stage lasts for a time $\Delta t_{squeeze}$ during witch the neck width shrinks from the initial radius $2r$ down to the minimum radius $2r_{pinch}$ at which point break-up takes place. The same authors showed in a previous work that the thread connecting the froming droplet to the side inlet rapidly collapses as soon as the pressure inside the liquid upstream of the receding interface becomes smaller than the pressure inside the liquid downstream of the nose of the droplet [112]. The pressure difference over the forming droplet can be calculated usign the static Laplace pressure jumps at the rear and the front of the droplet. These pressure jumps over the interface prior to pinch-off are $p_d - p_{c_{\text{rear}}} = \sigma(1/R + 1/r)$ and $p_d - p_{c,\text{front}} = \sigma(2/h + 2/w_c)$ with the radii r and R defined in Fig. 3.4. Taking the pressure inside the droplet p_d uniform, the pressure difference

$$p_{c,\text{rear}} - p_{c,\text{front}} = \sigma(2/h + 2/w_c - 1/R - 1/r), \tag{3.17}$$

becomes negative once the radius r equals

$$r_{pinch} = \frac{hw_c}{2\left(h + w_c - \frac{hw_c}{R_{pinch}}\right)} \simeq \frac{hw_c}{h + w_c}, \tag{3.18}$$

where the curvature $1/R$ can be neglected with respect to $1/r$. Note that the expression for r_{pinch} is independent from the interfacial tension σ. The pinch off radius R_{pinch} can be obtained by reworking this criterion in terms of R using the relation between $2r$ and R (Fig. 3.4):

$$2r - \epsilon = R - \sqrt{(R - w_c)^2 + (R - w_d)^2}, \tag{3.19}$$

resulting in

$$R_{pinch} = w_c + w_d - \rho_{pinch} + \left[2\left(w_d - \rho_{pinch}\right)\left(w_c - \rho_{pinch}\right)\right]^{1/2} \tag{3.20}$$

and ρ_{pinch} is simply

$$\rho_{pinch} == r_{pinch} - \epsilon = \frac{hw_c}{h + w_c} - \epsilon \tag{3.21}$$

and ϵ again rapresents the curvature radius of the channel corners.

To determine the time interval $\Delta t_{squeeze}$ one has to consider that the droplet does not actually obstruct the main channel completely but leaves some spaces at the edges of the channel, called *gutters*, where the continuous phase can still flow. Therefore during the squeezing step there is an increase in the volume occupied by the continuous phase upstream of the droplet equal to

$$\frac{dV_c}{dt} = Q_c \left(1 - \frac{Q_{gutter}}{Q_c}\right) \tag{3.22}$$

where Q_{gutter} is the flow rate of the continuous phase going beyond the droplet through the gutters. At the same time the increase in the area occupied by the continuous phase projection in the in-plane section is $dA = 2(1 - \pi/4)RdR$ while its perimeter changes by $dl = \frac{\pi}{2}dR$, and using equation 3.15:

$$\frac{dV_c}{dt} = 2h\left(\frac{\pi}{4}\right)\left(R + \frac{\pi h}{8}\right)\frac{dR}{dt}. \tag{3.23}$$

Equating equation 3.22 and 3.23 and integrating from t_{fill} to t_{pinch} it is possible to find:

$$\begin{aligned}\Delta t_{squeeze} = \left(\frac{\pi}{4}\right)\left(1 - \frac{Q_{gutter}}{Q_c}\right)^{-1}\frac{hw_c^2}{Q_c}\cdot \\ \cdot\left[\left(\frac{R_{pinch}}{w_c}\right)^2 - \left(\frac{R_{fill}}{w_c}\right)^2 + \frac{\pi}{4}\frac{h}{w_c}\left(\frac{R_{pinch}}{w_c} - \frac{R_{fill}}{w_c}\right)\right].\end{aligned} \tag{3.24}$$

The volume gained by the droplets during the squeezing stage will be

$$V_{squeeze} = \Delta t_{squeeze} Q_d \tag{3.25}$$

and the final rescaled volume of the droplet is:

$$\bar{V} = \frac{V}{hw_c^2} = \frac{V_{fill}}{hw_c^2} + \frac{V_{squeeze}}{hw_c^2} = \bar{V}_{fill} + \alpha_V \frac{Q_d}{Q_c} \tag{3.26}$$

where:

$$\alpha_V = \left(\frac{\pi}{4}\right)\left(1 - \frac{Q_{gutter}}{Q_c}\right)^{-1}\left[\left(\frac{R_{pinch}}{w_c}\right)^2 - \left(\frac{R_{fill}}{w_c}\right)^2 + \frac{\pi}{4}\frac{h}{w_c}\left(\frac{R_{pinch}}{w_c} - \frac{R_{fill}}{w_c}\right)\right]. \tag{3.27}$$

Van Steijn *et al.* showed that this model predicted the linear dependence of the droplet volume on the flow rate ratio for the different T-junction aspect ratios treated in their paper ($w_d/w_c = 0.33, 0.67, 1, 1.33, 3$) but it did not account for the dependence of the droplet volume on Ca, a dependence verified by Christpher's experimental data.

While an exhaustive theory able to provide a scaling law for the droplet volume in the squeezing regime still lacks, we have established a basis for our analysis of our microfluidic droplet generator, identifying Ca, the droplet length and volume and the liquid fluxes as

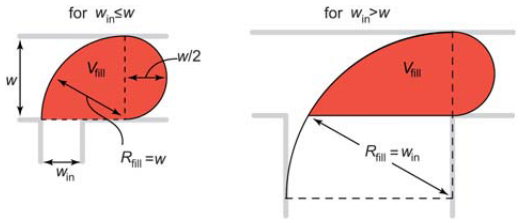

Figure 3.5: Shape of the droplet during the *filling* stage when $w_d \leq w_c$ (left) or $w_d > w_c$ (right) [104].

the prime parameters to obtain experimental trends in our microfluidic characterization. We will then proceed to compare our results to those obtained by the authors above, hopefully providing further information in the understanding of the T-junction geometry and describing the behaviour of the cross-junction geometry used in this work, a geometry which will prove to be a useful asset when attempting to use both the droplet generation and the waveguide illumination features of our microfluidic chip to perform a measure of the refractive index of different solutions.

3.5 Microfluidic Channels Fabrication in Lithium Niobate

As stressed at the beginning of the chapter we believe that lithium niobate is a valid alternative to other solid materials, such as silicon or glass, for the integration of multiple stages in a single device able to produce, manipulate, sort droplets and analyze their behaviour and contents.

Attempts to create microfluidic structures in silicon and glass are made easier by the a variety of fabrication techniques inherited from other fields of reaserch, such as chemical etching and mechanical micromachining on silicon derived from microelectronics [113, 114], exploited also for the realization of waveguides and ring-resonators for sensing optical stages; or the employment of femtosecond laser damaging inherited from optics, able to join waveguides and microchannels in the same glass substrate [115]. However, the only attempts found in literature to engrave microfluidics channels directly on lithium niobate were presented in last four years by Chauvet *et al.* at the University of France-Comté , Besanǫn (France) [116, 117] and by our group [12]. Many different micro-fabrication techniques have been used on lithium niobate in the past, especially in the in the field of optics for the realization of ridge waveguides or surface patterning for photonic crystals, wavelength conversion, Bragg reflectance or diffraction; but there aare very few studies reporting the realization of structures in the range of hundreds of micrometers in this material. Our group evaluated a series of fabrication techniques considering their advantages and drawback which will be briefly listed below:

- **Chemical Etching.** Chemical etching is widely used technique in $LiNbO_3$ microstructuring, specifically for the realization of ridge waveguides [44]. Lithium niobate has an extremely high chemical stability, thus a solution of hydrofluoric acid

(HF) is needed to etch its surface. Although this technique allows to obtain optical quality surfaces, the etching rate is very low ($\sim 1\mu$m/h at room temeprature) along the face perpendicular to the z-direction and even lower (a few nm/min) for the other surfaces, making it an exeedingly long process if one wants to obtain structures in the tens of micrometers such as those needed for our work. In addition the dependence of the etching rate on the surface crystallographic orientation makes it difficult to realize steep U-shaped channels on those surfaces where the etching rate is lower.

- **Reactive Ion Etching.** RIE has been successfully used to etch $LiNbO_3$ usign SF_6, CF_4 and CHF_3 plasmas at rattes up to 50nm/min and a $LiNbO_3$ selectivity of 0.25 [118]. Even better results were obtained by Inductive Coupled Plasma (ICP) with an etching rate of 190nm/min [119]. Several hours would be needed to engrave a 100μm deep channel but the quality of the surfaces would make this technique suitable in the attempt to create an integrated opto-microfluidic device in lithium niobate. Due to the unavailability of the needed instrumentation this technique was not studied in this work.

- **Focused Beam Litography.** FIB technique allows to obtain an optimal roughness of the channel walls (down to a few nanometers as recently reported by Sridhar *et al.* [120]). Nevertheless this technique seems to be more suitable for nanofluidics applications due to very low etching rates (around tens of nanometers depending on the beam current and accelerating voltage).

- **Laser Ablation.** This is a popular technique for the realization of optical waveguides and optical circuits [121, 122] but it also presents an alternative to etching and micromachining for the realization of microfluidic channels, since it allows to design almost any two-dimensional pattern on the sample surface and to finely control the depth of the engraved structures. Focused laser techniques are used on lighium niobate mainly for amorphisation or refractive index change to design waveguides and optical circuits, but it can be also used for the ablation of the material, making it a good candidate for the fabrication of microfluidics channels on lithium niobate since it provides a fast removal of the material and ensures an acceptable qaulity of the channel walls and flexibility in the circuit design.

- **Mechanical Micromachining.** Mechanical dicing and milling are common techniques to engrave micro-structures in silicon for opto-electronics, fast and easy to operate. Only in recent years this technique has been used on lithium niobate, probably due to its brittle nature, requiring a very accurate study of the process parameters to engrave while avoiding scratches and cracks. Moreover its pyroelectricity and its piezoelectricity can contribute to material stresses during the micromachining process. The only examples reported in literature are the employment of dicing saws which will be discussed in greater detail in section 3.5.1 as described in and a very recent study on lithium niobate micromilling where a CNC milling machine is

used to engrave cylindrical hole with a diameter of 500μm [123]. These recent development make this technique suitable to produce microfluidic channels with good surface quality (possibly better than those obtained by laser ablation). While the dicing saw used in this work poses severe limits on the device geometry, it proved to provide all the needed characteristics for the realization of a proof-of-concept set of microfluidic chips.

3.5.1 Mechanical Micromachining

The main advantage of mechanical micromachining in optical applications is the ability to provide generally good quality of the surfaces in the shortest fabrication time. Although this technique doen not allow for complicated structures to be engraved on lithium niobate, the straight forward process and reproducibility of the operation make it attractive when deep microfluidic channels have to be engraved.

In this work a DISCO DAD 321 precision saw was tested for micromachining of lithium niobate in collaboration with the university of France-Comté , Besanǫn (France). This polymeric blade with diamond particle has a diameter of 56mm and a thickness of 200μm. The parameters found to give the best surface quality were a rotating speed of 10000rpm and a cutting speed of 0.2mm/s. A constant flow of water was employed to keep the temperature low and to get rid of crystal residuals.

The obtained channels were characterized by optical microscopy and profilometry. As can be seen from microscope images the quality of the edges at the top of the channel is very high. A good quality of the top edge is imperative since it is on this edge that the in-diffused waveguides end and illuminate the channel and collect the diffused light on the other side. The morphology of both the lateral and bottom surfaces were investigated with a Veeco Cp-II atomic force microscope (AFM), which showed an average roughness of (19 ± 6)nm and (6.8 ± 0.5)nm for the bottom and lateral surfaces respectively. While this result is perfect for optical applications, the polymeric blade makes it impossible to obtain a T-junction since the curvature of the blade results in a decreasing depth in the last part of the channel ($\sim$ 2.4mm for a channel 100μm deep). We therefore adopted a natural geometry for this technique: a cross-junction with four branches. What would seem like a liability proved to be instead an asset, since this geometry can still be used in a T-junction configuration with comparable results, and enabled us to use two distinct dispersed phases at the same time with stable alternate droplet production.

3.6 Microfluidic Chip Sealing

In the previous section we have described the various techniques to engrave microfluidic channels on lithium niobate, but to complete a working microfluidic device these channels need to be sealed and inlets and outlets for the fluids have to be integrated. The first sealing method used by our group was the bonding of a layer of polydimethylsoloxane (PDMS) to the lithium crystal [124]. The sealing proved to be effective and resistant to

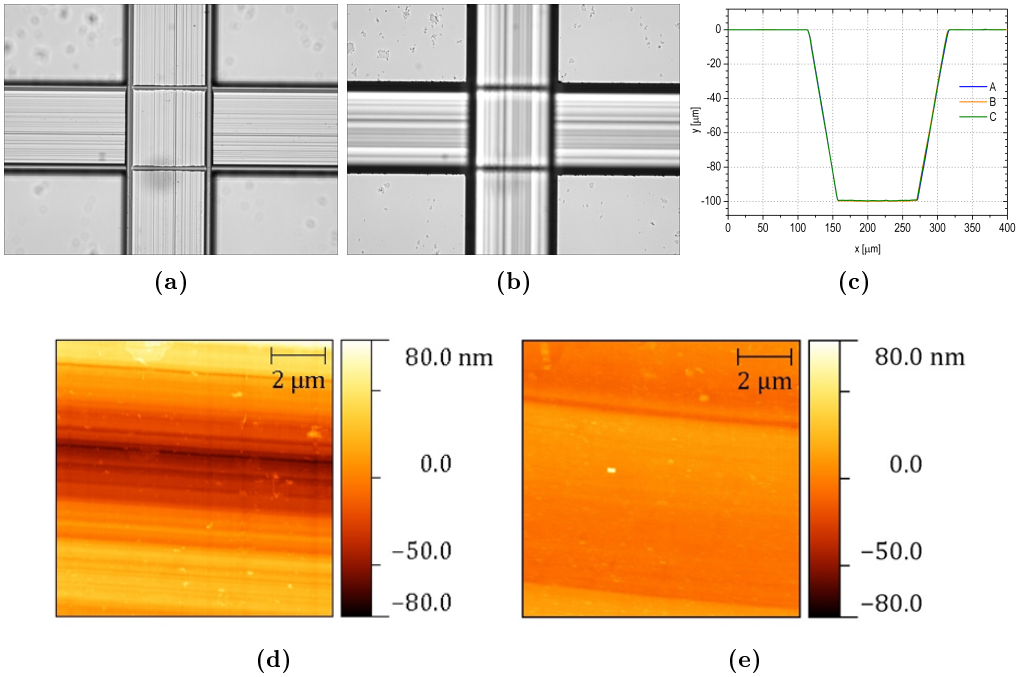

Figure 3.6: Characterization of the microfluidic channels engraved on $LiNbO_3$ with a dicing saw DISCO DAD 321. (a)(b) Microscope images focused on the bottom (a) and top (b) edges respectively of two crossing microfluidic channels; (c) superposition of three profiles collected at different positions along the two microfluidic channel showing the high reproducivility of the channel geometry (the sloped sides are an artefact due to the profilometer tip integration); (d)(e) $10\times10\mu m^2$ AFM images of the bottom and the side of the channel respectively with an average roughness of 19 ± 6nm and 6.8 ± 0.5

fluid rates up to 400μl/min before leaks started to appear, that means a pressure of about 2.4 atm in our microfluidic device. However it posed a few problems:

- the progressive degradation suffered by the polymer, which affects its transparency and elasticity after a few weeks;
- the swelling when using solvents and oils used in our microfluidic experiments;
- its poor resistance to chemical agents.

We therefore moved on to use a microscope silica slide to seal our microfluidic device. We tried two similar methods of glass sealing which we will discuss in the following.

Type L glass sealing

The first method consisted in cutting a microscope slide to fit the lithium niobate chip size and geometry. Four holes were drilled with a diamond coated drill head with a diameter of about 2mm in the same positions as the ends of the microfluidic channels. The area around the edges of this slide was then sandblasted (placing a mask over the slide

which left only the outer border exposed), creating a thinner region about 2mm wide all around. Four pieces of MASTERFLEX®silicone tubing were placed over the holes and glued to the glass slide using a small amount of PDMS. The slide was then placed in an oven at 70°C for about 2h for complete reticulation of the polymer. To glue the glass slide to the chip we chose the Norland Optical Adhesive 68 (NOA68) by Norland Products Incorporation, which is a very efficient adhesive employed to bound glass or plastic surfaces. It is a clear, colorless, liquid photopolymer which becomes a rigid solid after exposure to UV light at a wavelength between 350 and 380nm. It is resistant to acid solutions (tested by manifacturer in 10% $H_2SO_{4(aq)}$, 5% $H_2PO_{4(aq)}$, 5% CH_3COOH_{aq}) and to many organic solvents (hexane, toluene, methanol, trichloroethylene), and due to its rigidity doesn't suffer from swelling. We placed the lithium niobate chip in contact with the glass cover and clamped them togheter. This of course left a gap between the sandblasted area and the chip, which was then filled with small amounts of NOA. The chip was then placed under a UV lamp for 30min and then baked in an oven to help with solvent evaporation, after which the chip was ready for use. This technique ensures a high pressure resistance, at least as high as PDMS layer method. Nevertheless, the fact that the chip and the glass slide were simply clamped together meant that a small empty interspace a few micrometers wide was left over the channels. This posed no problems for the droplet production itself, but a small part of the continuous phase would always flow through the gap (meaning that the actual flux rate of the continuous phase at the junction was lower than one set at the inlet), and at higher flux rates ($Q_c \geq 50\mu$l/min and $Q_d/Q_c > 1$) even part of the dispersed phase started bypassing the junction through the interspace. For these reasons a microfluidic characterization of the chip is not comparable to the scaling laws described in section 3.4.1.

For applications requiring low fluxes however, such as biological applications, this type of low flux sealing is prefectly viable and has in fact been used during our opto-microfluidic tests with good results as described in chapter 5.

Type H glass sealing

A different type of glass sealing was tested which did not present any gap on the borders, to allow for higher flux rates to be used. The silica microscope slide was cut and drilled as before and the tubings were glued in the same way, but no sandblasting was performed. The lithium niobate chip and the glass cover were then clamped together and small amounts of NOA were placed on the lateral surfaces of the cover and the chip letting it seep in the small gap (a few micrometers) between the two thanks to capillarity, filling all available space, while surface tension prevented NOA from overflowing into the much wider microfluidic channels. This process took around 12h due to the NOA high viscosity and to the fact that just the right amount of NOA was employed to avoid overflowing into the channel. The chip was then placed under a UV lamp for 30min and then baked in an oven in the same way as in the previous glass sealing.

This technique still ensures a high pressure and chemical resistance, as well as solving

the interspace problem at high flux rates since the interspace was filled with NOA.

The last issue with the sealing techniques described so far is that the waveguide lies at the top of the channel, while in many applications it would be better to have the waveguide lying at the centre of the channel where it can illuminate the center of the droplets instead of their upper region.

To obtain this result, we investigated alternative geometries:

1. the top half of the channels could be engraved on the glass cover and the lower half on the lithium niobate chip (with the waveguides on its surface) and then the two could be glued together;

2. a layer of material could be created above the chip before the channels are engraved but after waveguides in-diffusion, and then engrave the channels directly on this "sandwich", which would then be sealed as normal.

The first method proved to be ineffective beacuse it would require perfect alignement of the cover with the chip, which is rather hard to achieve in practice.

The second method was tested with a 50μm layer of NOA over the lithium niobate chip, but unfortunately the NOA layer presented very rough and jagged lateral surfaces after dicing. Nevertheless, this seems to be the most promising method, but more tests will be needed to produce a reliable sealing with no loss in terms of surface quality, possibly with the use of different polymers or other materials.

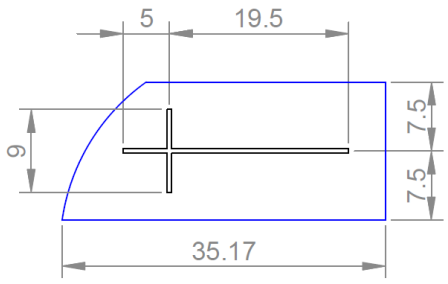

Figure 3.7: Scheme of a sample engraved with the dicing saw. Quotes are in millimeter. Curved edges are due to the round shape of the commercial wafer grown by Czochralski technique from which the samples were cut.

When considering a material for possible microfluidic applications one of its most importat properties is the wettability of its surfaces with respect to the fluids one wishes to employ. In the following we will study the wettability properties of lithium niobate, which will prove to be paramount for the generation of water droplets in oil.

3.7 Lithium Niobate Wettability

Wettability is the macroscopic effect of microscopic interactions between the surface and the molecules of the fluid and it usually depends on the chemical composition and the

physical morphology of the surface, as well as on the chemical and physical properties of the fluid such as surface tension and the polarization and polarizability of its molecules.

The standard procedure estimate the wettability of a material is to measure of the static contact angle θ_c, which is operatively defined as the angle between the solid surface and the liquid-air interface of a droplet of liquid deposited on said surface at equilibrium. According to Young's law [125] we can define the *wettability coefficient* $k = \cos\theta_c$, which depends on the interfacial tensions at the liquid-solid (σ_{ls}), liquid-gas (σ_{lg}) and solid-gas (σsg) interfaces:

$$k = \cos\theta_c = \frac{\sigma_{sg} - \sigma_{ls}}{\sigma_{lg}} \tag{3.28}$$

and rapresents an estimation of the wettability of the surface [126]. The higher the contact angle the lower is the wettability and vice versa.

In droplet microfluidics one desires surfaces easily wetted by the continuous phase, while the dispersed phase should have a very high contact angle and the droplets eveloped in the continuous phase should never come in contact with the channel walls. This is especially important during the droplet break-up process, which should depend only on the interaction between the two fluids and on the junction geometry and not on the wetting properties of the fluids with the solid surface. In addition, if the droplet is used as a carrier of any kind of chemical or biological sample, one generally wants to avoid any kind of interaction between said samples and the channel walls, to avoid possible absorbtion from the surfaces or their degradation degradation, or even possible contamination of the samples.

The first aim of this work was usign water as the dispersed phase for our droplets, since the analysis of biological samples is one of the future prospects for the kind of devices realized in this work, and these samples usully need to be disperse in water solutions.

The next step was then to choose a continuous phase fluid which is immiscible with water. The obvious candidates were found among oils: hydrocarbons such as decane,dodecanem hexadecane and mineral oil are frequently used in microfluidics, as well as silicone oils or even vegetable oils. These all have similar wettability properties since they interact mostly via Van der Waals forces, with possible differences caused by their polarizzability in the presence of strongly polarized surfaces. In our work we used two types of oil: hexadecane and light mineral oil. All the important coefficients and properties of hexadecane can be found in literature (and are given by the producer itself) with great precision, making it a very good candidate in microfluidics experiments. The only issuse we had with hexadecane (apart from the cost) is that it causes swelling in PDMS structures, which was a concern when we still used PDMS layers for chip sealing. We therefore started using mineral oil which still caused swelling but to a lesser degree. The introduction of glass sealing solved these problems altogether.

A detailed study of water and hexadecane wettability of lithium niobate was performed by our group and the results of the measurements are reported in Fig. 3.8. Hexadecane completely wets all surfaces of the crystal with a contact angle $< 10°$. Water has an average

wetting angle of $62° \pm 1°$ which indicates only a moderate hydrophobicity of lithium niobate. The discrepancies in wettability of different crystal cuts are not relevant for microfluidics applications and are compatible with different humidity or temperature conditions inside the laboratory.

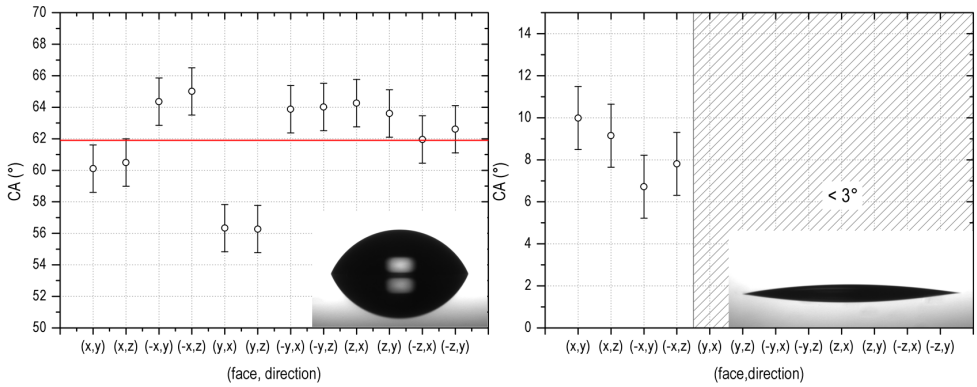

Figure 3.8: Contact angle (CA) measurements on a lithium niobate surface for different crystal cuts and different crystallographic directions for (a) water and (b) hexadecane. The red line represents the average of all CA determinations.

While the high oleophilicity of lithium niobate is a good starting point for microfluidics applications but a higher hydrophobicity is required for proper droplet production. Polymeric materials commonly used in microfluidics have a contact angle with water of around 100◦ to 120◦. Our premilimanry tests showed that with the lithium niobate chip as-is the only regime achievable is co-flow (Fig. 3.10).

Functionalization of the channel walls was found to be a valid solution to increase the contact angle of water with lithium niobate. Functionlization is a process that consists in coating a surface with a molecule which adheres to the surface and changes its wettability properties.

For the functionalization of the microfluidic channels, a solution of octadecyltrichlorosilane (OTS) in toluene or hexadecane was preperared at a concentration of 100μM. The solution was then injected in the microfluidic channels with a siringe pump at 10μl/min for about 15min, ensuring the fromation of a Self Assembled Monolayer (SAM) of OTA on the surface of the crystal. This procedure was usually done just after the sealing procedure, i.e. after exposure to UV light, which had the side effect of further cleaning the channel surfaces (thorough cleaning was carried out before each sealing) and to promote the formation of -OH ligands on the surface in order to better favour the condensation reaction needed for the bonding of the OTS molecules with the surface oxygen atoms [127, 128].

Contact angle measurements on functionalized lithium niobate crystals (Fig. 3.9) showed that both the contact angle of water and hexadecane were raised, with water reaching an average value of $(101 \pm 1)°$ and hexadacane raising to about $(35 \pm 1)°$. These values are comparable with those of PDMS found in literature $(100° \div 110°$ for water,

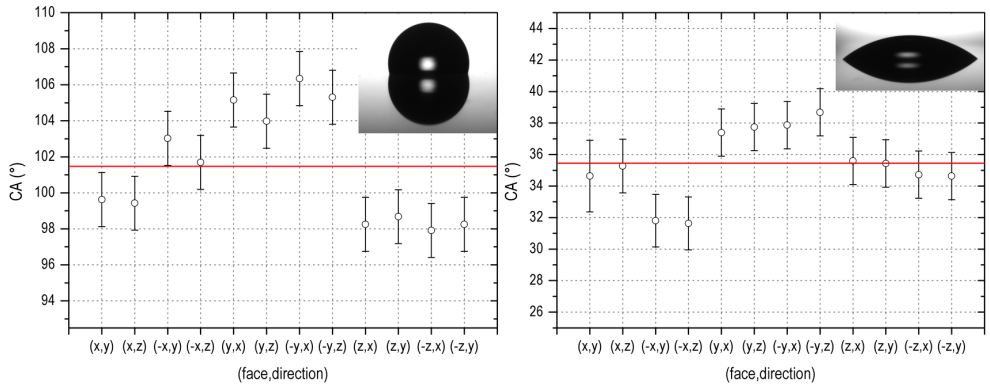

Figure 3.9: Contact angle (CA) measurements on a lithium niobate surface for different crystal cuts and different crystallographic directions after functionalization with a solution of OTS in toluene at a concentration of 100μm for (a) water and (b) hexadecane. The red line represents the average of all CA determinations.

$\sim 35°$ for hexadecane). This made droplet generation possible in our microfluidic chip (Fig. 3.10), even without the use of surfactants, molecules that naturally form micelle and are usually used in a solution with the continuous phase to improve droplet generation and reduce their volume dispersion.

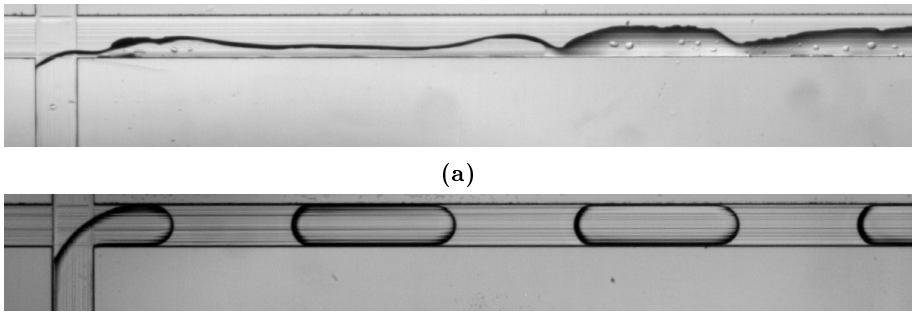

Figure 3.10: Effect of the functionalization on the droplet generation. Images show a cross junction (a) before and (b) after functionalization. Water is injected from the bottom inlet, while oil flows in the main channel (the top inlet was sealed). It is easy to see that no droplet generation can happen without changing the wetting properties of lithium niobate as water pins on the channel surfaces and simply coflows with the oil.

Chapter 4

Microfluidic Characterization

4.1 Experimental Set-up

The complete microfluidic setup used in these work consisted of two automated syringe pumps PHD 2000, Harvard Apparatu for the indipendent control of both the water and oil fluxes. The syringes were connected to the microfluidic chip through flexible polyethylene tubings by Deutsche & Neumann with an internal diameter of 0.5mm and an external diameter of 1.0mm resistant to acids, bases, alcohols and salt solutions up to 80°C. The tubing were connected to the syringes and the microfluidic chip through MASTERFLEX®silicone tubing by Cole-Parmer (OD = 4mm; ID = 0.8mm).

The plunger of the syringe is fixed to a clamp connected to a stepper motor, which pushes or pulls the plunger at a fixed speed. The flow rates range ranges from 0.0001μl/min (equal to the instrument sensibility) up to 220.82ml/min and the syringe pump can be used both to infuse and withdraw. In our experiment we used flow rates ranging from $Q_c = 5\mu$l/min to $Q_c = 60\mu$l/min for the continuous phase while the flow rates for the dispersed phase where kept inside a range of 0.1 to 1.5 times the flow rate of the continuous phase. We used mineral oil as the continuous phase and distilled water as the dispersed phase. Two sets of measurements were made, one with no added surfactants and one with surfactant (SPAN®80) added to the continuous phase. The surfactant concentration was set to 0.08% (w/w) which is above the critical micelle[1] concentration.

The experimental setup for the characterization cross-junction droplet generator included, in addition to the microfluidic setup, a fast camera connected to a microscope able to record image sequences of the droplet production and flow throughout the channel (Fig. 4.1). The microscope employed in the experiment was an inverted microscope Eclipse Ti-E, Nikon with a plan 4x/0.10 objective with a 30mm working distance. A fast camera Phantom VRI v7.3 was used to record the image sequences. The resolution of the images

[1] a micelle is an aggregate of surfactant molecules (long molecules hydrophilic at one end and hydrophobic at the other) dispersed in a liquid. When the surfactant concentration is above the critical micelle concentration the monomers self-organize forming encolsed vescicules. In the presence of two liquids (e.g. water in oil) the surfactant molecules arrange themselves at the fluids interface, reducing the surface tension.

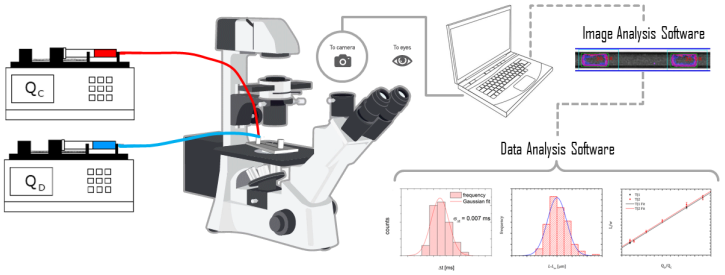

Figure 4.1: Sketch of the experimental setup employed for the measurement and the analysis of the droplet length and production frequency.

was set to 1280×254, which were calibrated to determine the spacial resolution of the image which was found to be 3.46μm/px. The exposure time of a single frame was kept fixed (200μs or 100μs for the higher flux rates, enough to avoid motion blur) as well as the illumination of the samples, while the frame rates were changed based on the droplet velocity in order to have about the same number of frames for every droplet (a single droplet appeared in about 9-11 frames before it left the field of view).

The analysis of the images was performed with the aid of custom made software developed by Enrico Chiarello, in the framework of the LaFSI group at the Department of Physics of the University of Padova.

The imaging software is based on the analysis of the contrast of the images which allows for the recognition of the droplet interface with respect to the channel floor. The program can then follow the droplets frame by frame, calculating their length, speed and flowing time. The length of a droplet is determined from each single frame while the speed and the time when it crosses the center of the field of view are derived by fitting its position at each frame as a function of the frame number.

The output of the software gives for each droplet its length measured in pixels, its speed in pixels/frame and the time of its passage through the center of the image in frame number. These data were then elaborated usign a data analysis software developed by Giacomo Bettella, a member of the $LiNbO_3$ group at the Department of Physics of the University of Padova.

4.2 Droplet Generator Performances

The characterization of our droplet generator is fundamental to asses its efficiency and versatility. It should be able to produce droplets over a wide range of volumes and frequencies and have a very sharp distribution both in the droplet volume and in the time interval between subsequent droplets. The volume monodispersion in particular is critically important for the precise control of dispersed analyte quantities or reagents dilution. In a passive device such as ours this is directly linked to the production frequency distribution when the flow rate is fixed (as it was in all our measurements), which shall then have a very sharp distribution as well.

For this characterization we used a cross-junction with a type H sealing (described in section 3.6), employed in a T-junction configuration obtained by filling the extra inlet with mineral oil (the same used as the continuous phase in the experiments) and then sealing the silicon tubing. This ensured that there was no in- or out-flux from said inlet, with the result of a droplet generation very much like that obtained in a standard T-junction geometry.

To test the performances of this configuration we proceded to record several image sequences of more than 100 droplet each with a capillarity number ranging from $6.4 \cdot 10^{-4}$ to $2.55 \cdot 10^{-3}$ and different different flow rates $\phi = Q_d/Q_c$ from 0.1 to 1.85. From these sequences we obtained the length and frequency distribution of the droplets.

Droplet frequency: the droplet frequency f depends on the flow rates of the continuous and dispersed phase and is limited only by the maximum flow rates the channel is able to sustain. A T-junction in lithium niobate closed with a PDMS layer was tested at flow rates of up to $Q_c = 300\mu$l/min and $Q_d = 80\mu$l/min with a corresponding $f_{max} = 1157 \pm 9$Hz. With the most recent glass sealing the maximum frequency obtainable is probably higher but the chip was only tested up to $Q_c = 50\mu$l/min and $Q_d = 87.5\mu$l/min with a frequency of 450Hz which was enough for a characterization at low Ca (to confront the results with Christopher's scaling law). The droplet production frequency was calculated by the average of the distribution of the time interval between two subsequent droplets, at a fixed flow rate ratio $\phi = Q_d/Q_c$. Only distinct droplet pairs have been taken into consideration (for example we considered the time interval between the first and second droplet, the third and the forth, but not between the second and the third) so that $\Delta t_j = t_{2j+1} - t_{2j}$ with $j = 1, 2, 3, ..., N/2$ with N the total number of droplets in the sequence. This was done to avoid possible asymmetries in the time distribution and possible correlations. The observed time interval distribution did not show large deviations from the Gaussian for all tested frequencies (between 35Hz and 450Hz) with a maximum standard deviation of 13% and an average standard deviation of 4.7%.

Droplet length: the length of the droplet L was measured in pixels as the distance between the two menisci of the droplet, which was then converted in micrometers according to the calibration obtained from a standard calibration sample. The length distributions at fixed ϕ ere found to have a maximum standard deviation just above 5% and an average standard deviation (considering all length distributions obtained at different ϕ) of 1.6%, in line with microfluidic standards.

4.2.1 Error contributions to droplet length and frequency determination

The two main sources of error in the determination of the droplet length and frequency are the image quality and and the pumping system.

The image quality is determined by the size of the camera pixels, which in our case was $r_{px} = 3.46\mu$m. In addition, the image resolution makes it so that the droplet boundary

shown in the image spans over more than one pixel, with an uncertainty σ_{px} related to the image resolution. In order to estimate σ_{px} we considered the pixel length as the maximum uncertainty relative to the boundary location. By assuming a uniform probability density distribution, σ_{px} can be estimated as $\sigma_{px} = r_{px}/\sqrt{12} = 1.00\mu$m. The uncertainty on the measurement of the droplet length is therefore $\sigma_{L,px} = \sigma_{px}\sqrt{2} = 1.41\mu$m, derived from the error propagation law applied to the difference between the positions of the advancing and the receding menisci.

This source of error is however negligible in the determination of the time interval between two consecutive droplets, because the time of passage of a droplet at the center of the image is calculated as the intercept of the linear fir of 10 or more posistions of the advancing meniscus as a function of time.

The source of error introduced by the pumping system is more difficult to be determined. The syringe pumps employed to inject the fluids inside the microfluidic channel have a high control on the injected flow rate (accuracy within 0.35% and reproducibility within 0.05% declared by the manufacturer). The syringes used to pump the fluids however could have an irregular diameter along their length and the tubing connecting the syringes to the microfluidic chip inlets can suffer from small elastic or plastic deformations under the imposed pressures, up to about 1bar, for prolonged periods of time.

This can add systematic errors to the measured length of the droplets and their production frequency. Sometimes this errors can be avoided by waiting enough time for the system to stabilize, but since this waiting time is hardly a known quantity these sources of error have to be taken into account.

Our group performed a few measurements to estimate these error contribution, by fixing the flow rates of both phases and collecting three image sequences of 2000÷3000 droplets at three distinct times: 1 minute after setting the injection fluxex and again after 15 and 30 minutes. The results of these measurements of the time intervals plotted as a function of the droplet number are reported in Fig. 4.2. While the amplitude of the high frequency fluctuations decreases significantly after 15 minutes of constant flow, the main contribution to the deviation from the mean, which comes from the low frequency fluction, does not seem to decrease as time passes. Therefore, we chose to wait 15 minutes every time the fluxes were changed to avoid the high frequency fluctuations, while the low frequency fluctuations were taken as a random source of error in the determination of the average Δt in a 100÷200 droplets image sequence (since the time period of the low frequency fluctuations is much longer than the image sequence time duration).

The low frequency fluctuations were approximated as a sinusoidal with a probability density distribution of the measured time interval taking the form:

$$p(\Delta t) = \begin{cases} \dfrac{1}{\pi}\dfrac{1}{\sqrt{A^2 - (\Delta t - \bar{\Delta} t)^2}} & \forall \Delta t \in \left]\bar{\Delta} t - A, \bar{\Delta} t + A\right[; \\ 0 & \text{elsewhere;} \end{cases} \tag{4.1}$$

where $\bar{\Delta} t$ is the mean value and A is the sinusoidal amplitude. An estimation of the

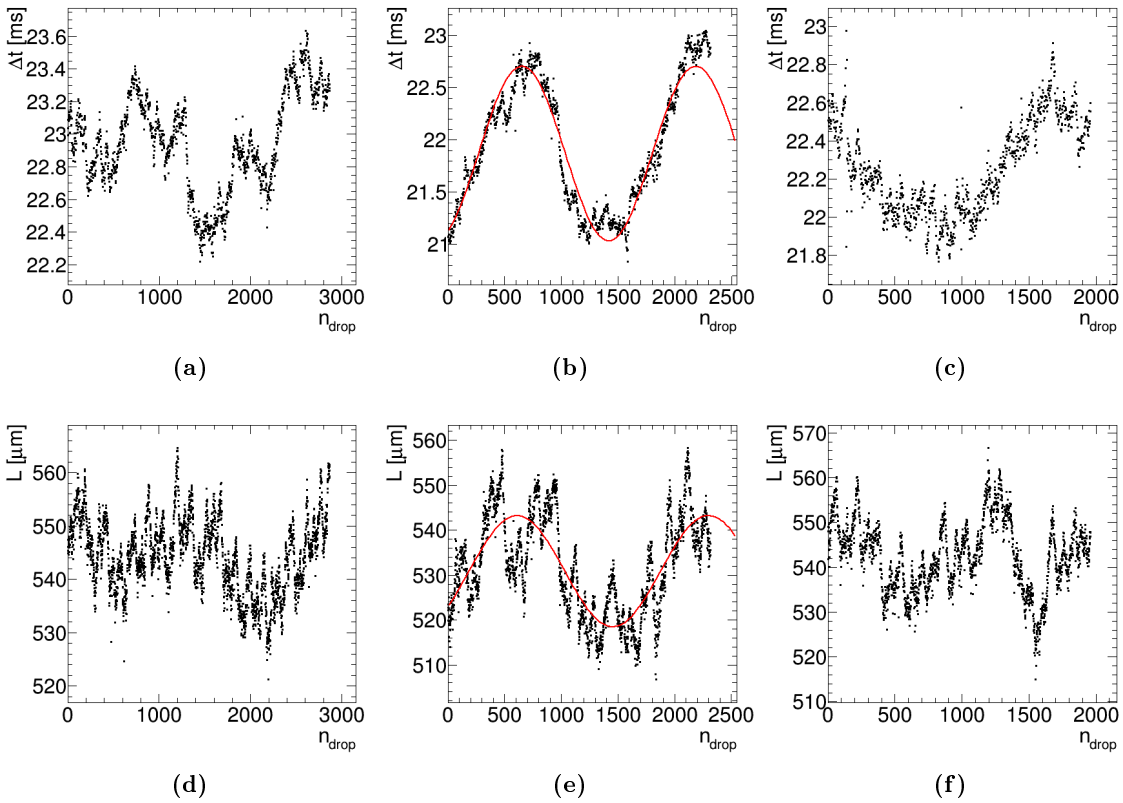

Figure 4.2: Contributions to the dispersion of both the droplet frequency and the droplet length due to the fluctuations of the pumping system. In (a), (b) and (c) measurements of the time interval between two subsequent droplets are shown as a function of the droplet number n_{drop}. (d), (e) and (f) show the droplet length measurements taken during the same experiment. All plots refer to flow rates $Q_c = 10\mu$l/min and $Q_d = 10\mu$l/min; (a),(d) were measured after 1 minute since the fluxes were set; (b), (e) after a 15min wait and (c), (f) after a 30min wait. The red curves represent the sinusoidal fit of the measurements taken after 30min.

dispersion of Δt can be obtained as the square root of the second moment of the distribution $p(\Delta t)$:

$$\sigma_{\Delta t,\text{pump}} = \left[\int_{-\infty}^{+\infty} d(\Delta t)p(\Delta t)(\Delta t - \bar{\Delta t})^2\right]^{1/2} = \frac{A}{\sqrt{2}}. \tag{4.2}$$

The amplitude of the sinusoidal oscillation was calculated for each tested couple of flow rates after 15min wait by fitting the measured Δt as a function of the droplet number and it was verified to be of the same order for all tested fluxes. The dispersion $\sigma_{\Delta t,\text{pump}}$ was calculated for all long time recording tests taken after 15min wait with a maximum $\sigma^{\max}_{\Delta t,\text{pump}} = 0.59ms$, which was chosen as the estimation of the random error caused by the pumping system.

The same procedure was followed for the estimation of the random error on the average length. In this case the low frequency fluctuations were of lower amplitude compared to the high frequency fluctuations. The random error was estimated to be $\sigma^{\max}_{,\text{pump}} = 8.73\mu$m.

4.3 Comparison with Microfluidic Scaling Laws

The comparison of the experimental results for the droplet generation with those found in literature and with the theoretical scaling laws is useful to understand if our cross junction behaves in the same way as a T-junction when used in the same configuration, i.e. with one of the inlet channels sealed, and provides a tool to predict the response of the droplet generation as a funtion of the external variables controlled by the user, i.e. the liquids used and their inlet fluxes.

First of all one has to identify which droplets generation regime would be best for the chosen application and the corrisponding parameters range. The production regime can be deduced in two ways:

- by simply looking at the droplet while it is generated: as described in section 3.3 the main difference between the squeezing and dripping regime is whether the droplet blocks the whole channel before the break-up or not. In the squeezing regime the produced droplets are longer than the main channel width ($L > w_c$) and fill the channel entirely. Conversely in the dripping regime the droplets have a mean radius smaller than the main channel width;

- by studying the dependence between the droplet volume and the capillary number: the squeezing regime is typical of low capillary numbers while the dripping regime is found for Ca>Ca* = 0.015, with Ca* the critical capillary number found by De Menech *et al.* [109] which marks the change in the relation between Ca and the droplet volume. The value of Ca and the trend of V as Ca varies can therefore be used to identify the droplet production regime.

As stated before the aim of this work is the coupling of a channel waveguide to the microfluidic channel to illuminate the droplets and collect the transmitted light. The

squeezing regime is then preferred, with plugs occupying the largest portion of the channel cross-section as possible. Therefore our microfluidic analysis was performed for capillary numbers below the critical value (Ca<0.015), and the employed fluxes were divided in a set of samples with Q_c = 15, 20, 30, 40, 50μ/min and Q_d = (0.1, 0.25, 0.4, 0.55, 0.7, 0.85, 1.0, 1.15, 1,3, 1.45, 1,6, 1.75)·Q_c, and a smaller set of samples with Q_c = 12.5, 17.5, 25, 35, 45μ/min and Q_d = (0.1, 0.4, 0.7, 1.0, 1,3, 1,6)·Q_c. The first set of fluxes was chosen to have a large enough number of points to verify the expected linear relation between the length of the droplets L and the flux rate ratio ϕ, while the smaller set was used in combination with the first one to verify Christopher's scaling laws $\bar{f} = \frac{\mu_c w_c}{\sigma} f = \bar{\beta} \cdot \mathrm{Ca}^{1-\delta}$ and $\bar{V} = \frac{V}{w_c^2 h} = (\phi/\bar{\beta}) \cdot \mathrm{Ca}^{\delta}$, with $\bar{\beta}$ kept as a fitting parameter. For the sake of simplicity we used the logarithm of these scaling laws to obtain linear relations, i.e $\log(\bar{f}) = \log(\bar{\beta}) + (1-\delta) log(\mathrm{Ca})$ and $log(\bar{V}) = log(\phi/\bar{\beta}) + \delta \log(\mathrm{Ca})$, to more easily compare these laws with our experimental trends.

4.3.1 Analysis of the Droplet Production Frequency

The rescaled droplet production frequency $\bar{f} = \frac{\mu_c w_c}{\sigma} f$ was analyzed for fixed values of $\phi = Q_d/Q_d = \{0.1, 0.4, 0.7, 1.0, 1.3, 1.6\}$ as a function of Ca (for values of $6.4 \cdot 10^{-4} < \mathrm{Ca} < 2.55 \cdot 10^{-3}$). The results are plotted in Fig. 4.3. As observed experimentally by Christopher *et al.* [110] a linear dependence of $\log(\bar{f})$ on log(Ca was found (see eq. 3.13). While some points suffered from a higher dispersion, especially at the lowest ϕ tested, they did not present large deviations from linearity.

4.3.2 Analysis of the Droplet Length

The most common scaling law found in literature when describing the T-junction is the linear dependence of the droplet length (or volume) on the flow rates $\phi = Q_d/Q_c$. Plots of the averaged rescaled droplets $\bar{L} = L/w_c$ as a function of the flow rate ratio ϕ, measured at different values of the continuous phase flow rate Q_c. The plots are reported in Fig. 4.4; the measurements follow a linear relation between $\bar{L}$ and ϕ as expected with no large deviations from this trend exept for the points at the higher flow rates. Still, the results are very satisfying and in line or better than similar plots found in literature.

It was also verified that the droplet rescaled volume $\bar{V} = V/w_c^2 h$, calculated from the droplet length following the expression proposed by Van Steijn *et al.* [104] (Eq. 3.15), shows a dependence on the capillary number Ca as observed by Christopher *et al.* (who proposed a scaling law reported in section 3.4.1 , Eq. 3.14). We linearized the dependence between the droplet rescaled volume and the flux rate ratio to obtain a more easily verified relation. Plots of the rescaled droplet volumes $\bar{V}$ as a function of the capillary number Ca for fixed values of the flow rate ratio ϕ are reported in Fig. 4.5. The linearity is again satisfied exept for the higher flux rates, in line with Christopher's observations.

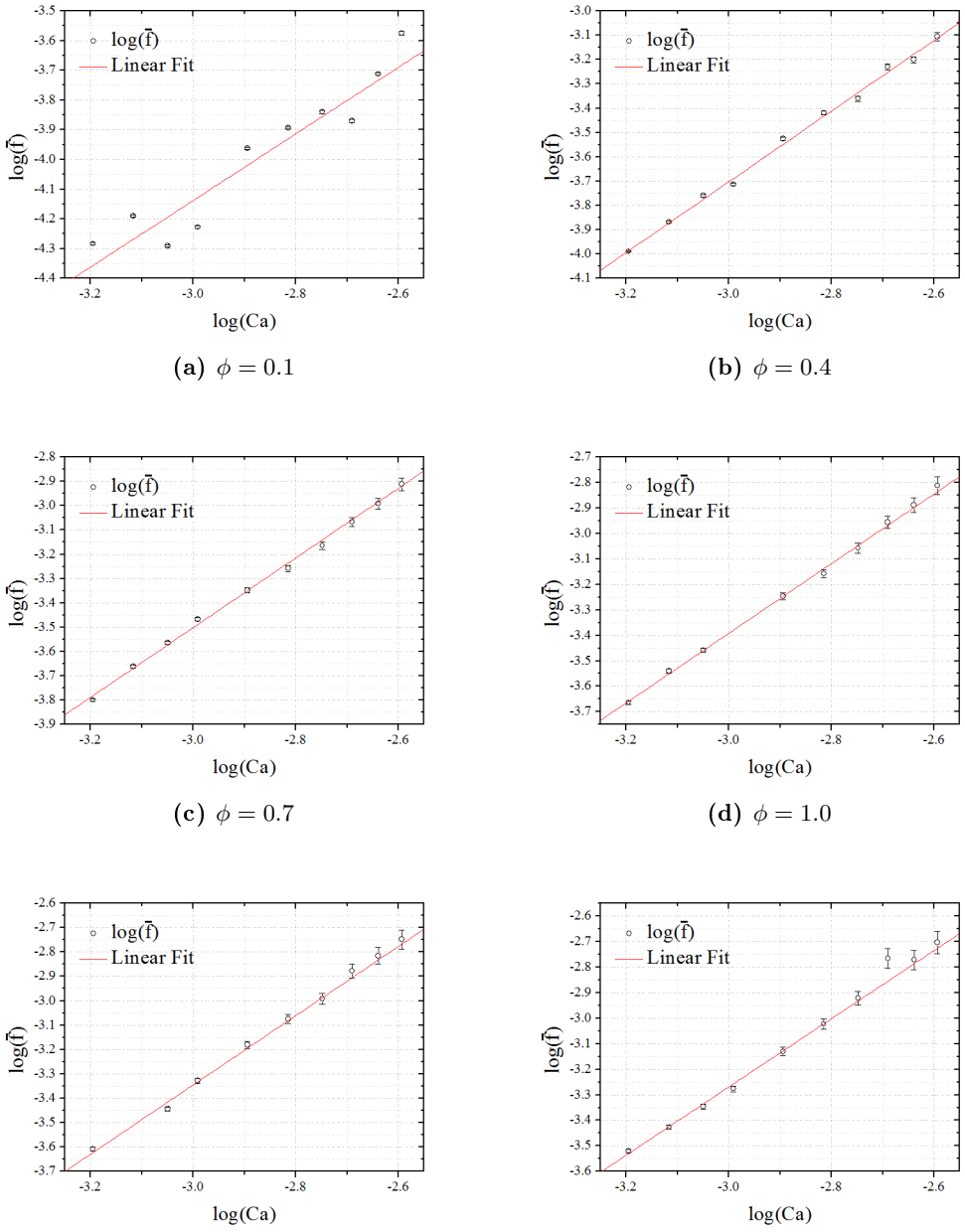

(a) $\phi = 0.1$ **(b)** $\phi = 0.4$

(c) $\phi = 0.7$ **(d)** $\phi = 1.0$

(e) $\phi = 1.3$ **(f)** $\phi = 1.6$

Figure 4.3: Analysis of the rescaled droplet production frequency $\bar{f} = \frac{\mu_c w_c}{\sigma} f$ as a function of the capillary number Ca at fixed flow rate ratios ϕ, with mineral oil as the continuous phase (no surfactant added, $\sigma = 40\text{mN/m}$). The red line represents the linear fit of the experimental data.

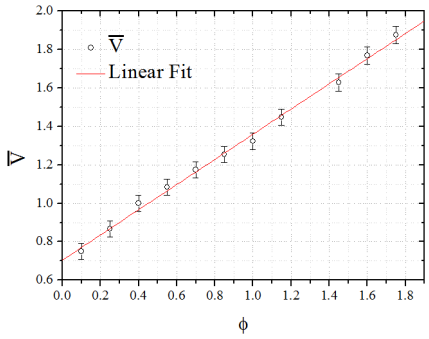

(a) $Q_c = 15$

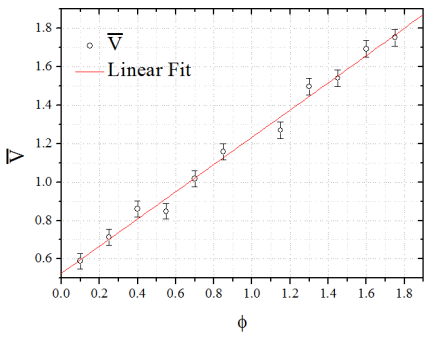

(b) $Q_c = 20$

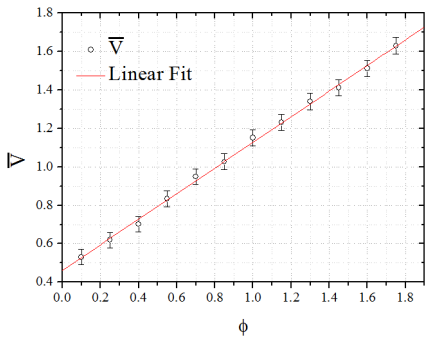

(c) $Q_c = 30$

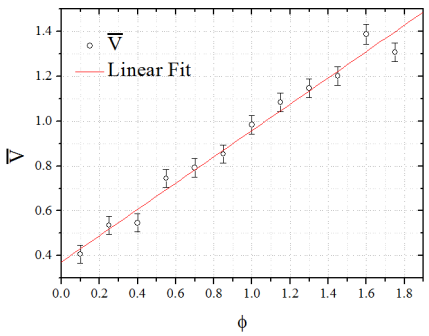

(d) $Q_c = 40$

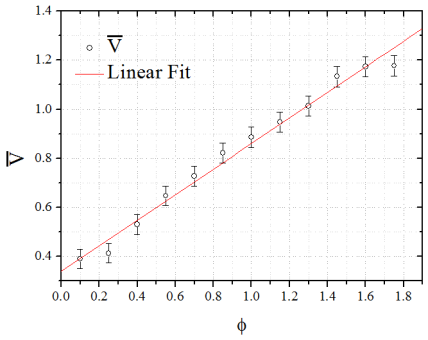

(e) $Q_c = 50$

Figure 4.4: Analysis of the rescaled droplet lengths $\bar{L} = L/w_c$ as a function of the flow rate ratio ϕ at fixed continuous phase flow rates Q_c, with mineral oil as the continuous phase (no surfactant added, $\sigma = 40\text{mN/m}$). The red line represents the linear fit of the experimental data.

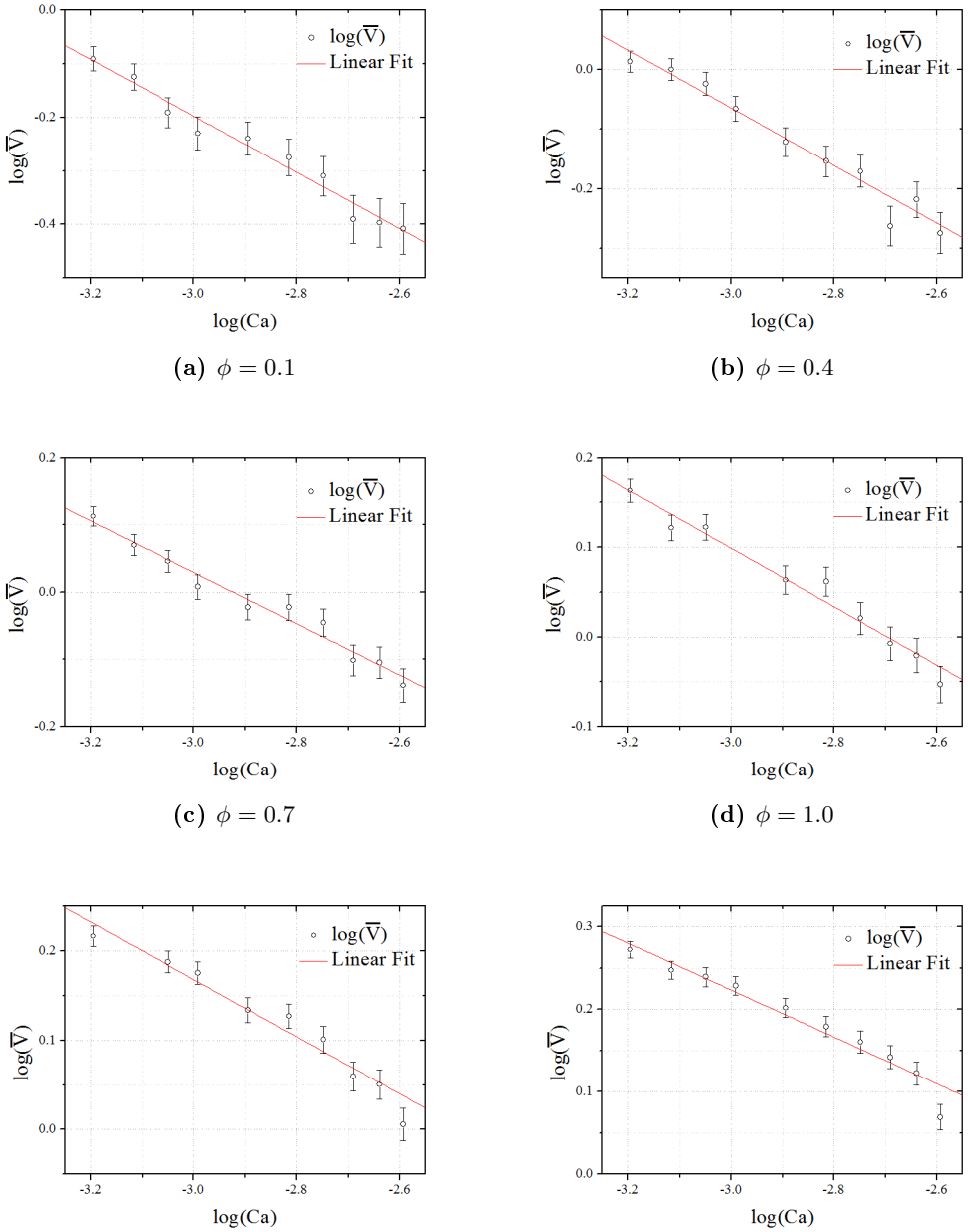

(a) $\phi = 0.1$ **(b)** $\phi = 0.4$

(c) $\phi = 0.7$ **(d)** $\phi = 1.0$

(e) $\phi = 1.3$ **(f)** $\phi = 1.6$

Figure 4.5: Analysis of the rescaled droplet volume $\bar{V} = V/w_c^2 h$ as a function of the capillary number Ca at fixed flow rate ratios ϕ, with mineral oil as the continuous phase (no surfactant added, $\sigma = 40\text{mN/m}$). The red line represents the linear fit of the experimental data.

4.3.3 Fit Parameters for $\bar{f}$(Ca) and $\bar{V}$(Ca)

It is worth noting that the scaling laws proposed by Christopher for the rescaled frequency $\bar{f}(\mathrm{Ca})$ and the rescaled volume $\bar{V}(\mathrm{Ca})$, which we report in their logarithmic form:

$$\log_{10}(\bar{f}) = \log_{10}(\bar{\beta}) + (1-\delta)\log_{10}(\mathrm{Ca}), \tag{4.3}$$

$$\log_{10}(\bar{V}) = \log_{10}\left(\frac{\phi}{\bar{\beta}}\right) + \delta\log_{10}(\mathrm{Ca}), \tag{4.4}$$

share the same parameters $\bar{\beta}$ and δ, since the second one derives from the first from the alterante definition of the rescaled frequency given by Christopher $\bar{f} = \frac{\mathrm{Ca}\times\phi}{\bar{V}}$. We calculated $\bar{\beta}$ and δ as fitting parameters for the linear fits showed in Fig. 4.3 and 4.5, as well as for the other available measurements of $\bar{f}$ and $\bar{V}$ for values of $\phi = (0.25, 0.55, 0.85, 1.15, 1.45, 1.75)$, constituted by only six fitted points each. The parameters are presented in Fig. 4.6a,b, with the black points being the fitting parameters of $\bar{f}(Ca)$ and the red point being the fitting parameters of $\bar{V}(Ca)$, to confront the values obtained from the rescaled frequency and the rescaled volume.

For δ (Fig. 4.6b), we see that in most cases the black and red points at a fixed ϕ are compatible, apart from the points at $\phi = (0.1, 0.55)$ where the error bars are too large to conduct a compatibility test. Since half of the points presented were calculated from linear fits from a lower number of points (six instead of twelve) we removed those points and present the remaining ones in Fig. 4.6d. This second plot can be roughly divided into two regions, one for $\phi \geq 0.7$ where the trend is approximately constant, in line with Christopher's observations, and one for $\phi < 0.7$ where no definite trend can be discerned (arguably a third region could be identified for $\phi > 1.6$ but more measurements would be needed in this region to make any kind of remark). In the first region, we note that the black points (related to the frequency) are underestimated with respect to the red points (related to the volume) leading us to believe that there could be a systematic error in the formula relating the droplet length to its volume. We suggest this simply because the results for the frequency, as stated before, are less subject to systematic errors in their measurements. We also note that the average values for $\delta_{av}^{\bar{f}}$ and $\delta_{av}^{\bar{V}}$ are not compatible, suggesting again the possibility of a systematic error. In the plot we show also the value of δ obtained by Christopher *et al.*, which they found to be constant in this range.

For $\bar{\beta}$ the average values found for both $\bar{f}(Ca)$ (black points) and $\bar{V}(Ca)$ (red points) shown in Fig. 4.6a,c appear to be compatible only in the region $0.7 \leq \phi \leq 1.6$, with the points outside this region having error bars too large for a reliable compatibility test. In this center region (Fig. 4.6c) the values show no definite trend; we calculated and plotted the average values for $\bar{\beta}_{av}^{\bar{f}}$ and $\bar{\beta}_{av}^{\bar{V}}$ in this range and found them to be compatible with each other. Christopher *et al.* report a linear dependence of of $\bar{\beta}$ on the flux rate ratio ϕ [110], but this would mean that the first term on the right hand side of Eq. 4.4 does not depend on ϕ, i.e. that the rescaled volume is independent from ϕ. This is not the case as

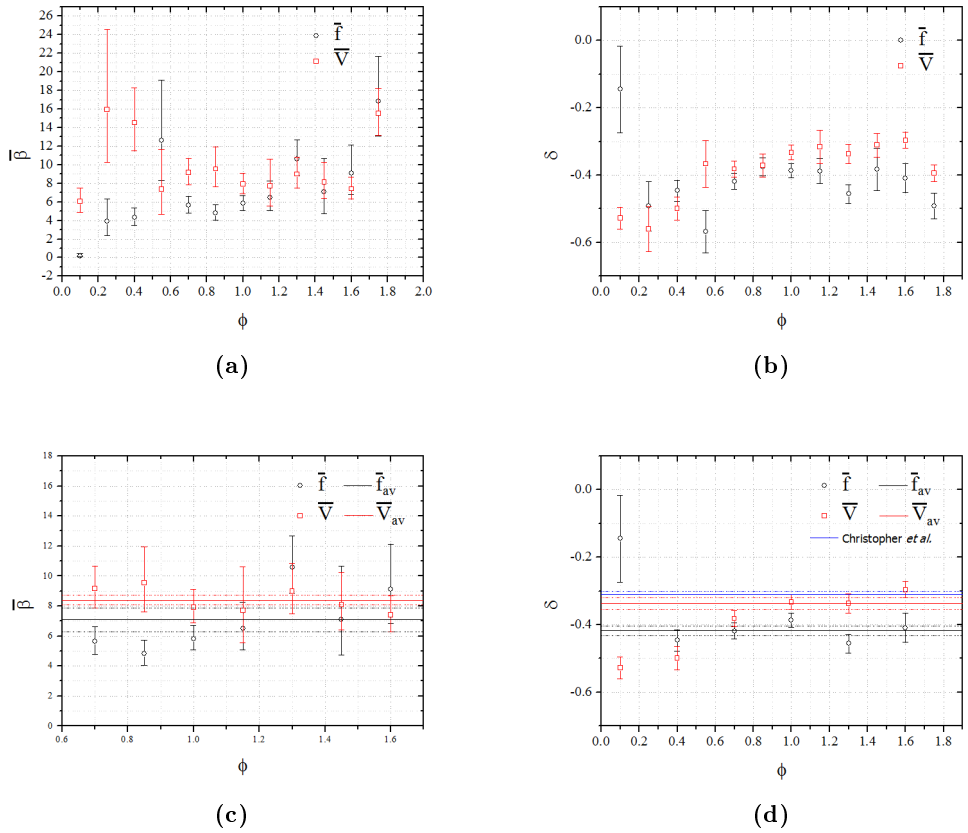

Figure 4.6: Analysis of the parameters (a) $\bar{\beta}$ and (b) δ obtained from the linear fits for $\bar{f}$(Ca) and $\bar{V}$(Ca).

shown previously in Fig. 4.4 for the droplet length (from which the volume is derived) and by Christopher *et al.* themselves in the same paper [110].

The other scaling laws for the volume proposed by Garstecki *et al.* [102] and by Van Steijn *et al.* [104] which were reported in Eqs. 3.5 and 3.26

Chapter 5

Optofluidic Coupling

In this chapter we describe our opto-microfluidic chip, built integrating the in-diffused channel waveguides described in chapter 2 and the microfluidic cross-junction droplet generator described in chapter 3. We will then describe two applications meant as proof-of-concept demonstrations of the capabilities of the device:

- a droplet counter, which reveals the droplet passage by measuring the effect on the light transmission across the channel. The illumination and signal collection are done via two waveguides crossing the channel at a right angle, as shown in Fig. 5.6;
- a droplet sensor, which works by monitoring the device response when droplets containing different solutions flow through the channel. We will study the correlation between the intensity of the output signal and the refractive index and solute concentration in a series of $CaCl_2$ solutions;

We will then briefly talk about the future prospects of this type of device, some of which are currently being studied by our group.

5.1 Opto-Microfluidic Chip Realization and Preliminary Tests

The procedure for the production of the opto-microfluidic is simply an application of the various techniques described in the previous chapters:

- Titanium in-diffused waveguides are produced on lithium niobate samples obtained from a x-cut $LiNbO_3$ commercial wafer as described in section 2.3;
- the waveguides on every sample are tested with the near field setup described in section 2.5. This gives us information on every waveguide general performances, the number of modes, the shape of the modes and the relative output intensity of the waveguide by means of the intensity profiles obtained from near field CCD images;
- microfluidic channels are then engraved on the sample by mechanical micromachining as described in section 3.5.1: the cross-junction is engraved in such a way as to

have the main channel cross the waveguides at a right angle. This ensures that the waveguides at both sides of the channel are aligned, making it possible to illuminate the channel from one side and collect the light from the other;

- the waveguides on each sample are tested again (now with the channel crossing them) to see which are still functional and to check for their inevitable loss in performance, both in air and by filling the channel with hexadecane ($n_{hexa} = 1.434$ at $\lambda = 632.8$nm). The hexadecane drop filled the channel by capillarity and allowed for better index matching with the lithium niobate crystal compared to air;

- after assesing the performances of the optical stage of the device, the is sealed and functionalized following the procedures described in sections 3.6 and 3.7;

- finally the microfluidic performances of the droplet generator are tested to check the sealing for leaks and to test the proper functionalization of the channels.

The key parameter to be studied in this opto-microfluidic system is the light transmitted across the microfluidic channel, as this is meant as the main tool to investigate and analyze various properties of the droplets flowing inside it. It was experimentally verified that, barring those cases where the dicing process produced defects on the channel edge were the waveguide was localized, the coupling of a laser with the waveguides still results in well defined images with no systematic change in the shape of the single mode after the waveguide is interrupted by the microfluidic channel.

5.2 Preliminary Tests

In the case of the open channel in air, the single mode of the output waveguide was recognizable at the near field image collected at the surface of the crystal. An example of the near-field image of a z-propagating waveguide crossed by the microfluidic channel is shown in Fig. 5.1b. The collected intensity is the 38% of the intensity recorded before the channel was engraved. Due to diffraction this intensity is lower than the 74% intensity expected by simply considering the Fresnel transmission coefficients across the two interfaces $LiNbO_3$-air, air-$LiNbO_3$. Nevetheless diffraction can enhance the sensitivity of the waveguide to the refractive index change of the fluid filling the channel: as can be seen by the near field image recorded in the presence of hexadecane inside the microfluidic channel (Fig. 5.1c), the transmitted intensity raises up to 2 times compared to the image taken in air, while the transmission of a non-diffracting plane wave should increase only by a factor 1.2.

These preliminary tests show that the optical stage of our device is indeed suitable for optofluidic applications as it is sensitive to some extent to the fluids flowing through the channel and the signal loss in the output is perfectly acceptable considering that the channel is 200μm wide, much larger than the waveguide dimensions.

These first tests were made on chips sealed using a type L sealin (see section 3.6). While this meant that flux rates had to be kept relatively low, limiting the range of our microfluidic characterization, it did not affect the performances of the device when used as a droplet detector, as will be showed by confronting these results with the measurements obtained with the experimental set-up described in section 4.1. For the second application there was no need for high imput flux rates and we did not use a T-junction set-up but an alternate droplet generator, so these measurements were unaffected by the type of sealing used.

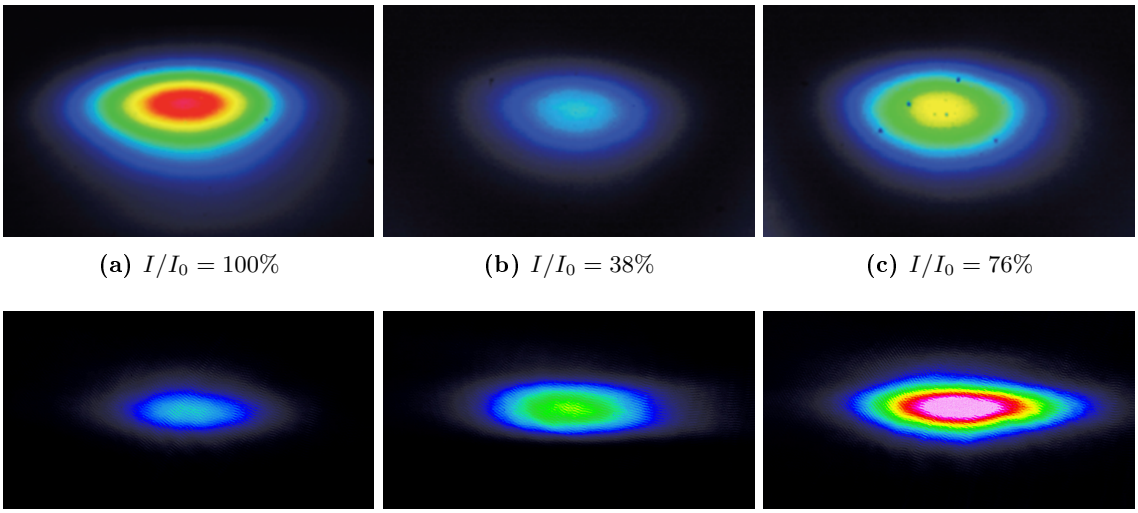

(a) $I/I_0 = 100\%$ **(b)** $I/I_0 = 38\%$ **(c)** $I/I_0 = 76\%$

(d) air **(e)** water **(f)** hexadecane

Figure 5.1: Examples of near field images of waveguides coupled to a 200μm wide microfluidic channel. On the top the TE single mode of a z-propagating waveguide (a) before the channel was engraved, (b) with the coupled channel in air, (c) with the channel filled with hexadecane; on the bottom the TM single mode of an y-propagating waveguide crossing a 200μm microfluidic channel (d) in air, (e) water and (f) hexadecane.

5.3 Experimental Set-up for Time Resolved Measurements

The acquisition system of the near field experimental setup described in section 2.5 cosists in a CCD camera which is not suited for fast or long aquisitions (it can only record up to 32 subsequent images). A more responsive acquisition system was needed for opto-microfluidic applications.

For the applications studied in this work there was no need to acquire the intensity profile of the modes but simply the overall output intensity of the wavdeguide, a simple photodiode was chosen, which integrsated the incoming signal and allowed for fast acquisition. A transimpedance was inserted in series to the photodiode in order to amplify the photo-generated current signal and convert it into a voltage signal, which was monitored and recorded with an Agilent MSO-X 2012A oscilloscope. Again, the same PHD 2000, Harvard Apparatus syringe pumps used during the droplet generator characterization (see

section 4.1) were employed for fluids injection in the microfluidic channels.

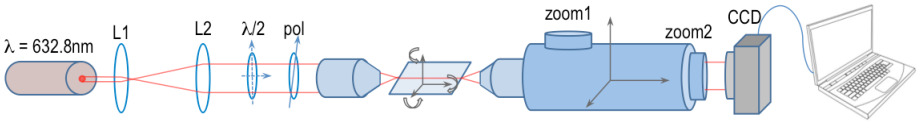

Figure 5.2: Scheme of the near field experimental setup used to perform time resolved measurements of the transmitted intensity exiting from the collecting waveguide while droplets are flowing.

5.4 Droplet Detection and Triggering

The device used for our tests in droplet detection consists in a $LiNbO_3$ with an integrated cross-junction used in a T-junction configuration with an array of Ti in-diffused z-propagating waveguides crossing the main channel at a right angle. The chip was sealed usign a sandblasted glass cover. The fluids used for this application were mineral oil (with no surfactant added) for the continuous phase and Milli-Q^{TM}water for the dispersed phase. The intensity signal from the TE single-mode of the brightest z-propagating waveguide was registered during the passage of the generated droplets.

The voltage signal generated as a single droplet flows in front of the waveguide is a a square wave with the signal of the droplet being much lower than that of the continuous phase, as shown in Fig. 5.4. The plateus for the continuous and dispersed phases are connected by sharp peaks, marking the passage of the advancing and the receding menisci in front of the waveguide.

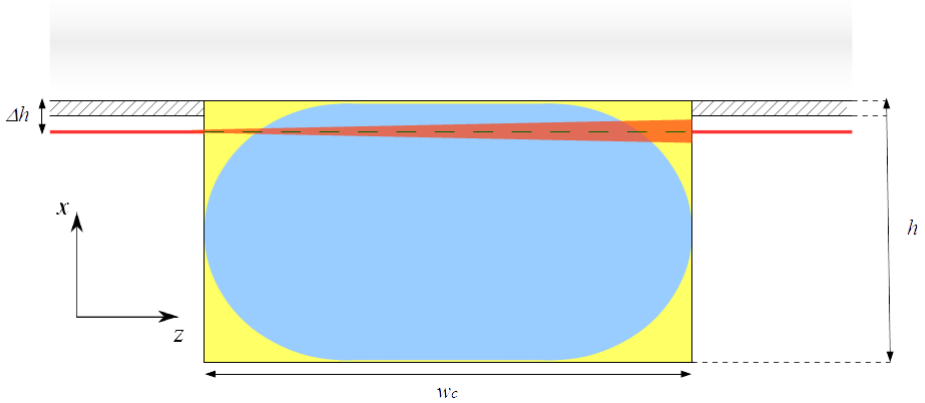

Figure 5.3: Front-view sketch of the droplet flowing in the microfluidic channel, showing the height Δh at which the waveguide illuminates the droplet and collects the transmitted light. The cone of light is simply meant as a guideline and in no way indicative of the actual light path.

To estimate the precision on the determination of the time instant at which the meniscus reaches the waveguide, we measured the time interval δt between the instants at which the

signal reaches 16% and 84% between the average voltage of the higher and lower plateau (Fig. 5.5). This estimation depends on the velocity and the shape of the droplets, which are again dependent on the chosen flow rates.

Δt was found to vary from $(377\pm4)\mu$s at the minimum flux rate tested ($Q_c = 10\mu$l/min, $Q_d = 1\mu$l/min) down to $(50 \pm 1)\mu$s for the maximum flow rates ($Q_c = 40\mu$l/min, $Q_d = 60\mu$l/min).

The first application for our device was the fast triggering of the droplets during their flow. In microfluidics research the standard experimental setup for the measure of droplets production frequency is the setup described in section 4.1, which requires a microscope, a fast camera, high data storage capacity to record the image sequences, a software for the analysis of the images (which is very hard to implement or requires the use of expensive commercial software) and time to post-process the sequences to gain the various droplet parameters. In addition, when droplet production frequencies reach an order of 1kHz or more, a real time image processing becomes really difficult.

The great advantage of our microfluidic setup is that it only requires a low power laser (we used a 1mW diode laser with an intensity coupled with to waveguide of around 400μW) and a photodiode with simple electronics triggering a square wave, while the two objectives used to couple the laser to the imput waveguide and to collect the signal of the output waveguide could easily be substituted with a couple of fibers directly connected to the microfluidic device (with the added benefit of doing away with alignement procedures).

To analyze the response of the system and to obtain measures comparable with those obtained with the standard microfluidi setup we recorded the signal from about 100 droplets at a time, changing the imposed flow rates of the continuous and dispersed phases. A software was developed by Dr. Giacomo Bettella[1] to analyze the output voltage from the oscilloscope in order to obtain the average voltage value of each plateau (excluding the peaks relative to the menisci) and the instant at which each slope reached its half height.

The analysis of the droplet time interval was performed by the software as follows: the software recovered the time instant of all the advancing menisci and the time difference Δt^a between two subsequent advancing menisci was calculated (Fig. 5.6). From the distribution of all the Δt^a's the average Δt^a_{av} and the dispersion σ^a_t were calculated. The same analysis was performed for the receeding menisci time difference Δt^r. Both results were combined to calculate the average time of passage of a single droplet in front of the waveguide Δt^d_{av}.

The flows rates tested for this application were $Q_c = 10$, 20, 30, 40μl/min for the continuous phase and $Q_d = 0.1$, 0.2, 0.4, 0.6, 1.0, 1.2, $1.5\times Q_c$ for the dispersed phase.

We measured the relative difference $(\Delta t^a_{av} - \Delta t^r_{av})/\Delta t^a_{av}$ between the average time interval Δt^a_{av} of the advancing menisci and the one calculated for the receeding menisci Δt^r_{av} and found it to be always $\leq 0.2\%$ and no systematic trends were noticed. The dispersion of Δt^a and Δt^r is also compatible within 10%.

The comparison between the Δt^a_{av} obtained by the integrated optical trigger and the time intervals Δt^m_{av} obtained with the microscope setup with the same flux rates is shown

[1] Private communication, G. Bettella PhD, Lithium Niobate group of the physics department of Padova

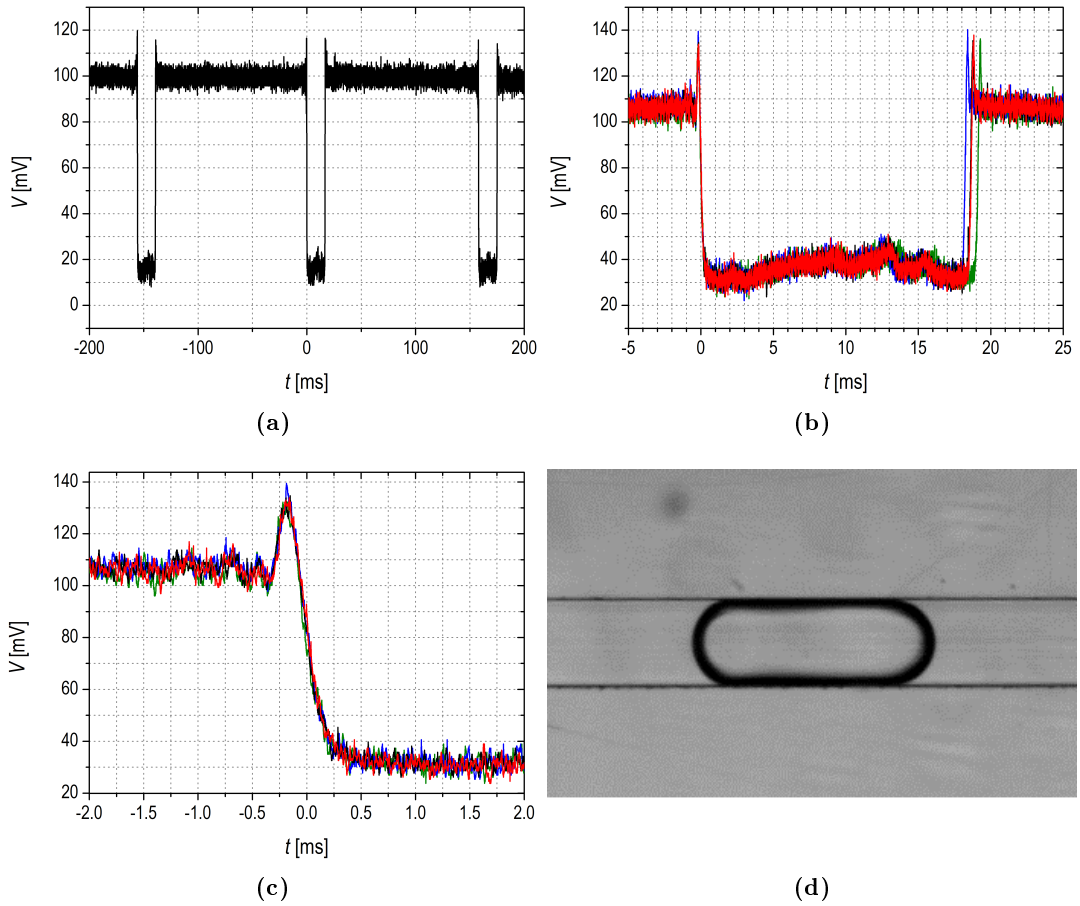

Figure 5.4: Example of the voltage signal from the photodiode at the passage of the water droplets through the cross-junction in a T-junction configuration. (a) signal from three subsequent droplets; (b) superposition of the signal of four different droplets, triggered on the negative slope, corresponding to the advancing meniscus; (c) detail of the superposition of four different peaks corresponding to the receeding meniscus; (d) microscope image of a droplet generated in the same conditions.

in Fig. 5.7 (the logarithmic scale is used to better visualize all sets of data. For logistical reasons we could not conduct simultaneous measurements with both the microfluidic setup and the integrated waveguide trigger. This means that the measurements were conducted in different laboratories in different days and possibly at different temperatures (our setups lacked a temperature control system). Temperature affects both the fluids dynamic viscosity (for instance hexadecane shows a 13% decrease in viscosity with a temperature increase from 298°C to 303°C and 26% from 298°C to 308°C) and surface tension. Therefore fluctuations due to the reproducibility of the measurements performed and also the reproducibility of the droplet generation has to be taken into account when comparing the data. Nevertheless the results from the microscope images and the optical trigger are in reasonable agreement reassuring us on the performances of our integrated optical system.

Indeed the integrated optical trigger performs better than the standard system in some respects as can be seen by comparing the dispersion in the sample data (each consisting

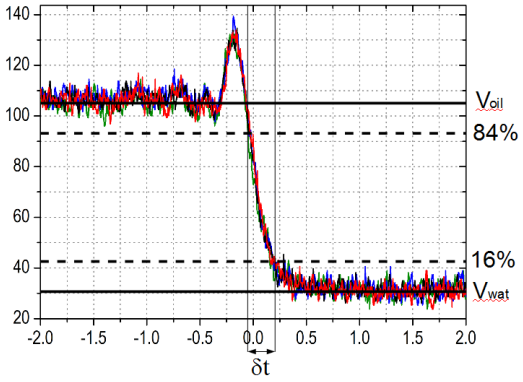

Figure 5.5: Sketch rapresenting the measure of the time interval δt between the instants at which the signal reaches 84% and 16% of the difference between the average voltage of the oil and of the water signals. This determines the precision of our droplet counter.

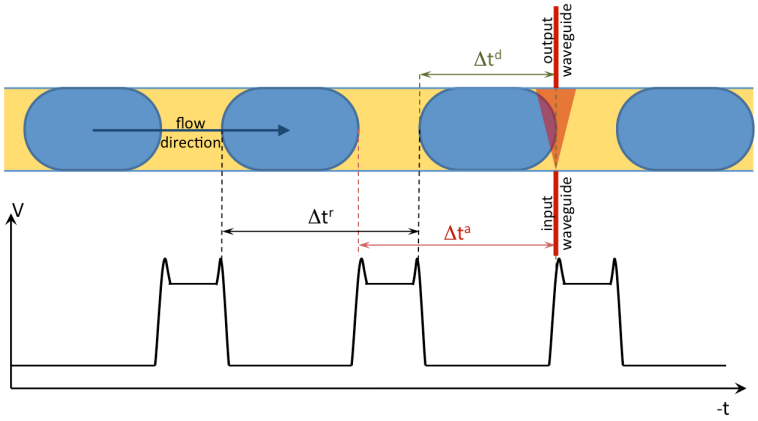

Figure 5.6: Sketch showing the time intervals measured with the integrated system as the droplets pass in front of the waveguide.

in the measured Δt of about 100 droplets) shown in Fig. 5.9. In most cases (except at the lowest flow rates) the optical trigger gives a much lower dispersion in the determination of Δt. This suggests that part of the fluctuations detected with the microscope are due to the experimental setup rather than to the droplet generator itself.

The time of passage of a single droplet Δt^d, i.e. the time difference between the the instant in which the advancing and receding menisci pass in front of the waveguide was compared with the one obtained with the microscope setup (Fig. 5.8). As stated before the waveguide is located at an estimated distance of $(6 \pm 2)\mu$m from the glass top wall of the channel. Therefore the recorded time interval Δt^d corresponds to the passage of the topmost section of the droplet (Fig. 5.3), and not of the droplet in its full length). The length registered by the camera connected to the microscope refers instead to the horizontal middle section of the droplet, which corresponds to the maximum extension of the droplet. In order to take this into account we calculated the difference $\Delta L/2$ between the meniscus width at the middle plane and at the plane intersected by the waveguide. The approximation for the three dimensional shape of the droplet discussed in section 3.4.1 was

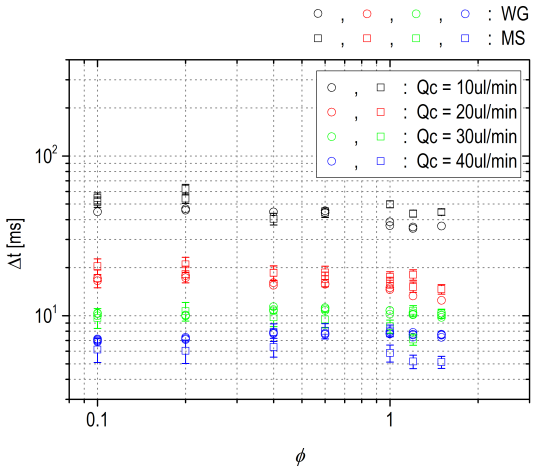

Figure 5.7: Comparison between the time interval between droplets measured with the microfluidic setup (MS) employing a microscope and a fast camera and the integrated optical trigger (WG) employing the optical waveguides described in this section. Logarithmic scales were set for better visualization and error bars are not shown for the same reason. Repeated measurements were reported when available.

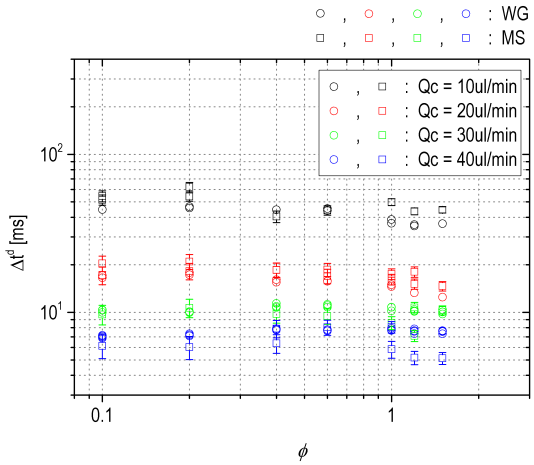

Figure 5.8: Comparison between the time passage of a droplet measured with the experimental system (MS) and the integrated optical trigger (WG). Error bars for the points referring to the integrated system are smaller then the markers.

adopted, supposing that the curvature radius of the droplet on the plane perpendicular to the cross-junction plane is $h/2$, with h the height of the channels. The estimated length triggered by the waveguide is then:

$$L - \Delta L = L - \left(h - \sqrt{h\Delta h + \Delta h^2}\right). \tag{5.1}$$

The time interval corresponding to this length can be calculated for the length L_{av} at the middle plane and the velocity v_{av} obtained from the microscope images analysis. This approach leads to the following estimation for the time interval:

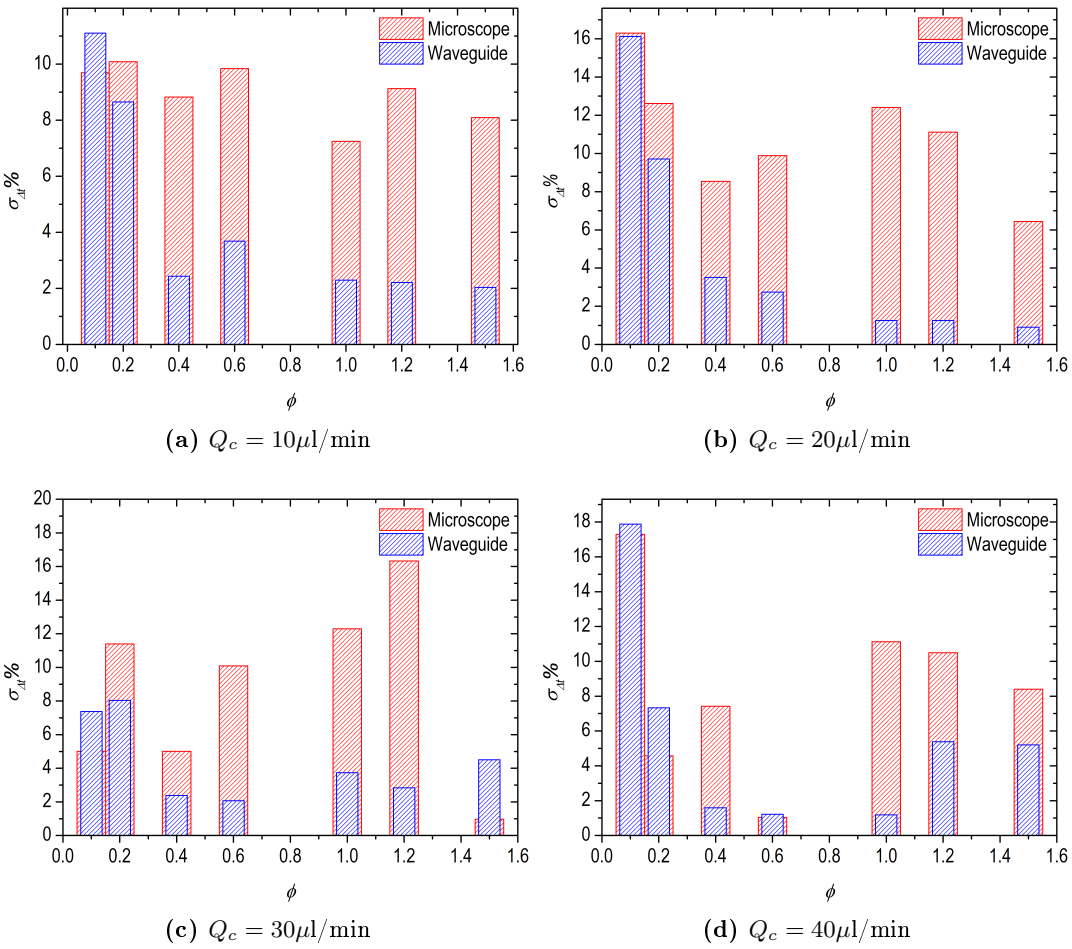

(a) $Q_c = 10\mu$l/min **(b)** $Q_c = 20\mu$l/min

(c) $Q_c = 30\mu$l/min **(d)** $Q_c = 40\mu$l/min

Figure 5.9: Comparison between the dispersion $\sigma^{\%}_{\Delta t}$ of the Δt^a distributions obtained by the standard setup (microscope - red columns) and the integrated optical waveguide system (waveguide - blue columns) for each tested value of the flow rate ratio ϕ and continuous phase flow rate Q_c.

$$\Delta t^d_{ms,av} = \frac{1}{v_{av}} \left[l_{av} - \left(h - \sqrt{h\Delta h + \Delta h^2} \right) \right] \tag{5.2}$$

The comparison between the passage time obtained with both system is reported in Fig. 5.8 for all values of the continuous phase and flow rate ratios; the error bars relative to the average Δt_{wg} from the waveguide trigger are always smaller than the marker, while those of the microscope are considerably larger due to the error propagaton from equation (5.2), but in general these measurements show good compatibility, again demonstrating the good performances of our integrated device.

5.5 Refractive index Sensing

The final characterization was carried out to explore possible sensing applications for our device. Our aim was to find a correlation, if any, between the output signal of the

waveguide from the droplets passage and the refractive index of the dispersed phase.

The tests were performed by preparing aqueous solutions of $CaCl_2$ at different concentration. $CaCl_2$ is insoluble in oil and offeres a large range of refractive index values without increasing the viscosity excessively. The tested solutions were 2.5%, 5%... 20% $CaCl_2$ in MilliQ®water, with pure water used as a control solution.

The first measures were performed in a T-junction configuration by recording the signal of about 100 droplets for each different solution. The waveguide signal was rescaled by the voltage signal of the coupled laser beam and for each droplet the ratio $R_V = V_d/V_c$ was calculated, which is the ratio between the measured voltage from the droplet and the voltage from the continuous phase.

While the measured values of R_V had good repeatability in the 100 droplet series, with a maximum standard deviation of $\sigma_{R_V}^{\max} = 5\%$, no defined trend was found when the R_V^{av} averages from different solutions were confronted. This is probably due to the experimental procedures emplyed, which involved disconnecting the tubings and changing the syringes for any new solution. A relatively long time was needed for the new solution to flow through the tubings and into the device, and then time was needed for the system pressure to stabilize. During this time (about half an hour between every solution). During this time enviromental conditions could change significaly, even altering the response of the system. It is also worth noting that due to the long time needed between every measurment, data acquisition cannot always be performed in the same day. In addition, waveguide output could also be influenced by misalignements of the waveguide with respect to the coupled laser, due to vibrations, which in time caused a decrease in the output voltage.

The main problem with this type of measurements was the lack of a reliable reference signal with which any single droplet could be compared: the signal from the droplets of different solutions were recorded several minutes (or even hours) one from the other. A reference signal was needed to account for the external conditions.

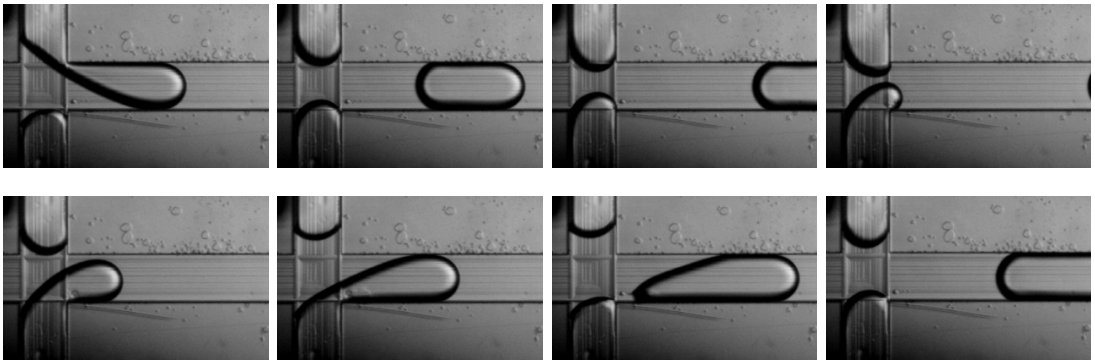

Figure 5.10: Alternate droplet production in a cross-junction configuration. Different solutions are injected from the top and bottom inlets. The flow rates were set to $Q_c = 10\mu$l/min for the continuous phase, $Q_d^w = 3\mu$l/min for the MilliQ®water (bottom inlet) and $Q_d^s = 2\mu$l/min for a 5% $CaCl_2$ aqueous solution (top inlet). The images were taken at a 20ms interval, from top left to bottom right.

This led us to change the setup configuration trying a new approach proposed in a recent paper by Surya *et al.* [129], i.e. an alternating droplet generation (Fig. 5.10): by injecting the solution in one of the lateral inlets and pure MilliQ®water in the other, by properly tuning the flow rates, we managed to produce alternating droplets of solution and pure water. This ensured that the reference signal of the MilliQ®water droplet was always taken in the same conditions as the solution droplet since they were produced just a few milliseconds apart. The relatively high flow rate of the continuous phase $Q_c = 10\mu$l/min compared to the dispersed phases flow rates ensured that the alternating droplets never merged: as shown in Fig. 5.10 there is always a layer of continuous phase between the two dispersed phases and as soon as a droplet is generated the neck recoils back in the inlet (as was the case in the T-junction configuration) and this allows the other dispersed phase to push into the channel and form another droplet.

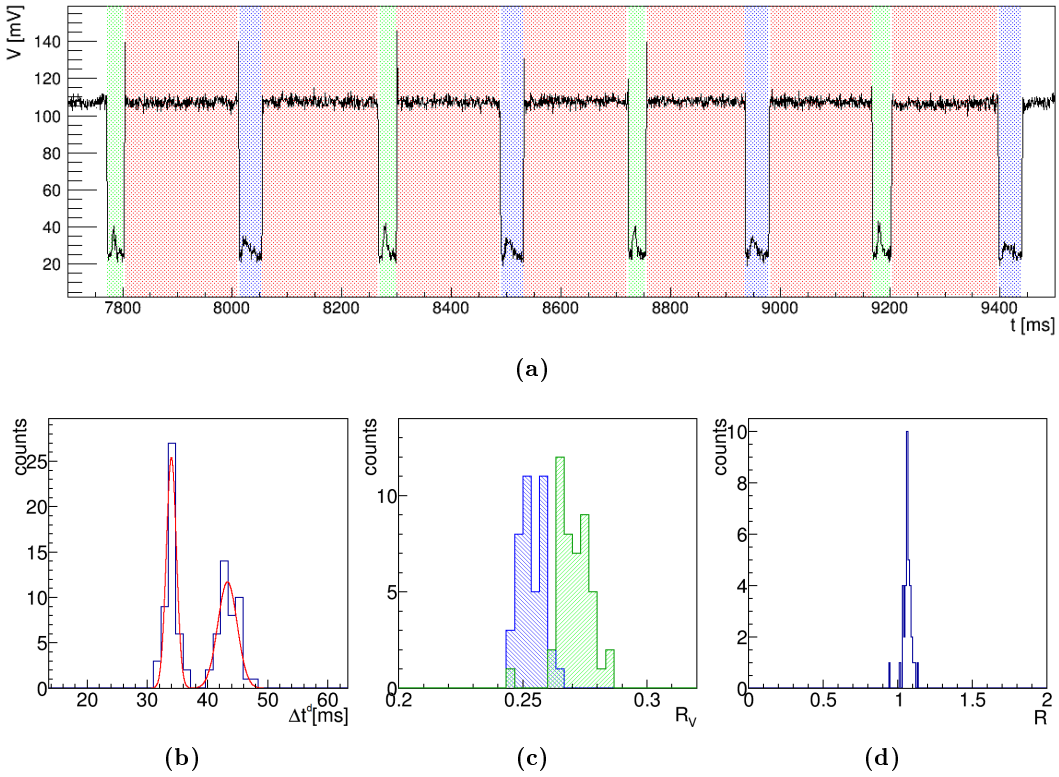

Figure 5.11: Software droplet recognition and calculations for the sensing of the refractive index of a water-based solution in the opto-microfluidic device in cross-junction configuration: (a) droplet recognition between the reference solution (blue - MilliQ^{TM}water) and the solution to be measured (green - 5% $CaCl_{2(aq)}$; (b) distribution of the passage time of droplets; (c) $R_V = V_d/V_c$ distribution, the colors indicating the solution s in green and the reference pure water w in blue; (d) $R = R_V^s/R_V^w$ distribution.

The waveguide signal from the alternating droplets is reported in Fig. 5.11a, where the blue areas indicate the reference pure water droplets, green areas indicate the droplets containing the saline solution and red areas indicate the continuous phase signal. The flow rates of the dispersed phases were kept different (at 2 and 3μl/min): this results in two

well separated Δt distributions which allow for easy droplet sorting.

To analyze the signals we used a modified version of the software used in section 5.4 to recognize droplets with difference length by measuring and comparing their passage time Δt (Fig. 5.11b shows the time passage distribution for both continuous phases).

As before the program calculates the ratio $R_V = V_d^{s,w}/V_c$ for all droplets, which is the dispersed phase voltage rescaled over the voltage of the continuous phase voltage signal preceeding the voltage. The distribution of R_V can be seen in Fig. 5.11c and the different colors are relative to the solution and pure water. V_c, V_d^s and V_d^w were calculated as the mean voltage of the corresponding segment, peaks excluded. While this is straight-forward in the case of the continuous phase (which appears as a plateu), the signal from the droplets has a more complicated profile (generally with a peak at the center), possibly due to the shape of the droplet. We still chose to use the mean voltage for the droplets since we still lack a model able to predict how the signal is affected by the shape of the droplet. A first hypothesis is that the droplet signal is affected mainly by the refractive index of the solution since the shape of the droplet was the same for every solution.

In this alternate droplet configuration the software also calculated the ratio $R = R_V^s/R_V^w$ of a droplet of the solution and the water droplet preceeding it. R was thus defined as the actual response of the device to the refractive index of the solution (as a relative measure rescaled to the signal of the pure water droplet). An example of the distribution of R can be seen in Fig. 5.11d.

Six series of around 50 couples of droplets were recorded with our system for each concentration of the $CaCl_{2(aq)}$ solution. For each droplet series the repeatability of $R = R_v^s/R_V^w$ was verified to be as good as in the T-junction configuration, with a standard deviation $\sigma_R < 4\%$.

The great advantage of this procedure is in the overall reproducibility, as this configuration showed a monotonic trend in the rescaled droplet signal ratio R with an increase in the $CaCl_2$ concentration, even if the measurements were performed at different times in different days.

For each of the six series at a fixed concentration the measurements of R were performed after repeating all the tubings and syringe connection procedures. For each set the set the standard deviation $\sigma_R(C_\%)$ was calculated and the maximum was found to be $\sigma_R^{max} = 0.01$.

The average value $R_{av}(C_\%)$ and its random error $\sigma_{R_{av}}$ were calculated for each value of the concentration and were plotted in Fig. 5.12a while in Fig. 5.12b we reoport the plot of the refractive index of different $CaCl_2$ solutions as a function of the concentration and for six different temperatures as reported by Tan and Huang [130]. Our device shows two different regimes, the first for $CaCl_2$ concentrations $\leq 2.5\%$ where the sensitivity of our system $\Delta R/\Delta C_\%$ is below 1%, and a second regime for $C_\% > 2.5\%$ where the device shows a monotonic increasing trend.

While the number of points is not enough to infer an accurate dependence of the device response on the concentration, we can still state that the trend for R and for the refractive index as a function of concentration share the same trend, increasing monotonically as the

concentration increases (at least for concentrations higher than 2.5%).

The monotonicity region between $C = 2.5\%$ and $C = 17.5\%$ is well described by the weighted linear fit represented in the plot by a red line. The gray dotted lines indicate that all the points stay at a distance from the fit compatible with $\sigma_R^{max}(C_{\%})$.

The sensitivity S was deduced by the slope of the interpolating line: $S_C = \partial R/\partial C = (1.14 \pm 0.04)\%$. The minimum concentration difference $\Delta C_{\%}^{min} = \sigma_R^{max}(C_{\%})/S_C = 0.88\%$. If the refractive index of the solutions was the only property affecting R we would find that the minimum refractive index difference Δn^{min} between two substances to be resolved by the sensor employing the described protocol could be estimated as $\Delta n^{min} = \sigma_R^{max}(C_{\%})/S_n = 2 \cdot 10^{-3}$.

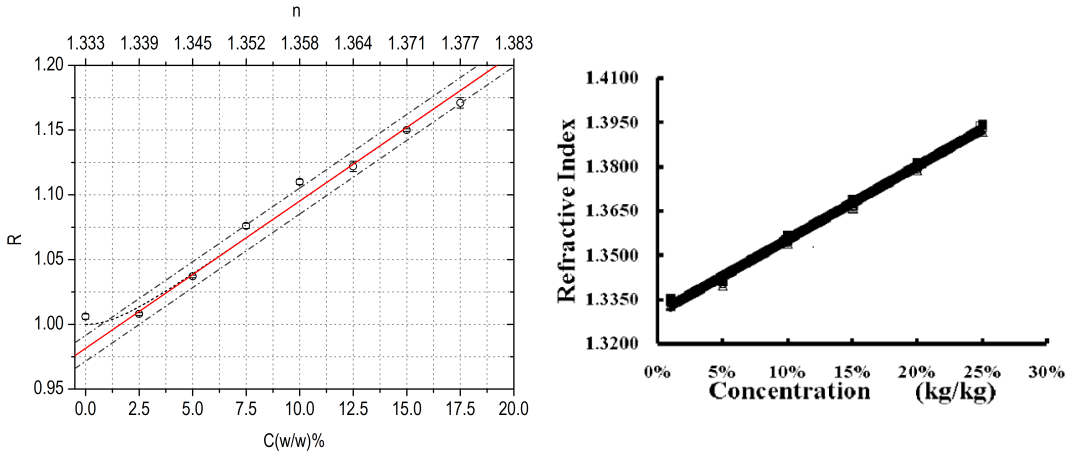

Figure 5.12: (a) Plot of R as a function of the concentration. The refrative index corresponding to the $CaCl_2$ concentration is reported at the top. The red line represents the weighted linear fit of data in the linearity region from a concentration of 2.5% up to 17.5%. Each experimental point was obtained as the average among 6 independent sets of measurements. The dash-dot gray lines are set at a distance $\sigma_R^{max} = 0.01$ from the linear fit. (b) Plot of the refractive indices of $CaCl_2$ solutions as a function of concentration (from 1 to 25%) and for 6 different temperature values from 293.15°K to 318.15°K [130].

While we cannot yet prove that the system can be used to directly measure the refractive index of the different solutions, the fact that we obtained similar trends for the response of our device and the refractive index as a function of concentration constitutes a good starting point for the realization of a refractive index sensor. Further confirmation will require other measurements with other types of solutes, such as glucose or potassium cloride, to take into account the effects of viscosity. In addition, as stated before, a model of how the waveguide illuminates the droplet and collects the refracted light would help us quantify the effects of the droplet geometry on the response of the system, while the realization of a chip with the waveguides at the center of the channel would reduce the effect of geometry altogether.

5.6 Summary and Future Prospects

In this chapter the possibility to couple titanium in-diffused waveguides with a microfluidic channel have been proved. The first prototype showed high repeatability and performances similar or better than traditional experimental setups when used as a droplet trigger and counter. In particular, the system showed a very fast response, limited only by the electronics used for the detection and recording of the output signal, allowing fro real-time measurements and reducing the needed data storage and elaborated image analysis software: a waveguide replaces the fast camera and several megabytes of image sequences are reduced to a few kilobytes of text files containing the electric voltage as a function of time.

The next steps in the development of a fully portable device will aim at doing away with the laboratory setup used in our analysis by adding quick-lock inlets and outlets for the fluids, and by gluing optical fibers to the ends of the integrated waveguides to inject and collect the light signal, reducing the amount of preliminary operations before a measurement and removing the need for an optical table, objectives, lenses and attenuators. The far reaching objective will be the complete integration of the light source and the detection electronics, possibly even the pumping system.

In addition, futere reaserches will also be focused on increasing the sensing capabilities of future devices with the integration of additional optical stages. An holographic Bragg grating has already been integrated with an optical waveguide on a single lithium niobate chip which presented a region Fe doped. Another improvement will be the employment of a splitting and recombining waveguide for the direct measurement of the droplet length and velocity by means of its double triggering with a single light imput and output.

Our prototype already demonstrated its potential for sensing application by being characterized as a refractive index sensor. It presents a detection sensitivity of $2 \cdot 10^{-3}$ is greater of other examples reported in literature where the refractive index of flowing droplets is measured [1, 131]. The presented measurements required around 50 droplet couples, requiring only 20s, which were enough at the employed flow rates of a few μl/min. The device is able to sustain much higher flows and, while still working inside the squeezing regime, more than 25 droplet couples per second could be produced and analyzed. Even higher flows could be reached by positioning the optical waveguides at the center of the channel, meaning that our system would be able to sense smaller droplets produced in the dripping regime. Moreover, although no control on the temperature of the system was added, the immediate comparison between the reference liquid and the solution to be identified made the measurement highly reproducible at normal ambient conditions.

The presented prototype is also able to distinguish the refractive index of two droplets when with a 100% probability Δn is suffeciently high, for example in the case of a single water droplet and a single droplet containing 15% $CaCl_{2(aq)}$, as shown in Fig.5.13. The ability to sort different solutions on a droplet-to-droplet basis (albeit with the current limitation of having a sufficiently high Δn) means that that in the future devices based

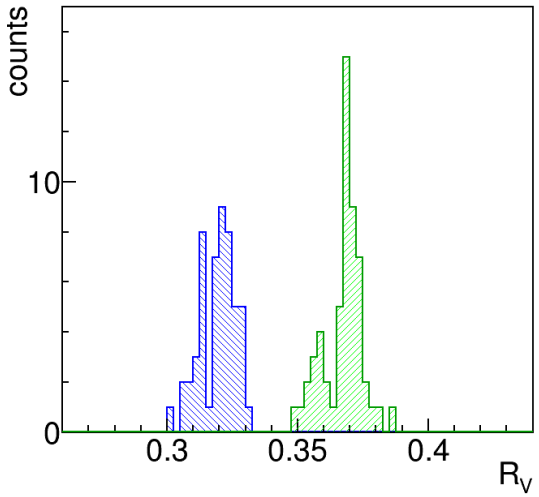

Figure 5.13: Voltage ratio R_V for alternating water droplets (blue) and 15% $CaCl_{2(aq)}$ droplets. Both distributions have a standard deviation $\sigma = 8 \cdot 10^{-3}$ and an average value of 0.319 ± 0.001 and 0.368 ± 0.001ì respectively. This means that the distribution are separated by a distance of 7σ

on this first prototype could be employed in digital microfluidics (several examples of microfluidic logic ports exist [132, 133], and droplets with different solutions could represent the binary values 0 and 1) and pharmaceutical applications (single droplets could be used to mark the start and end of different droplet sequences to be sorted and processed in different ways).

Conclusions

This thesis carried out a proof of concept of a new opto-microfluidic device in lithium niobate based on the integration of both a microfluidic stage for water-in-oil droplet generation and an optical stage for droplet detection, presenting its development, the successful realization of a working prototype and its characterization.

To the best of our knowledge, this prototype is the first to use lithium niobate as the substrate for an opto-microfluidic device with droplet detection capabilities integrated in a microfluidic system.

The realization of the optical stage started from basic knowledge and long experience of our research group in the realization of titanium in-diffused waveguides in lithium niobate. The realization of channel waveguides supporting only the fundamental TE and TM mode for light at 632.8nm required the optimization of the photolitographic, deposition and diffusion processes. In particular the diffusion process characterized by RBS and SIMS measurements and a FEM simulation was used to predict the number of supported TE and TM modes for channel waveguides of different width. A dedicated near field setup to characterize the waveguides was setted and the obtained guide modes were compared with the simulations. The transmission of the waveguides was measured in order to calculate the attenuation coefficient α, which is a useful indicator of a waveguide quality, and the results were found to be comparable to those found in literature.

The design, fabrication and characterization of the microfluidic stage required much more effort since this was a new field of reaserch for our group. A study on the wettability properties of lithium niobate had just been realized along with the first tests on a T-junction droplet generator realized by laser ablation [12], which proved to be a very effective system but presented a roughness of the channel side walls too high for the light to be collected by an integrated optical stage.

The possibility to realize the microfluidic stage using a dicing saw was tested with good results. The lateral surfaces of the channels realized with this technique had an almost optical quality, which made the coupling of two waveguides at each side of the channel possible.

Two different methods for sealing the microfluidic channels engraved on the surface of the crystal were presented, both using a glass cover glued to the crystal. This method was used in place of the previos sealing method using a polymeric cover made of PDMS, offering more stiffness, durability, resistence to pressure (up to a few bars) as well as resistence to

chemical agents such as acids or organic solvents.

The generation of water-in-oil droplets inside a cross-junction used in a T-junction configuration in the squeezing regime was investigated to characterized the microfluidic performances of our droplet generator, and the results were found to be comparable with the performances of other T-junction droplet generators found in other materials. Our analysis was also compared to the theoretical scaling laws describing the break-up of the dispersed phase typical of cross-flow geometries. An optical microscopy system was employed to record images of produced droplets and an image analysis software developed by LaFSI group of Padova allowed for the analysis of the image sequences. The output data from this software was elaborated using a data analysis program developed by our group, and the results showed a very stable production frequency and length of the droplets (the most importat requirement for a droplet generator), comparable with the T-junction droplet generator developed by our group and with the most recent microfluidic devices reported in literature. The comparison with the scaling law found in literature showed some discrepancies for the lower values of the flux rate ratio ϕ, possibly indicating a different regime or a systematic error in the calculated droplet volumes, but showed a similar behaviour at the higher flux rate ratios. Further measurements would be needed to more accurately describe the behaviour of our device in comparison to these scaling laws.

The last part of this thesis dealt with the coupling of optical waveguides to the microfluidic channels and the final realization of Lab-On-a-Chip prototype able to generate and detect droplets. As stated before, the microfluidic channels obtained by mechanical micromachining proved to be suitable for the coupling of both the injecting and collecting waveguides.

The near field setup was implemented to perform time resolved measurements and this allowed for the detection of the transmitted intensity from the waveguides as the droplets were flowing. A dedicated software was developed by Dr. Giacomo Bettella to analyze the signal modulated by the passage of the droplets.

The prototype was employed to measure the time of passage of the droplets as they flowed in front of the waveguides, and the results were compared with the measurements obtained using the microscopy setup. The comparison showed very good agreement, and the temporal dispersion of the data from the integrated optical system were demonstrated to be lower than those obtained from the standard setup, especially at higher production frequencies.

The last application for our device was its employment as a refractive index sensor for aqueous solutions. The cross-junction was used in a double droplet configuration employing three different fluid phases (oil, pure water and an aqueous solution). This way we obtained a droplet generation which alternated droplets from the two injected dispersed phases (pure water and aqueous solution). This method allowed to get, within a few tens of milliseconds, two signals relative to the transmitted intensity of the pure water droplet and the solution droplet, which ensured that the measured signal and its reference were recorded in the same enviromental conditions, greatly improving the reproducibility of the system.

The sensor was proved to have a linear response with the solute concentration ($CaCl_2$ in this case) in a range $C = [2.5, 17.5]\,\%$ with an overall sensitivity of $S_c = 1.14\%$, corresponding to a range $n = [1.339, 1.377]$ and a sensitivity $\Delta n^{min} = 2 \cdot 10^{-3}$ for measurements resulting from 50 successive droplet couples.

The first advantage of our prototype, when used for droplet counting, is the complete integration of the optical stage and its very low response time compared the the standard experimental setups, which require a microscope, a fast camera, several gigabytes of data storage and an image analysis software. In this chip the role of the microscope is covered by by the optical waveguides and the output signal is a single voltage signal, which can be easily processed and analyzed. Further possible integrations, easily achievable with standard techniques, could see optical fibres glued to the crystal to inject and collect the light into and from the waveguides, and quick-lock inlets for a fast insertion of the tubings.

The second advantage of this chip is the high structural and chemical stability and biocompatibility compared to polymeric devices, which can suffer instead from swelling, progressive degradation, poor chemical resistence and absorption of solvents and analytes (chemical or biological). In addition the fact that tested liquids are carried inside droplets means that there is no interaction between the channel walls and possible reagents or analytes, reducing the risk of contamination exists when measurements of different solutions are being made in quick succession.

The ability to perform refractive index measurements on single droplets in a very short time with an integrated system is also very appealing both for microfluidics research and microfluidics applications in the field of biology, medicine, pharmacology and enviromental sciences, as droplets can carry potentially any sample soluble in water and can even act as chemical reactors to study phenomena at the microscale. With a proper functionalization it could also be possible to create oil droplets in water, which would further increase the range of possible applications.

As a last remark we mention the advantages only possible thanks to the exploitation of lithium niobate as a substrate for both optics and microfluidics. This material has already been employed for moving droplets via surface acoustic waves induced by piezoelectricity. The voltage can be applied through interdigital electrodes deposited on its surface, and this technique has already been proved to be able to move droplets or even trap particles or cells in a specific region of the channel during the fluid flow. The trapping of particles can also be performed by exploiting the electric fields produced on the surface of lithium niobate after exposure to light due to its photorefractivity. This effect can also be used to modify the refractive index of the material to realize holograpgic Bragg gratings, beam splitters or wavelenght filters. This device offers the possibility to design very complex optical stages, for example for the simultaneous employment of different wavelengths or to excite fluorescent solutes inside droplets with a pump wavelength and collect the output signal at a greater wavelength by filtering the pump signal with a Bragg reflecting grating.

With these optical stages and the addition of miniaturized electronics for chip control and data recording and solid state laser sources a true self-sufficient LOC in lithium niobate

seems like a real possibility.

The results discussed in this thesis are meant as the first proof of the wide spectrum of possibilities lithium niobate offers for the realization of Lab-On-a-Chip devices, making it a prime material to study and employ in the growing field of opto-microfluidics and in other fields of reaserch that would benefit greatly from a multipurpose, inexpensive and easy to use sensing device.

Bibliography

[1] Emanuel Weber, Dietmar Puchberger-Enengl, and Michael J Vellekoop. In-line characterization of micro-droplets based on partial light reflection at the solid-liquid interface. In *ASME 2012 10th International Conference on Nanochannels, Microchannels, and Minichannels collocated with the ASME 2012 Heat Transfer Summer Conference and the ASME 2012 Fluids Engineering Division Summer Meeting*, pages 589–595. American Society of Mechanical Engineers, 2012.

[2] Martha-Elizabeth Baylor, Benjamin W Cerjan, Charlotte R Pfiefer, Robert W Boyne, Charles L Couch, Neil B Cramer, Christopher N Bowman, and Robert R McLeod. Monolithic integration of optical waveguide and fluidic channel structures in a thiolene/methacrylate photopolymer. *Optical Materials Express*, 2(11):1548–1555, 2012.

[3] Roberto Osellame, Valeria Maselli, Rebeca Martinez Vazquez, Roberta Ramponi, and Giulio Cerullo. Integration of optical waveguides and microfluidic channels both fabricated by femtosecond laser irradiation. *Applied physics letters*, 90(23):231118, 2007.

[4] Rebeca Martinez Vazquez, Roberto Osellame, Marina Cretich, Marcella Chiari, Chaitanya Dongre, Hugo JWM Hoekstra, Markus Pollnau, Hans van den Vlekkert, Roberta Ramponi, and Giulio Cerullo. Optical sensing in microfluidic lab-on-a-chip by femtosecond-laser-written waveguides. *Analytical and bioanalytical chemistry*, 393(4):1209–1216, 2009.

[5] F Bragheri, P Minzioni, R Martinez Vazquez, N Bellini, P Paiè, C Mondello, R Ramponi, I Cristiani, and R Osellame. Optofluidic integrated cell sorter fabricated by femtosecond lasers. *Lab on a Chip*, 12(19):3779–3784, 2012.

[6] Matthias F Schneider, Zeno Guttenberg, Stefan W Schneider, Kumudesh Sritharan, Vanessa M Myles, Umut Pamukci, and Achim Wixforth. An acoustically driven microliter flow chamber on a chip (μfcc) for cell–cell and cell–surface interaction studies. *ChemPhysChem*, 9(4):641–645, 2008.

[7] Leslie Y. Yeo and James R. Friend. Ultrafast microfluidics using surface acoustic waves. *Biomicrofluidics*, 3(1):1–23, 2009.

[8] HA Eggert, FY Kuhnert, K Buse, JR Adleman, and D Psaltis. Trapping of dielectric particles with light-induced space-charge fields. *Applied physics letters*, 90(24):241909, 2007.

[9] Michael Esseling, Annamaria Zaltron, Nicola Argiolas, Giovanni Nava, Jörg Imbrock, Ilaria Cristiani, Cinzia Sada, and Cornelia Denz. Highly reduced iron-doped lithium niobate for optoelectronic tweezers. *Applied Physics B*, 113(2):191–197, 2013.

[10] Michael Esseling, Annamaria Zaltron, Cinzia Sada, and Cornelia Denz. Charge sensor and particle trap based on z-cut lithium niobate. *Applied Physics Letters*, 103(6):061115, 2013.

[11] M Jubera, A García-Cabañes, José Olivares, A Alcazar, and M Carrascosa. Particle trapping and structuring on the surface of linbo 3: Fe optical waveguides using photovoltaic fields. *Optics letters*, 39(3):649–652, 2014.

[12] G Pozza, S Kroesen, G Bettella, A Zaltron, M Esseling, G Mistura, P Sartori, E Chiarello, M Pierno, C Denz, et al. T-junction droplet generator realised in lithium niobate crystals by laser ablation. *Optofluidics, Microfluidics and Nanofluidics*, 1(1), 2014.

[13] Tatyana Volk and Manfred Wöhlecke. *Lithium niobate: defects, photorefraction and ferroelectric switching*, volume 115. Springer Science & Business Media, 2008.

[14] Armin Rauber. Chemistry and physics of lithium niobate. *Current topics in materials science*, 1:481–601, 1978.

[15] Rs Weis and Tk Gaylord. Lithium Niobate: Summary of Physical Properties and Crystal Structure R. *Applied Physics A: Materials Science & Processing*, 37(4):191–203, 1985.

[16] P Lerner, C Legras, and JP Dumas. Stoechiometrie des monocristaux de metaniobate de lithium. *Journal of Crystal Growth*, 3:231–235, 1968.

[17] Wolfgang Sohler, DEY Dibyendu, REZA Selim, Hubertus SUCHE, Raimund RICKEN, et al. Erbium-doped lithium niobate waveguide lasers. *IEICE transactions on electronics*, 88(5):990–997, 2005.

[18] M Wöhlecke, G Corradi, and K Betzler. Optical methods to characterise the composition and homogeneity of lithium niobate single crystals. *Applied physics B*, 63(4):323–330, 1996.

[19] M Luennemann, U Hartwig, G Panotopoulos, and K Buse. Electrooptic properties of lithium niobate crystals for extremely high external electric fields. *Applied Physics B*, 76(4):403–406, 2003.

[20] E Bernal, GD Chen, and TC Lee. Low frequency electro-optic and dielectric constants of lithium niobate. *Physics Letters*, 21(3):259–260, 1966.

[21] X Y Du, M E Swanwick, Y Q Fu, J K Luo, A J Flewitt, D S Lee, S Maeng, and W I Milne. Surface acoustic wave induced streaming and pumping in 128° Y-cut LiNbO 3 for microfluidic applications. *Journal of Micromechanics and Microengineering*, 19(3):35016, 2009.

[22] Jinjie Shi, Xiaole Mao, Daniel Ahmed, Ashley Colletti, and Tony Jun Huang. Focusing microparticles in a microfluidic channel with standing surface acoustic waves (ssaw). *Lab on a Chip*, 8(2):221–223, 2008.

[23] AM Glass, D Von der Linde, and TJ Negran. High-voltage bulk photovoltaic effect and the photorefractive process in linbo3. *Applied Physics Letters*, 25(4):233–235, 1974.

[24] A Ashkin, GD Boyd, J iM Dziedzic, RG Smith, AA Ballman, JJ Levinstein, and K Nassau. Optically-induced refractive index inhomogeneities in linbo3 and litao3. *Applied Physics Letters*, 9(1):72–74, 1966.

[25] VL Vinetskii and NV Kukhtarev. Anomalous photostress and energy transfer in semiconductor holograph gratings. *Pisma v Zhurnal Tekhnischeskoi Fiziki*, 1:176–181, 1975.

[26] P. K. Tien and R. Ulrich. Theory of Prism-Film Coupler and Thin-Film Light Guides. *Journal of the Optical Society of America*, 60(10):1325, October 1970. bibtex: tien_theory_1970.

[27] R. J. Holmes and D. M. Smyth. Titanium diffusion into $LiNbO_3$ as a function of stoichiometry. *Journal of Applied Physics*, 55(10):3531, 1984.

[28] Masaharu Fukuma, Juichi Noda, and Hiroshi Iwasaki. Optical properties in titanium-diffused $LiNbO_3$ strip waveguides. *Journal of Applied Physics*, 49(7):3693, 1978.

[29] Kiyomasa Sugii, Masaharu Fukuma, and Hiroshi Iwasaki. A study on titanium diffusion into linbo3 waveguides by electron probe analysis and x-ray diffraction methods. *Journal of Materials Science*, 13(3):523–533, 1978.

[30] MN Armenise, C Canali, M De Sario, A Carnera, P Mazzoldi, and G Celotti. Evaluation of the ti diffusion process during fabrication of ti: Linbo 3 optical waveguides. *Journal of Non-Crystalline Solids*, 47(2):255–257, 1982.

[31] Grant J Griffiths and Roderick J Esdaile. Analysis of titanium diffused planar optical waveguides in lithium niobate. *Quantum Electronics, IEEE Journal of*, 20(2):149–159, 1984.

[32] Daniel Runde, Stefan Breuer, and Detlef Kip. Mode-selective coupler for wavelength multiplexing using linbo3: Ti optical waveguides. *Central European Journal of Physics*, 6(3):588–592, 2008.

[33] Ed L Wooten, Karl M Kissa, Alfredo Yi-Yan, Edmond J Murphy, Donald Lafaw, Peter F Hallemeier, David Maack, Daniel V Attanasio, Daniel J Fritz, Gregory J McBrien, et al. A review of lithium niobate modulators for fiber-optic communications systems. *Selected Topics in Quantum Electronics, IEEE Journal of*, 6(1):69–82, 2000.

[34] Yu N Korkishko and Vyacheslav A Fedorov. *Ion exchange in single crystals for integrated optics and optoelectronics*. Cambridge Int Science Publishing, 1999.

[35] Yuri N. Korkishko, Vyacheslav A. Fedorov, and Oksana Y. Feoktistova. Linbo3 optical waveguide fabrication by high-temperature proton exchange. *J. Lightwave Technol.*, 18(4):562, Apr 2000.

[36] Feng Chen, Xue-Lin Wang, and Ke-Ming Wang. Development of ion-implanted optical waveguides in optical materials: A review. *Optical materials*, 29(11):1523–1542, 2007.

[37] Ovidio Peña-Rodríguez, José Olivares, Mercedes Carrascosa, Ángel García-Cabañes, Antonio Rivera, and Fernando Agulló-López. Optical waveguides fabricated by ion implantation/irradiation: A review. *Ion Implantation, Prof. Mark Goorsky (Ed.), ISBN*, pages 978–953, 2012.

[38] GG Bentini, M Bianconi, L Correra, M Chiarini, P Mazzoldi, C Sada, N Argiolas, M Bazzan, and R Guzzi. Damage effects produced in the near-surface region of x-cut linbo3 by low dose, high energy implantation of nitrogen, oxygen, and fluorine ions. *Journal of applied physics*, 96(1):242–247, 2004.

[39] Jiao-Jian Yin, Fei Lu, Xian-Bing Ming, Yu-Jie Ma, and Meng-bing Huang. Theoretical modeling of refractive index in ion implanted linbo3 waveguides. *Journal of Applied Physics*, 108(3):033105, 2010.

[40] Kazuyoshi Itoh, Osamu Matoba, and Yoshiki Ichioka. Fabrication experiment of photorefractive three-dimensional waveguides in lithium niobate. *Optics letters*, 19(9):652–654, 1994.

[41] Jonas Burghoff, Christian Grebing, Stefan Nolte, and Andreas Tünnermann. Waveguides in lithium niobate fabricated by focused ultrashort laser pulses. *Applied surface science*, 253(19):7899–7902, 2007.

[42] W Horn, S Kroesen, J Herrmann, J Imbrock, and C Denz. Electro-optical tunable waveguide bragg gratings in lithium niobate induced by femtosecond laser writing. *Optics express*, 20(24):26922–26928, 2012.

[43] Nadège Courjal, Blandine Guichardaz, Gwenn Ulliac, Jean-Yves Rauch, Benattou Sadani, Hui-Hui Lu, and Maria-Pilar Bernal. High aspect ratio lithium niobate ridge waveguides fabricated by optical grade dicing. *Journal of Physics D: Applied Physics*, 44(30):305101, 2011.

[44] H. Hu, R. Ricken, W. Sohler, and R.B. Wehrspohn. Lithium niobate ridge waveguides fabricated by wet etching. *Photonics Technology Letters, IEEE*, 19(6):417–419, March 2007.

[45] Rei-Shin Cheng, Wei-Lin Chen, and Way-Seen Wang. Mach-zehnder modulators with lithium niobate ridge waveguides fabricated by proton-exchange wet etch and nickel indiffusion. *Photonics Technology Letters, IEEE*, 7(11):1282–1284, 1995.

[46] HJ Lee and S-Y Shin. Lithium niobate ridge waveguides fabricated by wet etching. *Electronics Letters*, 31(4):268–269, 1995.

[47] Payam Rabiei and William H Steier. Lithium niobate ridge waveguides and modulators fabricated using smart guide. *Applied Physics Letters*, 86(16):161115, 2005.

[48] Raghuram Narayan. Electrooptic coefficient variation in proton exchanged and annealed lithium niobate samples. *Selected Topics in Quantum Electronics, IEEE Journal of*, 3(3):796–807, 1997.

[49] Toshinori Nozawa, Hiroshi Miyazawa, and Shintaro Miyazawa. Water vapor effects on titanium diffusion into linbo3 substrates. *Japanese journal of applied physics*, 29(10R):2180, 1990.

[50] R. V. Schmidt. Metal-diffused optical waveguides in $LiNbO_3$. *Applied Physics Letters*, 25(8):458, 1974.

[51] F. Caccavale, C. Sada, F. Segato, and F. Cavuoti. Secondary ion mass spectrometry and optical characterization of Ti:$LiNbO_3$ optical waveguides. *Applied surface science*, 150(1):195–201, 1999.

[52] M. De Sario, M. N. Armenise, C. Canali, A. Carnera, P. Mazzoldi, and G. Celotti. TiO_2, $LiNb_3O_8$, and ($Ti_xNb_{1-x}O_2$) compound kinetics during Ti:$LiNbO_3$ waveguide fabrication in the presence of water vapors. *Journal of Applied Physics*, 57(5):1482, 1985.

[53] Y. Avrahami and E. Zolotoyabko. Diffusion and structural modification of Ti:LiNbO[sub 3], studied by high-resolution x-ray diffraction. *Journal of Applied Physics*, 85(9):6447, 1999. bibtex: avrahami_diffusion_1999.

[54] Makoto Minakata, Shoichi Saito, Masashi Shibata, and Shintaro Miyazawa. Precise determination of refractive-index changes in ti-diffused linbo3 optical waveguides. *Journal of Applied Physics*, 49(9):4677–4682, 1978.

[55] F Caccavale, P Chakraborty, A Quaranta, I Mansour, G Gianello, S Bosso, R Corsini, and G Mussi. Secondary-ion-mass spectrometry and near-field studies of ti: Linbo3 optical waveguides. *Journal of applied physics*, 78(9):5345–5350, 1995.

[56] Uma B. Ramabadran, Howard E. Jackson, and Joseph T. Boyd. Raman investigation of the nonlinear optical phenomenon of polarization rotation in Ti:LiNbO3 channel waveguides. *Journal of Applied Physics*, 74(3):1492–1500, 1993.

[57] Fernanda Irrera and Marco Valli. Characterization of planar Ti:LiNbO3 optical waveguides in the visible and near-infrared spectral range. *Journal of Applied Physics*, 64(4):1704–1708, 1988.

[58] Elmqvist Rune. Measuring instrument of the recording type, September 4 1951. US Patent 2,566,443.

[59] S. C. Terry, J. H. Jerman, and J. B. Angell. A gas chromatographic air analyzer fabricated on a silicon wafer. *IEEE Transactions on Electron Devices*, 26(12):1880–1886, 1979.

[60] Shuichi Shoji, Masayoshi Esashi, and Tadayuki Matsuo. Prototype miniature blood gas analyser fabricated on a silicon wafer. *Sensors and Actuators*, 14(2):101 – 107, 1988.

[61] H.T.G. van Lintel, F.C.M. van De Pol, and S. Bouwstra. A piezoelectric micropump based on micromachining of silicon. *Sensors and Actuators*, 15(2):153 – 167, 1988.

[62] G Whitesides and A Stroock. Flexible Methods for Microfluidics, 2001.

[63] A.D. Stroock and G.M. Whitesides. Components for integrated poly (dimethylsiloxane) microfluidic systems. *Electrophoresis*, 23(20):3461–3473, 2002.

[64] Paul J. A. Kenis, Rustem F. Ismagilove, and George M. Whitesides. Microfabrication Inside Capillaries Using Multiphase Laminar Flow Patterning. *Science*, 285(5424):83–85, 1999.

[65] H.A. Stone, A.D. Stroock, and A. Ajdari. Engineering Flows in Small Devices. *Annual Review of Fluid Mechanics*, 36(1):381–411, 2004.

[66] Todd M Squires and Stephen R Quake. Microfluidics: Fluid physics at the nanoliter scale. *Reviews of modern physics*, 77(3):977, 2005.

[67] Ángel Ríos, Mohammed Zougagh, and Mónica Avila. Miniaturization through lab-on-a-chip: Utopia or reality for routine laboratories? A review. *Analytica Chimica Acta*, 740:1–11, 2012.

[68] Michelle L. Kovarik, Douglas M. Ornoff, Adam T. Melvin, Nicholas C. Dobes, Yuli Wang, Alexandra J. Dickinson, Philip C. Gach, Pavak K. Shah, and Nancy L. Allbritton. Micro total analysis systems: Fundamental advances and applications in the laboratory, clinic, and field. *Analytical Chemistry*, 85(2):451–472, 2013.

[69] N. Craig Carville, Liam Collins, Michele Manzo, Katia Gallo, Bart I. Lukasz, Katey K. McKayed, Jeremy C. Simpson, and Brian J. Rodriguez. Biocompatibility of ferroelectric lithium niobate and the influence of polarization charge on osteoblast proliferation and function. *Journal of Biomedical Materials Research Part A*, 00000:n/a–n/a, 2014.

[70] P. Brunet, M. Baudoin, O. Bou Matar, and F. Zoueshtiagh. Droplet displacements and oscillations induced by ultrasonic surface acoustic waves: A quantitative study. *Physical Review E*, 81(3):036315, 2010.

[71] Wei-Kuo Tseng, Jr-Lung Lin, Wang-Chou Sung, Shu-Hui Chen, and Gwo-Bin Lee. Active micro-mixers using surface acoustic waves on Y-cut 128° LiNbO 3. *Journal of Micromechanics and Microengineering*, 16(3):539, 2006.

[72] Michael Esseling, Annamaria Zaltron, Wolfgang Horn, and Cornelia Denz. Optofluidic droplet router. *Laser & Photonics Reviews*, 9(1):98–104, 2015.

[73] Wolfgang Sohler, Hui Hu, Raimund Ricken, Viktor Quiring, Christoph Vannahme, Harald Herrmann, Daniel Büchter, Selim Reza, Werner Grundkötter, Sergey Orlov, et al. Integrated optical devices in lithium niobate. *Optics and Photonics News*, 19(1):24–31, 2008.

[74] a. Zaltron, G. Bettella, G. Pozza, R. Zamboni, M. Ciampolillo, N. Argiolas, C. Sada, S. Kroesen, M. Esseling, and C. Denz. Integrated optics on Lithium Niobate for sensing applications. 9506:950608, 2015.

[75] Linas Mazutis, John Gilbert, W Lloyd Ung, David A Weitz, Andrew D Griffiths, and John A Heyman. Single-cell analysis and sorting using droplet-based microfluidics. *Nature protocols*, 8(5):870–891, 2013.

[76] Eujin Um and Je-Kyun Park. A microfluidic abacus channel for controlling the addition of droplets. *Lab Chip*, 9(2):207–212, 2009.

[77] J.M Köhler, Th Henkel, A Grodrian, Th Kirner, M Roth, K Martin, and J Metze. Digital reaction technology by micro segmented flow—components, concepts and applications. *Chemical Engineering Journal*, 101(1-3):201–216, 2004.

[78] G F Christopher, J Bergstein, N B End, M Poon, C Nguyen, and S L Anna. Coalescence and splitting of confined droplets at microfluidic junctions. *Lab Chip*, 9(8):1102–1109, 2009.

[79] Shufang Zhao, Antoine Riaud, Guangsheng Luo, Yong Jin, and Yi Cheng. Simulation of liquid mixing inside micro-droplets by a lattice Boltzmann method. *Chemical Engineering Science*, 131:118–128, 2015.

[80] Yung-Chieh Tan and Abraham Phillip Lee. Microfluidic separation of satellite droplets as the basis of a monodispersed micron and submicron emulsification system. *Lab Chip*, 5(10):1178–1183, 2005.

[81] Yung-Chieh Tan, Yao Li Ho, and Abraham Phillip Lee. Microfluidic sorting of droplets by size. *Microfluidics and Nanofluidics*, 4(4):343–348, 2008.

[82] Adam R. Abate, Jeremy J. Agresti, and David A. Weitz. Microfluidic sorting with high-speed single-layer membrane valves. *Applied Physics Letters*, 96(20):203509, 2010.

[83] Keunho Ahn, Charles Kerbage, Tom P. Hunt, R. M. Westervelt, Darren R. Link, and D. A. Weitz. Dielectrophoretic manipulation of drops for high-speed microfluidic sorting devices. *Applied Physics Letters*, 88(2):024104, 2006.

[84] Jean-Christophe Baret, Oliver J Miller, Valerie Taly, Michael Ryckelynck, Abdeslam El-Harrak, Lucas Frenz, Christian Rick, Michael L Samuels, J Brian Hutchison, Jeremy J Agresti, Darren R Link, David A Weitz, and Andrew D Griffiths. Fluorescence-activated droplet sorting (FADS): efficient microfluidic cell sorting based on enzymatic activity. *Lab Chip*, 9(13):1850–1858, 2009.

[85] Feng Guo, Xing-Hu Ji, Kan Liu, Rong-Xiang He, Li-Bo Zhao, Zhi-Xiao Guo, Wei Liu, Shi-Shang Guo, and Xing-Zhong Zhao. Droplet electric separator microfluidic device for cell sorting. *Applied Physics Letters*, 96(19):193701, 2010.

[86] Alexandr Jonáš and Pavel Zemánek. Light at work: The use of optical forces for particle manipulation, sorting, and analysis. *Electrophoresis*, 29(24):4813–4851, 2008.

[87] Georgiy Tkachenko and Etienne Brasselet. Optofluidic sorting of material chirality by chiral light. *Nature Communications*, 5:1–7, 2014.

[88] Katherine S Elvira, Xavier Casadevall i Solvas, Robert C R Wootton, and Andrew J de Mello. The past, present and potential for microfluidic reactor technology in chemical synthesis. *Nature chemistry*, 5(11):905–15, 2013.

[89] Todd P Lagus and Jon F Edd. A review of the theory, methods and recent applications of high-throughput single-cell droplet microfluidics. *Journal of Physics D: Applied Physics*, 46(11):114005, 2013.

[90] Chun-Xia Zhao. Multiphase flow microfluidics for the production of single or multiple emulsions for drug delivery. *Advanced Drug Delivery Reviews*, 65(11-12):1420–1446, 2013.

[91] Jonathan H. Tsui, Woohyuk Lee, Suzie H. Pun, Jungkyu Kim, and Deok Ho Kim. Microfluidics-assisted in vitro drug screening and carrier production. *Advanced Drug Delivery Reviews*, 65(11-12):1575–1588, 2013.

[92] Jae-Hoon Choi, Seung-Kon Lee, Jong-Min Lim, Seung-Man Yang, and Gi-Ra Yi. Designed pneumatic valve actuators for controlled droplet breakup and generation. *Lab Chip*, 10(4):456–461, 2010.

[93] Jin Seok Hong, Beom Seok Lee, Dustin Moon, Jeong Gun Lee, and In Seok Kang. Pumpless dispensing of a droplet by breaking up a liquid bridge formed by electric induction. *ELECTROPHORESIS*, 31(8):1357–1365, 2010.

[94] Kazimierz Adamiak and Jerzy M. Floryan. Dynamics of water droplet distortion and breakup in a uniform electric field. *IEEE Transactions on Industry Applications*, 47(6):2374–2383, 2011.

[95] Matthieu Robert de Saint Vincent, Hamza Chraïbi, and Jean-Pierre Delville. Optical Flow Focusing: Light-Induced Destabilization of Stable Liquid Threads. *Physical Review Applied*, 4(4):044005, 2015.

[96] Winston Duo Wu, Sean Xuqi Lin, and Xiao Dong Chen. Monodisperse droplet formation through a continuous jet break-up using glass nozzles operated with piezoelectric pulsation. *AIChE Journal*, 57(6):1386–1392, 2011.

[97] Ferraro P., Coppola S., Grilli S., Paturzo M., and Vespini V. Dispensing nano-pico droplets and liquid patterning by pyroelectrodynamic shooting. *Nat Nano*, 5(6):429–435, jun 2010.

[98] Krzysztof Churski, Jacek Michalski, and Piotr Garstecki. Droplet on demand system utilizing a computer controlled microvalve integrated into a stiff polymeric microfluidic device. *Lab Chip*, 10(4):512–518, 2010.

[99] Sung-Yong Park, Ting-Hsiang Wu, Yue Chen, Michael A Teitell, and Pei-Yu Chiou. High-speed droplet generation on demand driven by pulse laser-induced cavitation. *Lab Chip*, 11(6):1010–1012, 2011.

[100] P. B. Umbanhowar, V. Prasad, and D. a. Weitz. Monodisperse emulsion generation via drop break off in a coflowing stream. *Langmuir*, 16(2):347–351, 2000.

[101] Todd Thorsen, Richard W. Roberts, Frances H. Arnold, and Stephen R. Quake. Dynamic pattern formation in a vesicle-generating microfluidic device. *Physical Review Letters*, 86(18):4163–4166, 2001.

[102] Piotr Garstecki, Michael J Fuerstman, Howard A Stone, and George M Whitesides. Formation of droplets and bubbles in a microfluidic T-junction-scaling and mechanism of break-up. *Lab Chip*, 6(3):437–446, 2006.

[103] Maartje L. J. Steegmans, Jolet De Ruiter, Karin G. P. H. Schroën, and Remko M. Boom. A descriptive force-balance model for droplet formation at microfluidic y-junctions. *AIChE Journal*, 56(10):2641–2649, 2010.

[104] Volkert van Steijn, Chris R Kleijn, and Michiel T Kreutzer. Predictive model for the size of bubbles and droplets created in microfluidic T-junctions. *Lab on a chip*, 10(19):2513–2518, 2010.

[105] Dieter A Wolf-Gladrow. *Lattice-gas cellular automata and lattice Boltzmann models: An Introduction*. Number 1725. Springer Science & Business Media, 2000.

[106] Sauro Succi. *The lattice Boltzmann equation: for fluid dynamics and beyond*. Oxford university press, 2001.

[107] Xiao Bin Li, Feng Chen Li, Juan Cheng Yang, Haruyuki Kinoshita, Masamichi Oishi, and Marie Oshima. Study on the mechanism of droplet formation in T-junction microchannel. *Chemical Engineering Science*, 69(1):340–351, 2012.

[108] Dongying Qian and Adeniyi Lawal. Numerical study on gas and liquid slugs for Taylor flow in a T-junction microchannel. *Chemical Engineering Science*, 61(23):7609–7625, 2006.

[109] M. DE MENECH, P. GARSTECKI, F. JOUSSE, and H. A. STONE. Transition from squeezing to dripping in a microfluidic t-shaped junction. *Journal of Fluid Mechanics*, 595:141–161, 1 2008.

[110] Gordon F. Christopher, N. Nadia Noharuddin, Joshua a. Taylor, and Shelley L. Anna. Experimental observations of the squeezing-to-dripping transition in T-shaped microfluidic junctions. *Physical Review E - Statistical, Nonlinear, and Soft Matter Physics*, 78(3):1–12, 2008.

[111] H.A. Stone. On lubrication flows in geometries with zero local curvature. *Chemical Engineering Science*, 60(17):4838–4845, 2005.

[112] Volkert van Steijn, Chris R. Kleijn, and Michiel T. Kreutzer. Flows around Confined Bubbles and Their Importance in Triggering Pinch-Off. *Physical Review Letters*, 103(21):214501, 2009.

[113] Mary E. Wilson, Nithyanand Kota, YongTae Kim, Yadong Wang, Donna B. Stolz, Philip R. LeDuc, and O. Burak Ozdoganlar. Fabrication of circular microfluidic channels by combining mechanical micromilling and soft lithography. *Lab Chip*, 11:1550–1555, 2011.

[114] Ciprian Iliescu, Hayden Taylor, Marioara Avram, Jianmin Miao, and Sami Franssila. A practical guide for the fabrication of microfluidic devices using glass and silicon. *Biomicrofluidics*, 6(1), 2012.

[115] Roberto Osellame, Giulio Cerullo, and Roberta Ramponi. *Femtosecond Laser Micromachining: Photonic and Microfluidic Devices in Transparent Materials*, volume 123. Springer Science & Business Media, 2012.

[116] Mathieu Chauvet, Luai Al Fares, and Fabrice Devaux. Self-trapped beams for fabrication of optofluidic chips. *Proc. SPIE*, 8434:84340Q–84340Q–7, 2012.

[117] M. Chauvet, L. Al Fares, B. Guichardaz, F. Devaux, and S. Ballandras. Integrated optofluidic index sensor based on self-trapped beams in linbo3. *Applied Physics Letters*, 101(18), 2012.

[118] Masashi Tamura and Shinzo Yoshikado. Etching characteristics of linbo3 crystal by fluorine gas plasma reactive ion etching. *Science and Technology of Advanced Materials*, 2(3–4):563 – 569, 2001.

[119] Z. Ren, P. J. Heard, J. M. Marshall, P. A. Thomas, and S. Yu. Etching characteristics of linbo3 in reactive ion etching and inductively coupled plasma. *Journal of Applied Physics*, 103(3), 2008.

[120] Manoj Sridhar, Devendra K Maurya, James R Friend, and Leslie Y Yeo. Focused ion beam milling of microchannels in lithium niobate. *Biomicrofluidics*, 6(1):012819, 2012.

[121] G Della Valle, R Osellame, and P Laporta. Micromachining of photonic devices by femtosecond laser pulses. *Journal of Optics A: Pure and Applied Optics*, 11(1):013001, 2009.

[122] Rafael R Gattass and Eric Mazur. Femtosecond laser micromachining in transparent materials. *Nature photonics*, 2(4):219–225, 2008.

[123] Zeyad Yousif Abdoon Al-Shibaany, John Hedley, Dehong Huo, and Zhongxu Hu. Micromachining lithium niobate for rapid prototyping of resonant biosensors. *IOP Conference Series: Materials Science and Engineering*, 65(1):012030, 2014.

[124] Shantanu Bhattacharya, Arindom Datta, Jordan M Berg, and Shubhra Gangopadhyay. Studies on surface wettability of poly (dimethyl) siloxane (pdms) and glass under oxygen-plasma treatment and correlation with bond strength. *Microelectromechanical Systems, Journal of*, 14(3):590–597, 2005.

[125] Thomas Young. An essay on the cohesion of fluids. *Philosophical Transactions of the Royal Society of London*, pages 65–87, 1805.

[126] John Shipley Rowlinson and Benjamin Widom. *Molecular theory of capillarity*. Courier Corporation, 2013.

[127] Alexander Y Fadeev and Yuri V Kazakevich. Covalently attached monolayers of oligo (dimethylsiloxane) s on silica: a siloxane chemistry approach for surface modification. *Langmuir*, 18(7):2665–2672, 2002.

[128] Noémi Rozlosnik, Michael C. Gerstenberg, and Niels B. Larsen. Effect of solvents and concentration on the formation of a self-assembled monolayer of octadecylsiloxane on silicon (001). *Langmuir*, 19(4):1182–1188, 2003.

[129] Harish Palani Naga Surya, Sajeesh Parayil, Utsab Banerjee, Subhash Chander, and Ashis Kumar Sen. Alternating and merged droplets in a double T-junction microchannel. *Biochip Journal*, 9(1):16–26, 2015.

[130] Chan Yuan Tan and Yao Xiong Huang. Dependence of Refractive Index on Concentration and Temperature in Electrolyte Solution, Polar Solution, Nonpolar Solution, and Protein Solution. *Journal of Chemical and Engineering Data*, 60(10):2827–2833, 2015.

[131] M Grad, CC Tsai, M Yu, DL Kwong, CW Wong, and D Attinger. Transient sensing of liquid films in microfluidic channels with optofluidic microresonators. *Measurement Science and Technology*, 21(7):075204, 2010.

[132] Lih Feng Cheow, Levent Yobas, and Dim Lee Kwong. Digital microfluidics: Droplet based logic gates. *Applied Physics Letters*, 90(5):1–4, 2007.

[133] Michael W. Toepke, Vinay V. Abhyankar, and David J. Beebe. Microfluidic logic gates and timers. *Lab Chip*, 7:1449–1453, 2007.